11-11-2016

Ferroelectric Switching and d33 Mapping of Micro-Patterned Piezoelectrics by Piezo Force Microscopy

Linghan Ye
University of Connecticut - Storrs, linghan.ye@uconn.edu

Ferroelectric Switching and d_{33} Mapping of Micro-Patterned Piezoelectrics by Piezo Force Microscopy

Linghan Ye, PhD

University of Connecticut, 2016

Abstract

The domain configurations and piezoelectric coefficient of ferroelectric materials such as PZT and PMN-PT thin films can have a significant effect on the optimization of future electronic devices. Piezo Force Microscopy (PFM) is an ideal tool based on Atomic Force Microscopy that allows unique investigations of such nanoscale effects, and can further be implemented to monitor domain switching dynamics.

Utilizing PFM, the domain orientations as well as switching dynamics can be tracked in-situ. As the lateral dimension plays an important role in ferroelectric properties since it influences in-plane strain, both normal and lateral domain orientations are uniquely mapped simultaneously. Leveraging a new method for fabricating ferroelectric mesas down to the nanoscale, coercive fields and switching kinetics have thereby been investigated for continuous strained films as well as geometrically strain-relieved samples. A piezoelectric enhancement at edges of engineered nano islands is directly observed, while switching activation energies have been calculated and related to the strain-relief behavior.

Piezoelectric coefficients in the surface normal direction were precisely measured on 2 μm, 1 μm and 0.75 μm wide PMN-PT microfabricated structures. These revealed piezoelectric enhancements up to 500 nm from feature edges for 2 μm or wider structures, and an increasing overall enhancement throughout smaller 1 μm and 0.75 μm structures as the strain relief

becomes more complete. These results are corroborated by X-RAY diffraction and dielectric measurements from collaborators.

The enhancement of dielectric and piezoelectric properties for geometrically strain relieved structures should furthermore be applicable to in-plane piezoactuation. Accordingly, lateral piezoactuation for PMN-PT microstructures is recorded for 4 µm and 2 µm features revealing direction-dependent edge enhancement as hypothesized. Such insights are crucial for ferroelectric strain engineering efforts, the development of new device mechanisms, and their ultimate performance.

Ferroelectric Switching and d_{33} Mapping of Micro-Patterned Piezoelectrics by Piezo Force Microscopy

Linghan Ye

B.S., Beijing University of Technology, 2010

M.S., University of Connecticut, 2013

A Dissertation

Submitted in Partial Fulfillment of the

Requirements for the Degree of

Doctor of Philosophy

At the

University of Connecticut

2016

APPROVAL PAGE

Doctor of Philosophy Dissertation

Ferroelectric Switching and d_{33} Mapping of Micro-Patterned Piezoelectrics by Piezo Force Microscopy

Presented by

Linghan Ye, B.S., M.S.

Major Advisor_____
Dr. Bryan D. Huey

Associate Advisor_____
Dr. Pamir Alpay

Associate Advisor_____
Dr. Serge Nakhmanson

University of Connecticut

2016

Acknowledgements

First, I would like to thank my advisor Dr. Bryan D. Huey for his great encouragement and guidance throughout the whole work and also for his understanding and support through hard times.

I would like to thank my advisory committee, Dr. Pamir Alpay, Dr. Serge Nakhmanson, Dr. Seok-woo Lee and Dr. Puxian Gao, for their critical reviews and important suggestions on this work.

I would also like to thank Huey NanoMeasurement Lab members: Dr. James Louis Bosse, Dr. Yasemin Kutes, Manuel Rivas, Dr. Justin Luria, James Steffes and Ryan Cordier for their help and support and creating a friendly work environment.

I would like to thank our collaborators, Dr. Ramesh's group in UC Berkeley and Dr. Trolier-McKinstry group in Penn State University for providing samples and other measurements.

I would also like to thank the staff at Asylum Research for providing readily available technical support for the AFM.

And I would like to thank those professors and students in IMS that provide samples to us and collaborations.

Finally, I would like to thank my family in China for the love and support they send from thousands of miles away.

Table of Contents

List of Figures

Chapter 1 Background

1.1 Ferroelectricity

Ferroelectrics are essential materials in a wide range of applications, including nonvolatile memories, various sensors and actuators [1-4]. Ferroelectricity is a property of certain materials possessing a spontaneous polarization that can be reversed by the application of an external electric field[5]. The study of ferroelectric thin films started when non-volatile RAM raised interest in late 1960s. The ferroelectric hysteresis loop of polarization versus electric field can be leveraged for data storage in Figure 1.1. Hence FeRAM is a promising device in the future because of power-efficiency and high writing speed compared to flash memories[6-8].

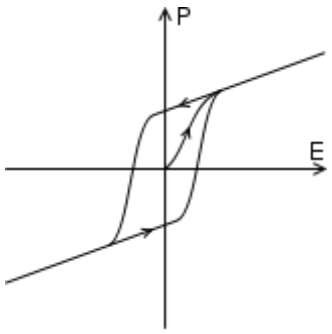

Figure 1.1 Typical ferroelctric polarization hysteresis loop[9].

The crystal system can be divided into 32 crystal classes as 20 of them are asymmetric and exhibit piezoelectricity with center ion slightly displaced upon forces. At room temperature, Ferroeletric materials have multiple polarized orientations at zero electric field; Above the Curie temperature Tc, they switch to a phase with the highest symmetries and no spontaneous polarization[10]. For example, a lot of materials such as Lead Zirconate Titanate (PZT) exhibit

ferroelectric property in z axis; and Barium Titanate can be ferroelectric in two or more directions[11].

Here we focus on perovskites structure ABO_3, where A and B are usually metals with the oxygen in the face centers[12]. The center ion is slightly displaced from the center of the unit cell during the ferroelectric state. This further generates a dipole moment causing the lattice expanded or compressed by external electric field shown in Figure 1.2.

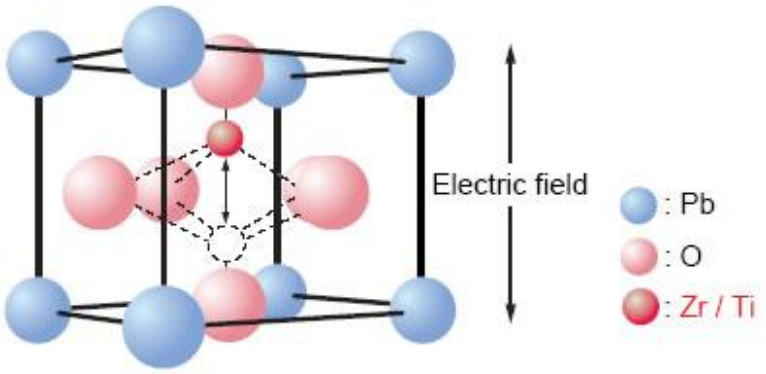

Figure 1.2. PZT crystal structure with ion displaced by electric field[13].

In response to a mechanical stress, piezoelectric materials can also accumulate charges during the electromechanical process. An applied DC field E causes an enhanced locally acting field E' by the polarization P it creates[14]:

$$\mathbf{E'=E+}\boldsymbol{\omega}\frac{\boldsymbol{P}}{\boldsymbol{\varepsilon_0}}\mathbf{;} \qquad (1)$$

where $\omega=\frac{1}{3}$, the Lorentz factor; ε is the permittivity and E is the electric field. The polarization P is measured by the electric susceptibility χ, which represents the ability of a material to polarize in response to the field. Microscopically this is caused by the polarizability α of N molecular entities per unit volume under the influence of E':

$$\mathbf{P=}\boldsymbol{\chi\varepsilon_0}\mathbf{E=N}\boldsymbol{\alpha E'}\mathbf{;} \qquad (2)$$

1.2 AFM

Atomic Force Microscopy (AFM) is a microscopy utilizing a probe to scan on the sample surface with spatial resolution at nanoscale[15-17]. When the tip is scanning the surface, deflection force can be generated which is measured using a laser spot reflected into segmented photodiodes. By recording these signals while scanning, images of the topography and other detected properties can be formed. The primary modes of operation for AFM are Contact mode and AC mode.

1.2.1 Contact Mode

In contact mode, AFM tip is in contact with the sample surface and maintains a constant deflection shown in Figure 1.3. This is achieved with a feedback loop by extending or contracting the Z piezo scanner to maintain the deflection set point. The height change in Z axis thus defines topography[18]. When the stiffness of the cantilever is smaller than the surface, essentially always the case for semiconducting materials as investigated in this work, the tip bends proportional to any changes in surface height. Contact mode operation enables high scanning speeds, especially useful for friction imaging and studying ferroelectric dynamics. A critical limit is that the lateral forces applied may distort soft samples such as polymers, leading to permanent surface damage and poor image resolution[19].

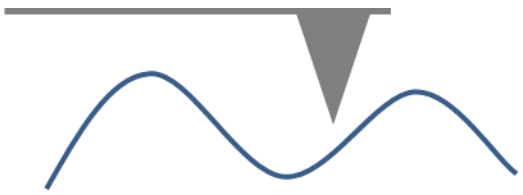

Figure 1.3 AFM tip and sample interaction in contact mode.

1.2.2 AC Mode (Tapping)

In this operation mode, the cantilever is vibrated at a resonant frequency with oscillation amplitude typically around 20-100nm[20, 21]. During scanning, the tip intermittently contacts the surface and a constant oscillation amplitude is maintained as in Figure 1.4 by again adjusting the extension of a z-actuator as necessary. A height image can thus be obtained as with contact AFM, by recording the z-actuation as a function of position. Phase image can also be recorded as the phase of oscillation is disturbed by touching the surface, inducing a phase difference between the tip and the drive oscillator. The contrast of a phase image is strongly related to the local elastic properties and relative surface energies of the sample[22].

Thus tapping mode can achieve higher imaging resolution of samples that can be easily deformed, due to less force applied and eliminated lateral force. However, disadvantages for AC modes are that they require a lower speed of scanning.

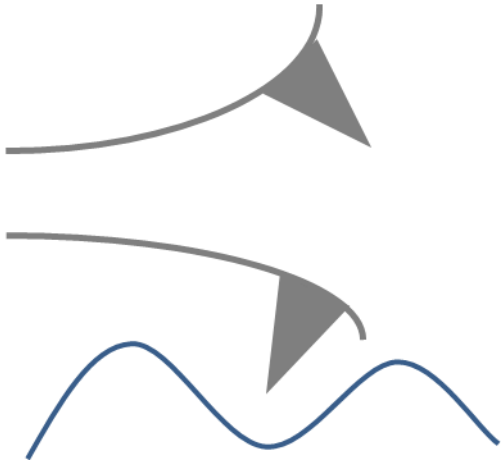

Figure 1.4. Tip and sample interaction in the tapping mode.

1.3 Piezo Force Microscopy (PFM)

Piezo Force Microscopy is a combination of Atomic Force Microscopy and other electronics to detect the mechanical response of ferroelectric materials upon electric field[23]. A conductive probe is in contact with the surface of a thin film which locally expands or contracts by the

converse piezoelectric effect. This gives rise to the cantilever deflection as demonstrated in Figure 1.5. By applying an AC bias, the periodic relative expansion and contraction of the surface, and hence a periodic signal for the AFM, is thus actuated and detected as a function of the tip position, biasing conditions, and specimen properties[24, 25]. This general concept has been widely used to study the ferroelectric polarization direction, domain configuration, and switching dynamics in ferroelectric specimens.

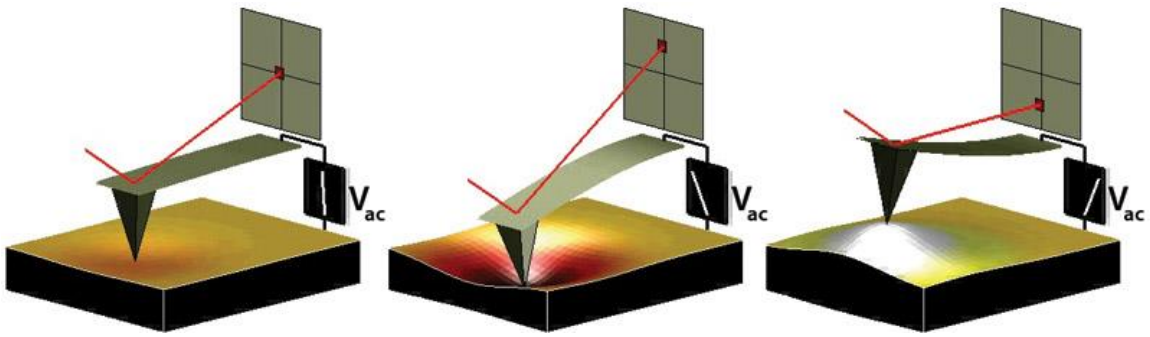

Figure 1.5. PFM cantilever deflection upon applied voltage[26].

There are three components in a typical PFM system: AFM, Lock-in Amplifier and Function Generator. A Function generator is electronic equipment generating various electrical waveforms such as sine waves with ranges of frequency from Hz to MHz. Thus, it enables frequency sweeps to maximize the piezo response and superimposes AC and DC bias directly applied to the tip during PFM measurements. A Lock-in amplifier is a highly sensitive external unit that extracts a signal at a certain frequency from a noisy environment and determines the amplitude and phase. It analyzes the input signal, eliminates signal other than the frequency of reference and amplifies the recovered signal from pm to nm[27].

Therefore, we can map out the surface microstructure and ferroelectric domain simultaneously. While the AFM topography is only a DC response of the tip height; the electromechanical

excitation is an AC measurement with high frequency (usually 500 kHz to 2 MHz). Oppositely polarized domains under AC field exhibit 180° phase shifts.

1.4 Piezo Response

PFM amplitude image indicates the magnitude of the piezoelectric signal, while the phase demonstrates the polarization orientation for individual domains, shown in Figure 1.6.

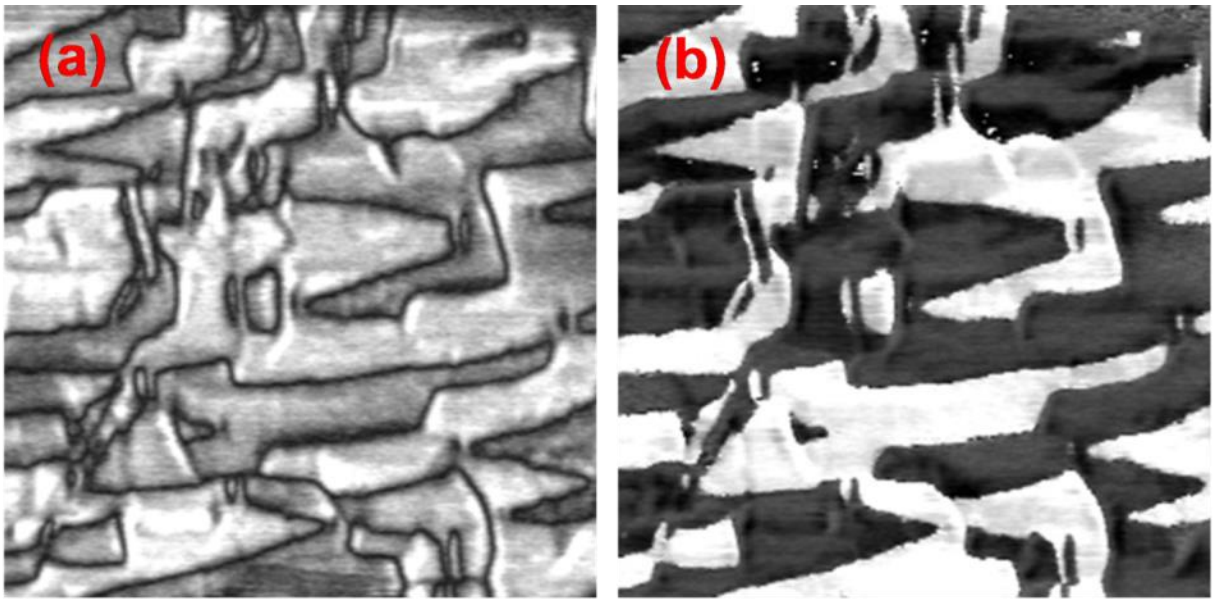

Figure 1.6. (a) Amplitude image and (b) Phase image acquired by PFM.

Amplitude signal is proportional to the bias induced piezo excitation [28]. The tip is applied with a periodic voltage,

$$V_{tip}=V_{dc}+V_{ac}\mathrm{Cos}\,(\omega t); \qquad (3)$$

The corresponding piezoactuation and electrostatic force in PFM thus can be calculated as follows:

$$\mathbf{Z} = (d_{eff} + (Lw\varepsilon_0\Delta V) / (48\mathrm{k}h_2))V_{AC}, \quad [29] \qquad (4)$$

where h is the height of the tip, ε_0 and ΔV are the dielectric constant of the air and voltage respectively; L and w are the length and width of AFM probe while d_{eff} is the effective piezoactuated displacement. The second term is taken from capacitive forces. Furthermore, a stiff cantilever can increase the PFM signal with the disadvantage of deforming samples. Conductive diamond coated probes are usually employed as a result.

Resonant frequency is crucial as the maximum piezoelectric oscillation occurs when applied AC is tuned to the optimized frequency with highest sensitivity in AFM. Moreover, by increasing the contact resonance, the cantilever gets stiff, reducing the electrostatic artifacts as described earlier before it reaches a limit as piezo amplitude decreases with frequency. By combining all these factors, AFM employs frequency from 500 kHz to 2 MHz in general. Thus we achieve frequency sweep to optimize the PFM performance with the function generator. As contact resonance can easily be affected by local surface, large contact area would cause a different contact resonance since stiffness changes. To reduce the topographic artifact, AC frequency should be selected around the resonant peak other than the peak itself[30].

1.5 Piezoelectric Coefficients

Piezoelectricity is the ability of piezoelectric materials with an electrical charge proportional to an applied mechanical force: this is a direct effect. Piezoelectric materials also exhibit a converse effect, where strain is produced via the application of electric field. Thus, the Piezoelectric d quantifies the volume change on application of stress[31, 32].

$$\boldsymbol{d_{ij} = \frac{P}{\sigma}} \qquad (5)$$

Since piezoelectric materials are anisotropic, the piezoelectric charge constants d can be related to the applied force and generated polarization which are two subscripts. The first subscript to d

represents the direction of induced polarization or strain; and the second subscript is the direction of applied field strength such as electric field E or applied mechanical stress, respectively. Therefore, d is a crucial factor of the performance of piezoelectric materials.

For ferroelectric applications upon applied voltage, the orientation of polarization is usually along x, y and z axis which is indicated by the subscript 1, 2 and 3 respectively. The shear force axes are 4, 5 and 6 shown in Figure 1.7[33].

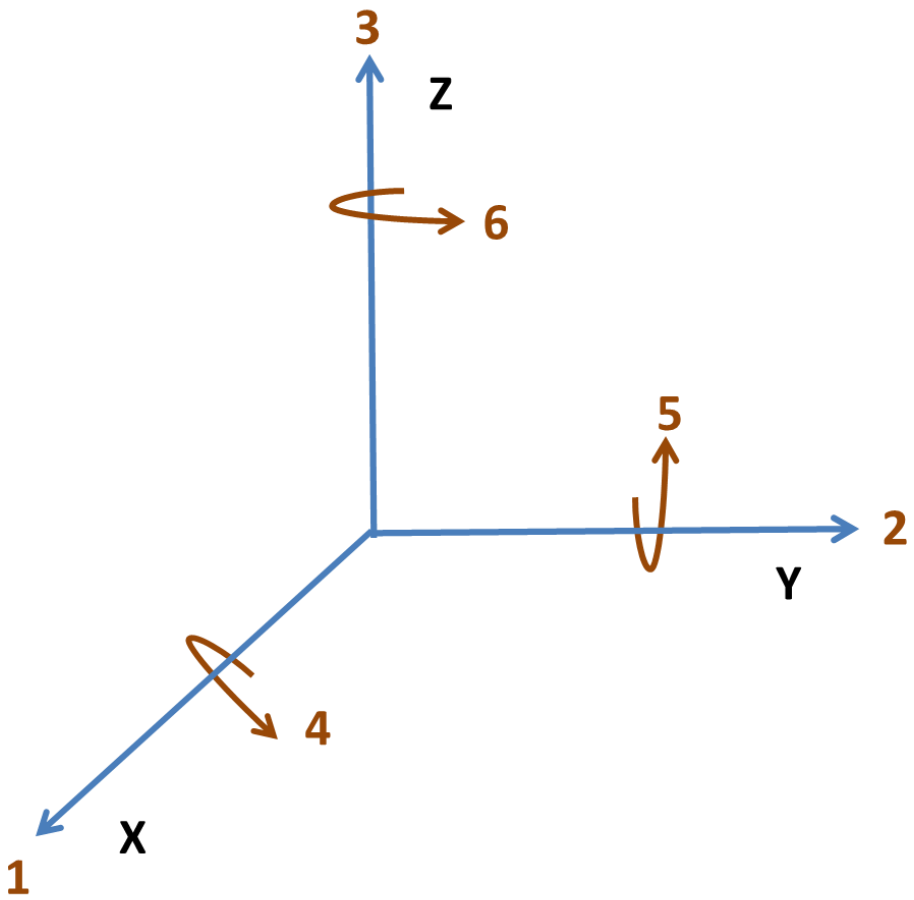

Figure 1.7. Directions of the subscripts affecting the piezoelectric coefficients.

For instance, d_{33} indicates the induced polarization in direction 3 which is parallel to the z axis with electrical field also applied in direction 3. d_{31} demonstrates the polarization in direction 3 while the force applied in direction 1 which is perpendicular to the z axis and polarization

orientation. Piezo Force Microscopy is widely used to detect piezoelectric response and polarization orientation in 3 dimensions[34]. Therefore, the induced strain or polarization can be mapped comprehensively in all directions in piezoelectric materials.

1.6 Domain Dynamics

Previous study has been reported about investigating the domain switching kinetics based on the duration of switching. Many factors would influence the results such as small dimensions of ferroelectric materials and switching voltage. At the initial state for ferroelectric materials, domains are assumed to be configured to minimize the overall free energy. Upon applying a potential sufficient to surpass the coercive field, the domains switch orientations according to the field direction and grow accordingly[35]. Domain switching involves the nucleation of new domains, growth of the nucleation sites, as well as normal and especially lateral domain wall movement. Several classic theories have been implemented to describe this switching mechanism, in particular based on growth limited switching, and nucleation limited switching. Either, or both, may dominate depending on temperature, specimen geometry, nucleation site density, etc. [36, 37].

1.6.1 Domain Growth Limited switching (KAI Model)

The traditional investigation of domain switching dynamics is based on Kolmogorov and Avrami's so called 'KAI model.' The fundamental assumption is that ferroelectric domains grow unrestrictedly and the domain wall velocity depends on the external field after nucleation. At the beginning stage, domains grow without overlapping. Once the domains overlap with each other, the volume of the reversed polarized area is not equal to the sum of each individual domain. Therefore, KAI model leads to the equation below to model ferroelectric switching [38, 39].

$$p(t) = 1 - e^{-(t/t_0)^n} \quad (6)$$

where p(t) is the fraction of the volume of the ferroelectric switched by time t, the parameters t_0 and n depend on the nucleation density for the reversed domains, mobility of the domain walls, the electric field acting on the moving domain walls E, and the dimension of the domain growth. This model provides a suitable explanation for short period of switching time in ferroelectric thin films. However, this theory cannot address the switching kinetics during a broad time interval[40].

1.6.2 Domain Nucleation Limited Switching (NSL Model)

On the other hand, the Nucleation Limited switching (NSL) model illustrates that switching depends on a distribution of time with independent domains nucleating. In this case, domain switching occurs region by region, with nucleation sites not influencing subsequent switching of neighboring regions, i.e. these domains do not participate in switching of the rest film. The switching rate is then [41]

$$p(t) = \int_{-\infty}^{In\, t} g(z)dz \quad (7)$$

where g(z) is the distribution function of the nucleation times. The differences for the two models are illustrated in Figure 1.8.

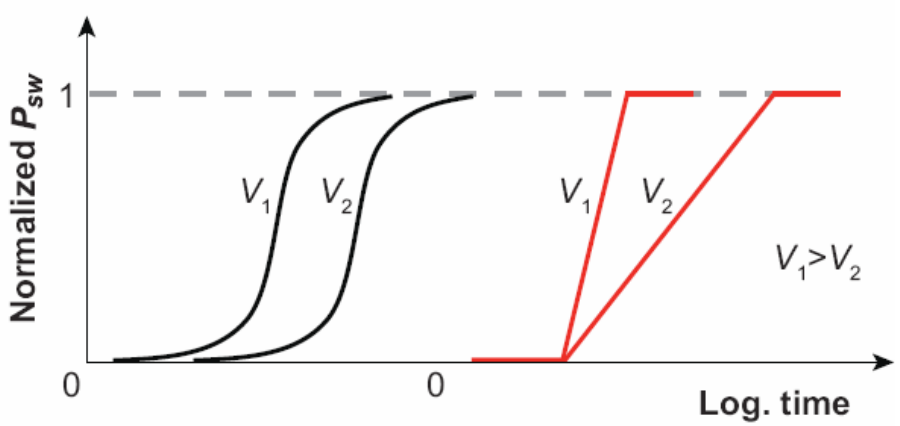

Figure 1.8. KAI model (left side) and NSL model (right side) describe the time dependence of polarization switching[42].

1.7 Piezoelectric Property of PZT

Lead Zirconate Titanate with the chemical formula $Pb[Zr_xTi_{1-x}]O_3$ employs the perovskite structure where Ti^{4+} and Zr^{4+} ions occupy B sites, Pb^{2+} occupy A site. At room temperature, remarkable piezoelectric effect of PZT has been widely considered for many devices such as MEMS, sensors and memory [43-45]. Thus many film deposition techniques have been applied to synthesize PZT thin films such as chemical vapor deposition (CVD)[46], sol-gel[47] and ion-beam sputtering[48].

A phase diagram has been shown in Figure 1.9 to indicate the influence of chemical compositions on piezoelectric properties. The Ti rich region of the phase diagram shows a tetragonal ferroelectric phase and Zr rich region shows rhombohedral. They have been divided by a morphotropic phase boundary (MPB) causing an abrupt change in lattice constants of PZT [49-51]. Therefore large piezoelectric effect and polarization can be observed at MPB as phase coexistence[52].

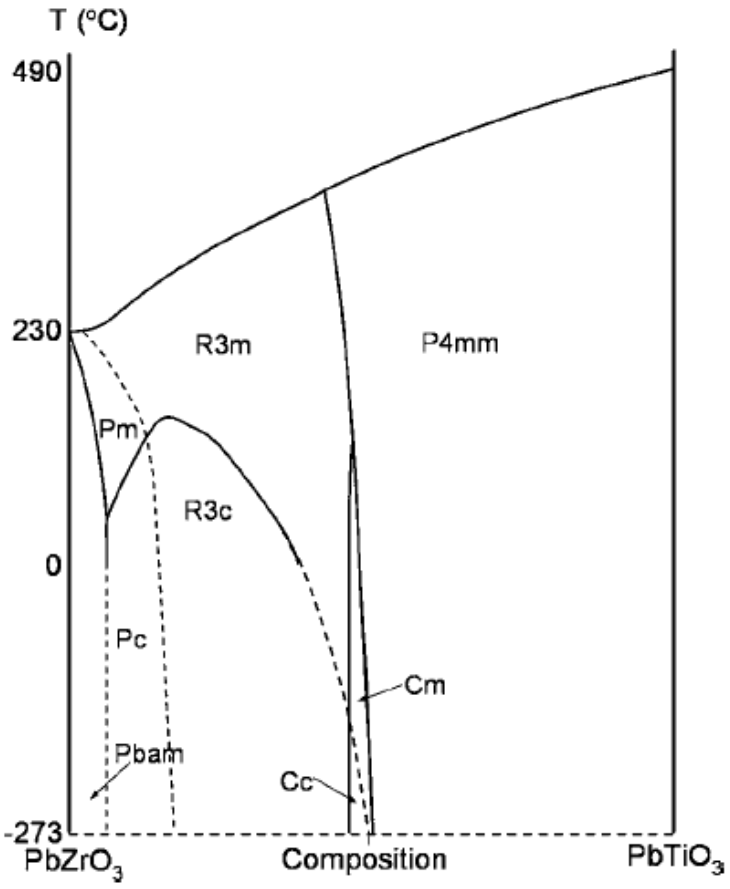

Figure 1.9. $PbrO_3$ and $PbTiO_3$ phase diagrams.

1.8 TEM Characterization

Another method for investigating domain switching in ferroelectrics and multiferroics is Transmission Electron Microscopy [53-55]. For example, TEM has been used to study the dynamics of ferroelectric switching in $BiFeO_3$ epitaxial thin films. It was able to resolve localized nucleation sites, the presence of domain walls, and also ferroelectric switching at interfaces [56]. In this case, an electric field is applied normally between a bottom electrode and a top electrode, even an in-situ SPM tip, to switch a BFO film locally. Unlike with PFM, however, the specimen is observed in cross section, i.e. perpendicular to the applied field.

For instance, Figure 1.10 shows ferroelectric switching starting with a single nucleation event occurring at the interface with the back contact (white arrow), and this domain grows laterally

and normally through the film with increasing applied voltage. Such results are very useful as they can correlate nucleation sites and domain growth with the local microstructure, chemical content, even up to atomic resolution with HRTEM. However, TEM cannot resolve any vectors of the polarized orientations normal to the field of view, a disadvantage of TEM compared to PFM where the 3-d polarization orientation can be deduced.

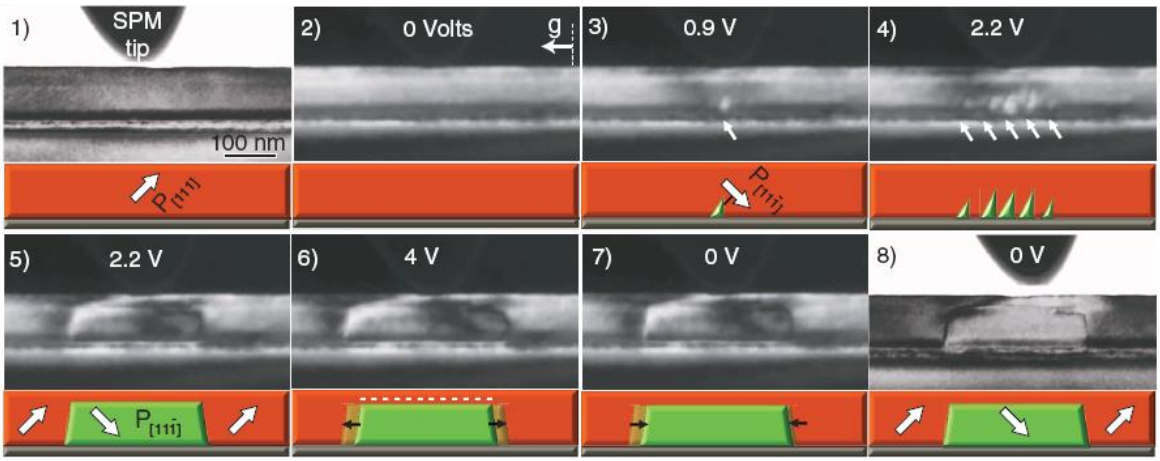

Figure 1.10. TEM dark field images show the domain nucleation and growth process with external voltage in cross-section view[56].

Cracks developing under electric fields in PZT polycrystalline ceramics can also been observed in situ TEM, Figure 1.11 [57]. The original pore was applied upon a cyclic electric field along the direction indicated by the arrow. This pore expanded into cracks under TEM has been revealed.

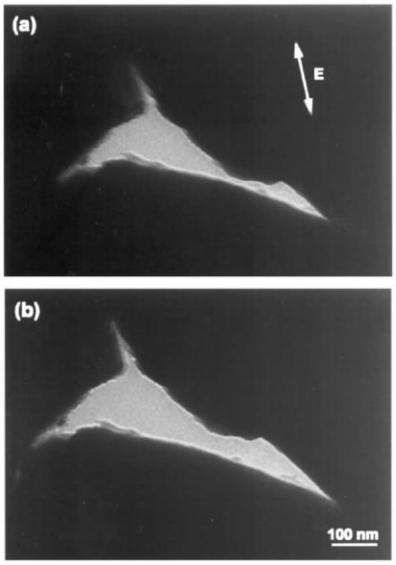

Figure 1.11. Initiation of microcrack from a pore at the triple junction of the grain boundaries of PZT thin film: (a) before application of electric field; (b) after cycles.

1.9 Declamping Effect

It has been reported that the internal stress due to lattice mismatch can affect the electrical and electromechanical property [58-61]. By adjusting the internal stress, ferroelectric polarization of thin films can be controlled as well. For instance, V. Nagarajan etc. report the effect of various substrates on piezoelectric behaviors of 100-nm-thick epitaxial 0.9PMN–0.1PT thin films[62]. As different substrates would induce compressive or tensile strain conditions, the electromechanical property strongly depends on the substrate-induced stress.

Moreover, A. L. Roytburd etc. reveal crucial recovery in the piezoelectric property of PZT by reducing the degree of internal stress based on distinct film-substrate design[63]. Figure 1.12 (a) shows the schematic model of internal stress filed distributed across the entire film for epitaxial film. Figure (b) demonstrates the internal stress and constraint for strip structures with lateral width D much smaller than thickness h decrease significantly. The reduction in constraint is caused by the declamping effect and the strain condition for the surface of the strip film is traction-free[64].

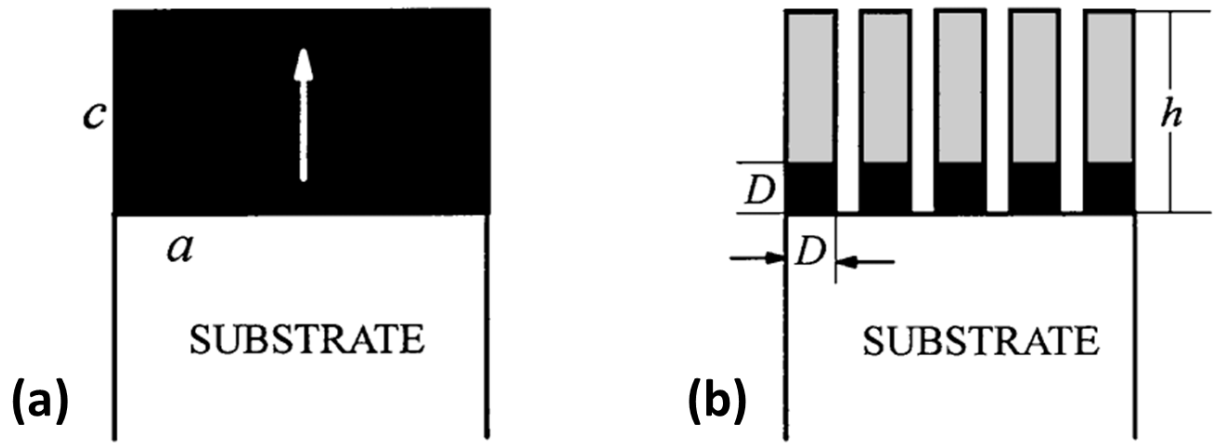

Figure 1.12. Uniform stress field in the epitaxial film (a); Cutting film into stripes along [100] with lateral D and thickness h[63].

In addition, the piezoelectric material nearest the sidewalls is more declamped than the feature centers. The theoretical results exhibit a considerable increase in the saturation polarization due to epitaxial stresses. Significant recovery in the piezoelectric constant has been verified for geometric configurations with reduced degree of constraint. For instance, piezoelectric coefficient for delineated island is significantly larger than the continuous film for 120 nm thick PNZT on Si substrate[63].

Therefore, declamping effect exhibited by patterning piezoelectric materials is related to the feature's width: thickness aspect ratio; smaller aspect ratio yields improved functional performance.

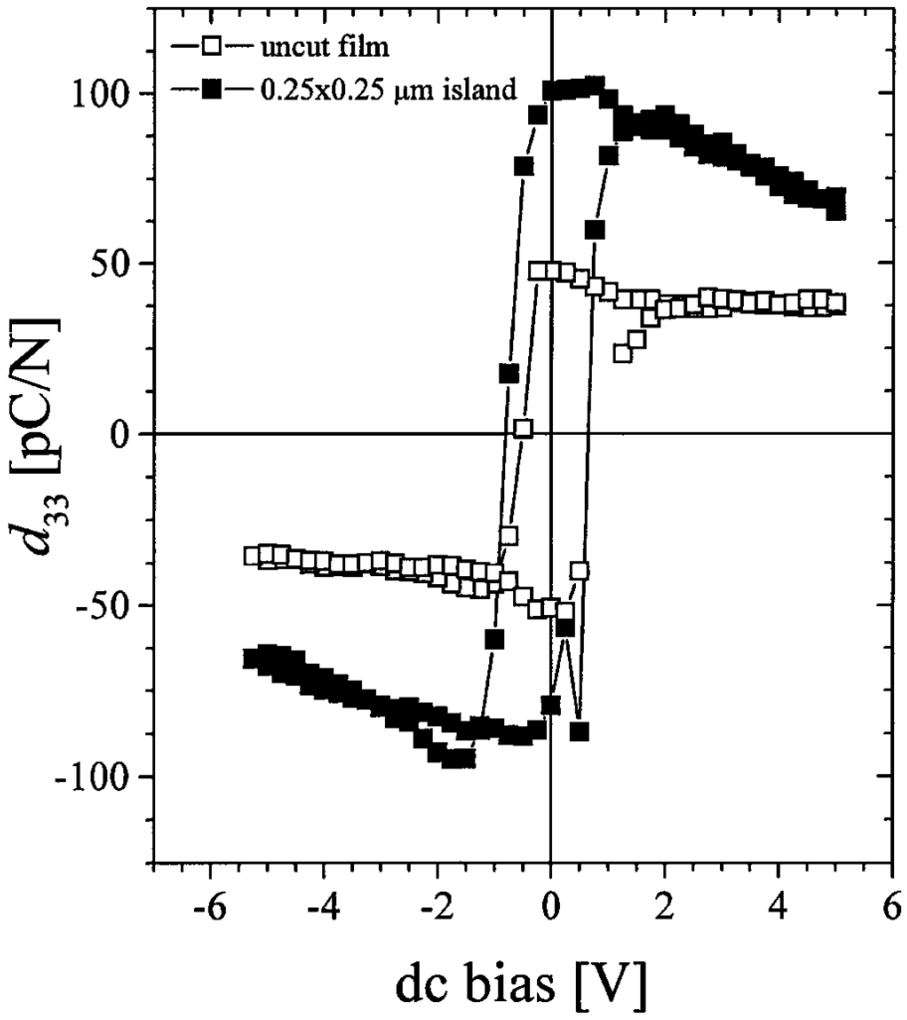

Figure 1.13. Piezoelectric coefficient d_{33} as a function of electrical voltage for a continuous 120 nm thick PNZT thin film and a 0.25 x 0.25 μm delineated island[63].

1.10 Summary

This chapter summarizes ferroelectric domains, the primary method used by other researchers to study such effects, and PFM, the main method employed in the rest of this work to investigate ferroelectric domains and their dynamics.

Chapter 2 Materials and methods

2.1 AFM

The AFM used in all experiments is an Asylum Research Cypher AFM shown in Figure 2.1, with Igor Pro software version 6.37. All experiments were performed at room temperature. The piezoactuator scanners have a maximum range in the X and Y directions of 30 μm x 30 μm extension range.

Figure 2.1. Cypher AFM in the Nano-measurement lab.

During scanning, AFM probe deflects due to various interactions with a specimen and is measured optically (Figure 2.2). Typically, RF-modulated laser diode light source module is reflected from the cantilever onto a photodiode. The position of the laser spot has been recorded to show the height change of the surface.

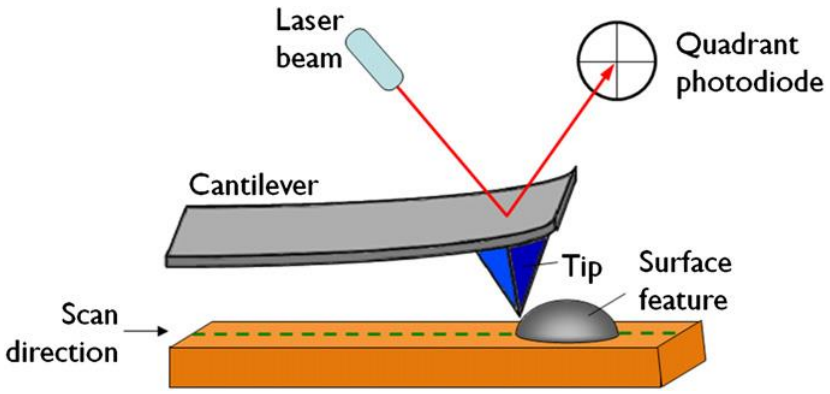

Figure 2.2. Typical AFM imaging set up[65].

2.2 Lock-in Amplifier

The Lock-in Amplifier (LIA) is a Zurich Instruments HF2 Series digital amplifier covering the frequency range between DC and 50 MHz in Figure 2.3. Small output PFM signals, along with the strong background noise, are filtered by synchronizing to the function generator AC frequency. The LIA recovers the PFM signals and amplifies to several orders of magnitude.

Figure 2.3. Stanford Lock-in Amplifier system.

LIA Amplitude (R) and Phase (θ) can be amplified by sensitivity which is based on a range of the amplitude detected. These signals are sampled by AFM electronics pixel by pixel. To calculate the lock in value into the AFM, equation 7 and 8 are used in this case. To acquire the PFM images simultaneously with topographic image and ease PFM analysis, it is significant to

consider the scaling factors while recording the amplitude and phase signal by the LIA and measure the constantly updating signals in real time with AFM.

$$\boldsymbol{Amplitude_{V,rms}} = \frac{\boldsymbol{In_0 * Sensitivity_{V,rms}}}{\mathbf{10}} \quad (8)$$

$$\boldsymbol{Phase_{degrees}} = \frac{\boldsymbol{In_0 * 180}}{\mathbf{10}} \quad (9)$$

2.3 Function Generator

The function generator utilized is an Agilent 33220A 20 MHz Function Waveform Generator (Figure 2.4). It has two primary functions: using the bias to switch or piezoactuate; as well as synchronizing the signal at the exact AC frequency from the Lock-in Amplifier.

Figure 2.4. Function generator.

AC bias detects the domain configurations by inducing the surface vibration. DC voltage can be separately applied to reverse the domain polarization only when the bias exceeds the coercive field. To simultaneously accomplish the ferroelectric domain mapping and switching, AC and DC voltage are superimposed during PFM poling. The maximum voltage which can be applied from the function generator is 10 V, at frequency range of approximately 500-2000 kHz.

2.4 AFM Probes

The primary cantilevers used in the experiments are conductive diamond coated tip[66], CDTP-NCHR and CDT-FMR, acquired from Nanosensors in Figure 2.5. The nominal cantilever length of CDTP-NCHR is 120-130 μm, with a resonant frequency of 275-720 kHz and force constant between 38-328 N/m. The CDT-FMR has longer length which is 220 – 230 μm, and resonant frequency of 80 - 130 kHz as well as force constant between 3 - 11.4 N/m. CDTP-NCHR with high stiffness was used to remove materials in nano-island fabricating, meanwhile CDT-FMR can map out the ferroelectric domains. During PFM imaging, the output voltage is applied to the tip from the function generator. The wire connected to the ground was silver painted to the back electrode.

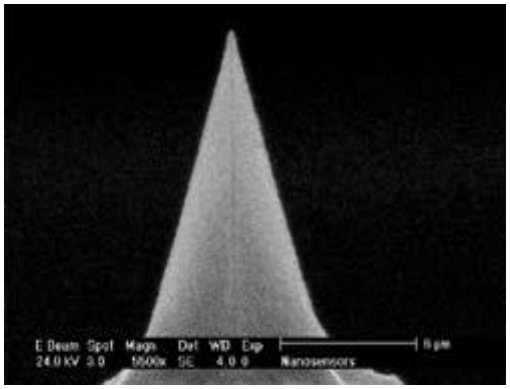

Figure 2.5. Probe shape in SEM image[67].

CDTP-NCHR is diamond coated and mechanically robust with high operation stability. The strength of this AFM probe is especially useful for milling, as probe damage is minimized. The CDT-FMR is conductive as the diamond coating is highly doped with Boron, leading to a resistivity of 0.003 - 0.005 Ohm·cm. The typical pyramid tip radius is between 100 nm to 200 nm, leading to a contact area of 10 nm region and improving the resolution. The detector side of

the cantilever is coated with the aluminum reflex to enhance the reflectivity of the optical lever detection beam.

2.5 Resonance Frequency

Resonance frequency sweep for PFM measurement has been used with external software shown in Figure 2.6 to indicate the ferroelectric amplitude as a function of frequency. The frequency is in the typical range of 300 kHz to 2000 kHz. In this figure, a strong peak can be identified at ~600 kHz driving the highest amplitude followed by several small resonant peaks. These corresponding frequencies thus can be selected for piezoelectric driving with the function generator, in order to generate the maximum piezoresponse signal[68].

Figure 2.6. An example of a Normal PFM peak.

2.6 PFM Signal

2.6.1 PFM Amplitude and Phase Signal

Amplitude images reveal details about ferroelectric properties such as the magnitude of the local piezoactuation. Domain walls with no magnitude can also be detected between two adjacent domains with opposite polarizations as the tip is above domains that are oscillating in phase and out of phase. Furthermore phase contrast usually displays 180 degrees of domains oriented directions Out-of-Plane and In-Plane.

2.6.2 Out-of-Plane and In-Plane PFM

As we described earlier, AFM cantilevers can detect the vertical vibrations perpendicular to the specimen surface with the most sensitivity. In another words, Out-of-Plane (OP) PFM measures the displacement along z axis[69, 70]. Also the lever can simultaneously monitor torque in xy plane defined as the In-Plane (IP) PFM[71]. Figure 2.7 shows the sketch of OP signal detection as the tip deflected with laser spot displacing up and down in (a); while the IP response causes torsion with shear force induced by the lateral force and therefore with laser pot moving horizontally illustrated in (b).

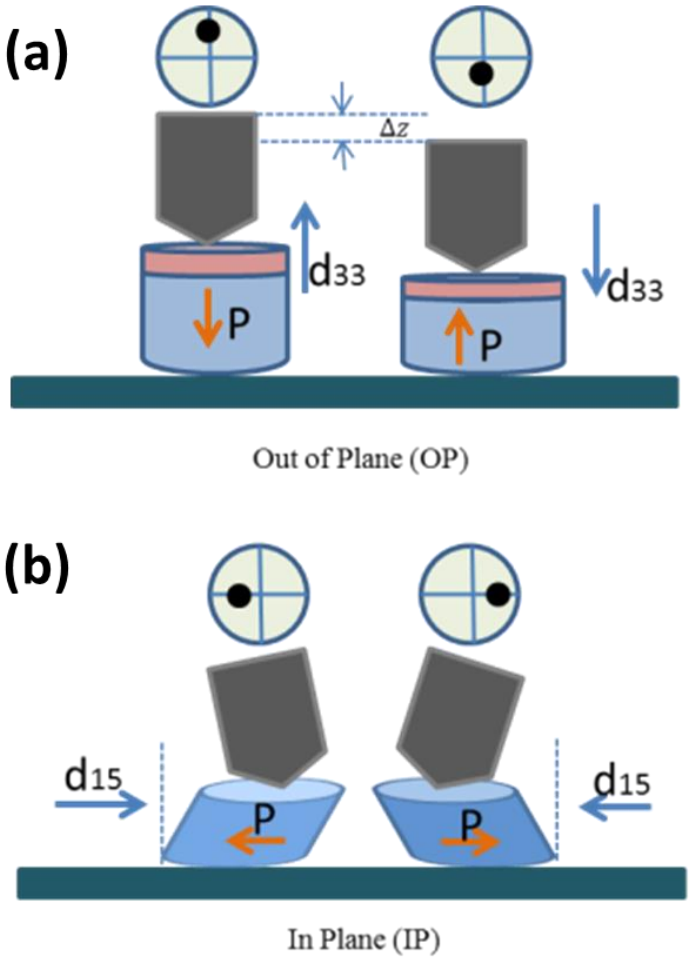

Figure 2.7. Illustration of AFM measurement: (a) shows the demonstration of the out of plane (vertical) signal; b) shows the in plane (lateral) signal.

Figure 2.8 demonstrates phase contrasts of $BiFeO_3$ for OP and IP PFM images. There are two color contrasts with 180 degrees indicating there are two domain orientations for both OP and IP images, either up or down and forward or backward respectively. Particularly, IP signal has stripe-shape domains which don't display in OP with strong contrast suggesting the OP and IP signals are independent. Note that there are atomic steps in figure (a) which is the cross-talk signal from topography.

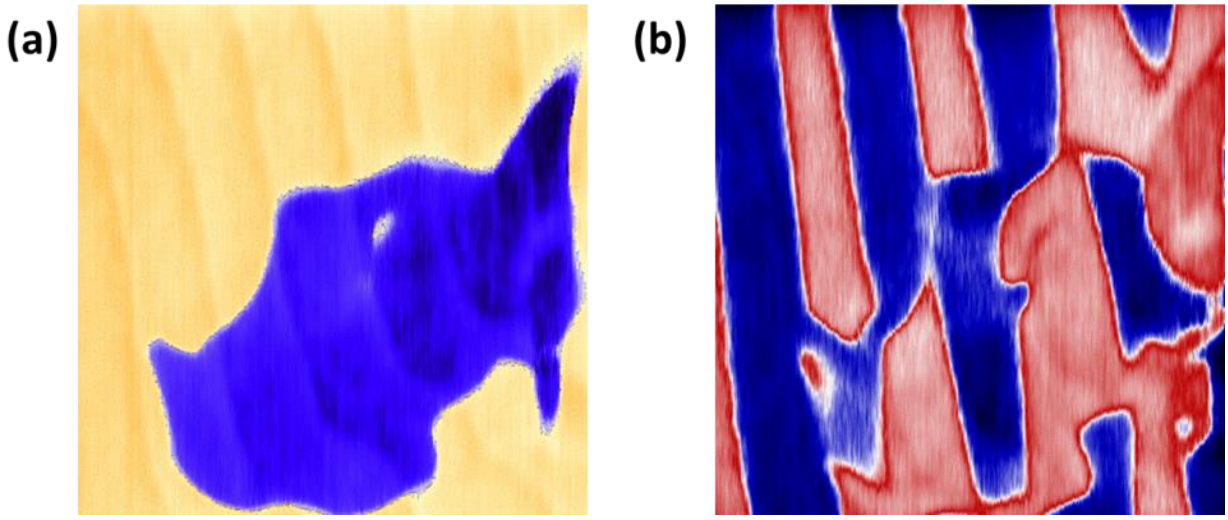

Figure 2.8. PFM phase signal for $BiFeO_3$: (a) OP and (b) IP Phase data.

To identify the configurations of such domains in 3 dimensions, the same region would need to be imaged by rotating the sample at 0° and 90° physically. By comparing the OP and IP domains with both sample mounting angles pixel by pixel, the full vector of analysis can be determined for thin films such as BFO specimen with eight possible domain orientations [72].

2.7 PZT Sample with a-domain

The sample used in the chapter 3 and 4 is epitaxial $Pb(Zr_{0.2}Ti_{0.8})O_3$ film. 90 nm PZT ferroelectric film has been grown on 12 nm $SrRuO_3$ (SRO) buffered (110) oriented $GdScO_3$ (GSO) substrates by the pulsed laser deposition technique in University of California, Berkeley, Salahuddin

group[73] in Figure 2.9. PZT thin film exhibits c domains in z axis and a-domain (90° domain) along the <100> directions due to the substrate induced strain.

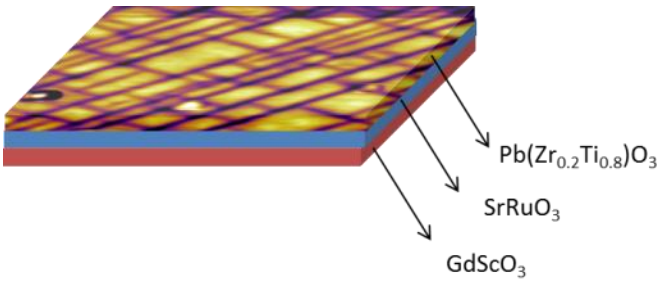

Figure 2.9. Sketch of PZT thin film composition.

2.8 PZT Sample in Compressive Strain

Another samples used is a PZT thin film from the Ramesh lab at the University of California, Berkeley. Epitaxial $PbZr_{0.2}Ti_{0.8}O_3$ (PZT) tetragonal films are grown on $SrTiO_3$ with intermediate $SrRuO_3$ conducting electrodes (Figure 2.10). The PZT is approximately 50 nm thick, so the film exhibits domains oriented normal to the surface only (no in-plane domains has been detected).

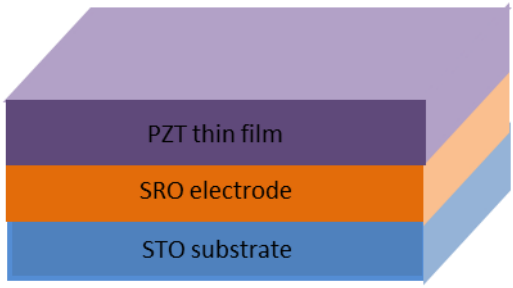

Figure 2.10. PZT thin film.

2.9 PMN-PT Thin Film

A thin PMN-PT film fabricated by the Trolier-McKinstry group from Pennsylvania State University has been studied in chapter 5. 70PMN-30PT film growth was prepared on chemical solution deposition on commercial $Pt/Ti/SiO_2/Si$ substrates. By building each layer of PMN-PT

which was ~25 nm thick repeatedly, a film with thickness of 300 nm was obtained. A 50 nm platinum top electrode was sputtered on the films and they were patterned in strip structures by lithography. The strips ranged from 9 μm to 0.75 μm in width and can be electrically excited simultaneously. The patterned PMN-PT structures were wire bonded to a Si wafer with connected silver paint for PFM measurement in Figure 2.11[74].

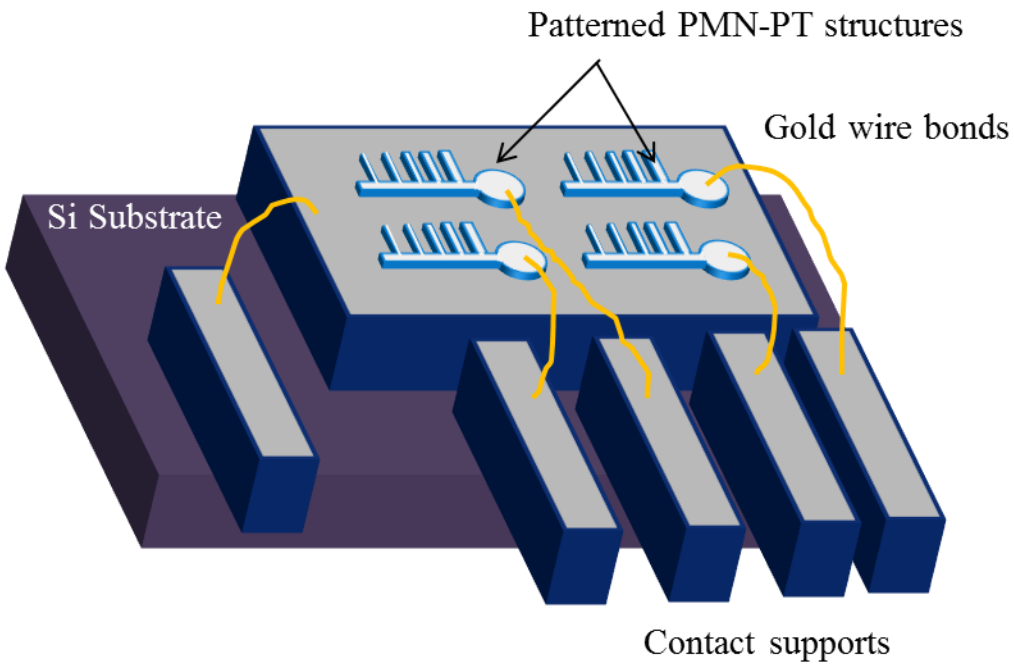

Figure 2.11. Sketch of the microfabricated PMN-PT thin films.

2.10 Summary

This chapter discusses the equipment, software and probes that have been utilized for the experiments described throughout this body of work. In particular, normal and lateral modes of piezo force microscopy are compared and details about the relevant specimens are also provided.

Chapter 3 Switching for Continuous, Strain-relieved, ferroelectric PZT thin films

Ferroelectric materials such as Lead zirconate titanate (PZT) provide numerous applications including sensors, actuators and microelectronics because of the piezoelectric response and domain configurations. These materials form ferroelectric as well as ferroelastic domains due to the stress relaxation between film and substrate[75]. Among these studies, 90° domain-wall motion particularly can lead to a strain in the order of lattice tetragonality and an enhancement of piezoelectric response compared with single crystals[76]. Several characterization techniques as X-Ray Diffraction, TEM have been applied to investigate their properties with certain limitations. Meanwhile Piezo Force Microscopy (PFM) offers great opportunity to reveal and manipulate both (180° and 90°) domain structures. More studies need to be investigated in understanding the three-dimensional domain switching in PZT thin films.

3.1 a-domain Switching

Here, we utilize Piezo Force Microscopy (PFM) to visualize the ferroelectric and ferroelastic domain switching in epitaxial $Pb(Zr_{0.2}Ti_{0.8})O_3$ film. 90 nm PZT ferroelectric film has grown on 12 nm $SrRuO_3$ (SRO) buffered $GdScO_3$ (GSO) substrates[73]. Previous theories of lattice mismatch would be accommodated entirely by strain within the film below certain thickness of the film[77]. This PZT specimen has a tetragonal crystal structure below Curie temperature (Tc) while GSO is pseudocubic. Thus the film assumes a heterogeneous phase containing periodic alternating a and c domains with 90° domain walls to reduce the strain energy when the thickness is below 250 nm. The calculated results indicate that the film appears to be fully relaxed by

dislocations for thicknesses above 250 nm[78, 79]. This PZT thin film exhibits c domains in tetragonal axis and a-domain (90° domain) along the <100> directions due to the substrate induced strain. A 0.96% tensile strain has been created to PZT, keeps the slanted a-domain and tetragonal c-domain at steady state.

The voltage control of ferroelastic domains in the PZT thin film has been previously reported[73]. The electric field induced ferroelastic c—a switching was observed without the ferroelectric 180° domain switching occuring by using PFM technique sketched in Figure 3.1.

.

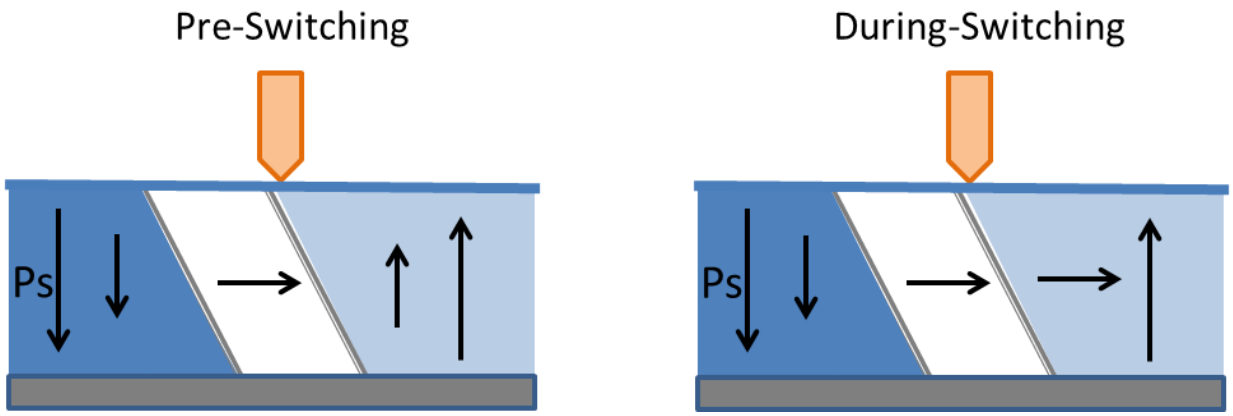

Figure 3.1. Sketch of c domain switching to a-domain under tip bias.

We also achieved the ferroelastic 90° domain switching process with the absence of 180° c-domain switching with higher resolution by PFM. Figure 3.2 shows the consecutive switching images under DC bias.

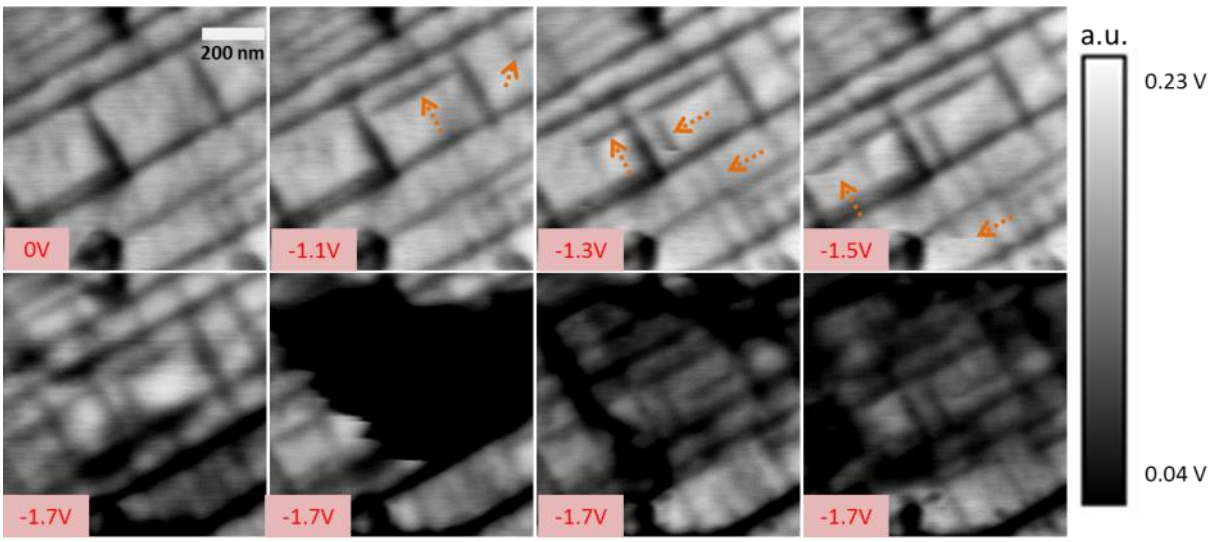

Figure 3.2. PFM out-of-plane switching in 800 nm x 800 nm amplitude image: The regions where ferroelastic a-domain created are indicated by yellow arrows.

Figure 3.2 shows the out-of-plane PFM images of a 90 nm PZT film. In as-grown state (0 V), a-domains appear as slanted needle-like shape. We applied DC voltage superimposed with 3 $V_{ac\ peak\ to\ peak}$ on this 800 nm x 800 nm region to reveal the response via a conductive diamond probe (CDT-FMR). After -1.1 Vdc applied to the entire region, the first new a-domain has been created by comparing to the original state at the same area as indicated by the yellow dashed arrow. More a-domains formed when the voltage increasing to 1.3 V. No concurrent of c-domain ferroelectric switching has been observed in the image before 1.7 V where a-domain switching happened. 180° c-domain switched along the direction parallel to the voltage applied and perpendicular to the PZT/ SRO interface when the external voltage reached 1.7 V. The coercive voltages for the c-domain switching vary from spot to spot since the domain reversal is not simultaneous as shown at the bottom row of PFM out-plane images. The PFM image sequences suggest the threshold voltage for the ferroelastic c-a domain switching is ~ -1.1 V while the coercive voltage for ferroelectric switching is ~ -1.7 V, proposing the fact that ferroelastic switching could happen without the concurrency of ferroelectric reversal.

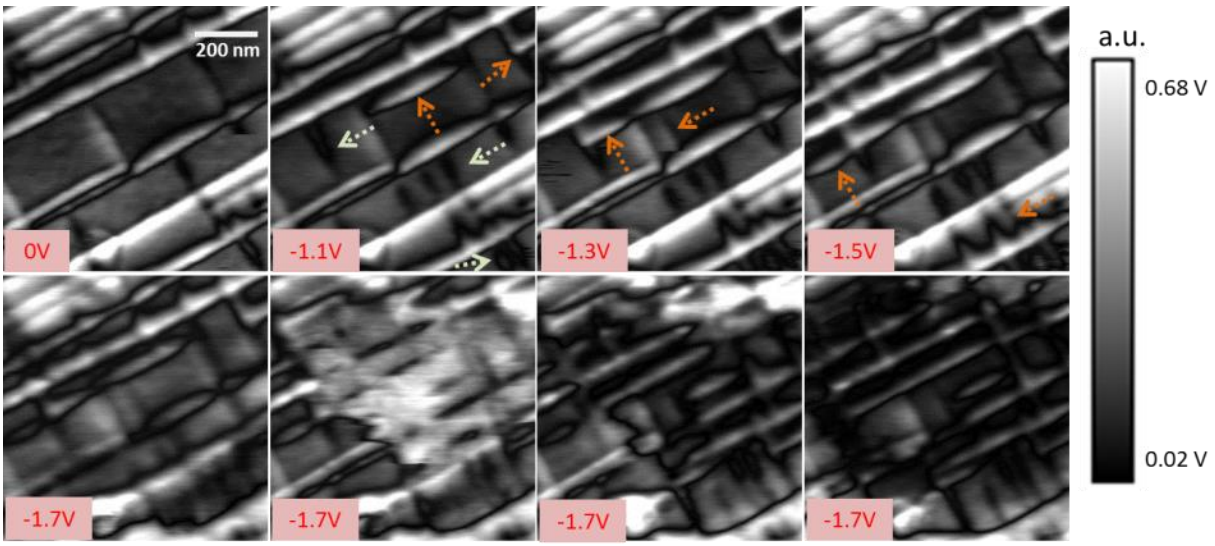

Figure 3.3. PFM In-Plane switching in 800 nm x 800 nm amplitude image: The regions where ferroelastic a-domain created are indicated by yellow and green arrows.

Figure 3.3 shows the In-Plane ferroelastic switching occurrence without the coupled ferroelectric switching at the same spot. Again yellow dashed arrows point out the newly formed a-domain at each voltage applied image. By carefully analyzing the In-plane response, a-domains have been created at -1.1 V as shown in the corresponded Out-of-Plane image. Surprisingly In-Plane image reveals more new a-domain indicated by the light green arrow comparing to the Out-of-Plane data acquired at the same time. This fact proves In-plane signal can resolve fine domains at higher resolution which has not been reported before.

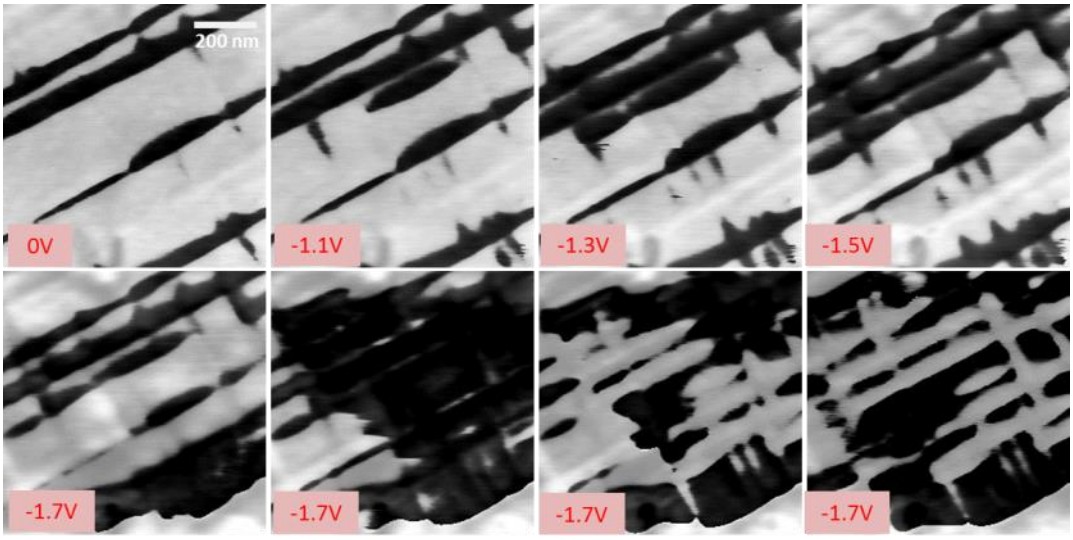

Figure 3.4. PFM In-Plane phase switching in 800 nm x 800 nm image.

The polarization orientation in a-domains has also been mapped out by measuring the in-plane phase signal in Figure 3.4. These phase images exhibit the lateral torsion of the AFM cantilever recorded in the photodiode as the tip scans over the region. Black and white color contrast given in Figure 3.4 represents those a-domains with opposite polarized orientations as suggested in Figure 3.5.

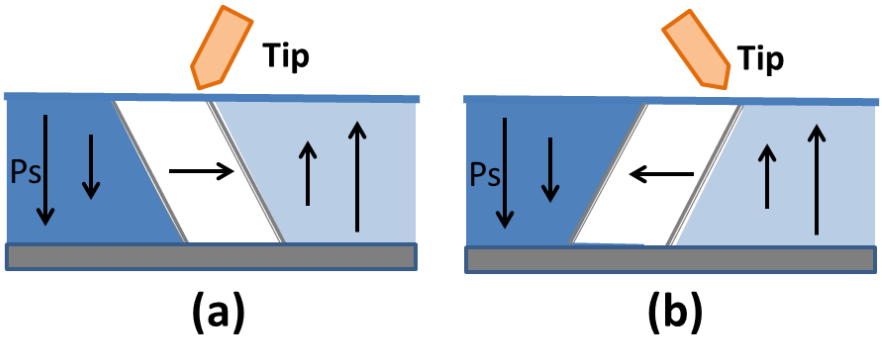

Figure 3.5. Tip torsion when scanning over a-domain with reversed orientations in (a) and (b).

Furthermore, we can explore switching energy per pixel and how it couples to various microstructural features for OP and IP signal. In this 800 nm x 800 nm region, light blue area has been switched with only ~0.15 eV while red area requires activation energy as high as ~ 0.3 eV

in Figure 3.6 (a) for OP switching. Figure 3.6 (b) shows the blue and green spot would switch in-plane before the red spot since the energy barrier is smaller. Thus which domain has come up first is clarified. Importantly and unexpectedly, some a-domain switching is clearly independent of c-domain switching for these films. Separate work by Ramesh and Martin suggests that these a-domain nucleation sites are buried under zero voltage conditions, and that a-domains are drawn towards the free surface upon appropriate poling such that the map of Figure 3.6 (b) may primarily indicate the surface energy landscape corresponding to heterogeneities in this mechanism[80].

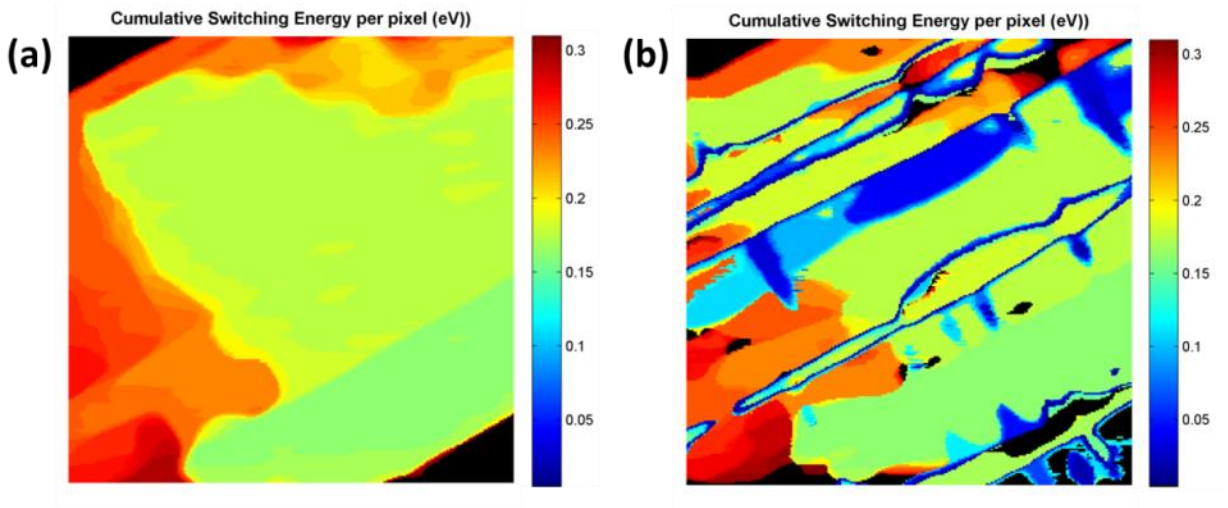

Figure 3.6. Switching energy per pixel for OP switching (a), and IP switching (b).

3.2 a-domain Formation Relating with Height Difference

It has long been observed that there should be a change in the local height for local polarization rotations (as opposed to 180° switches). For example, Ganpule etc. reported topographic steps when scanning across an a-domain, as illustrated in Figure 3.7[81].

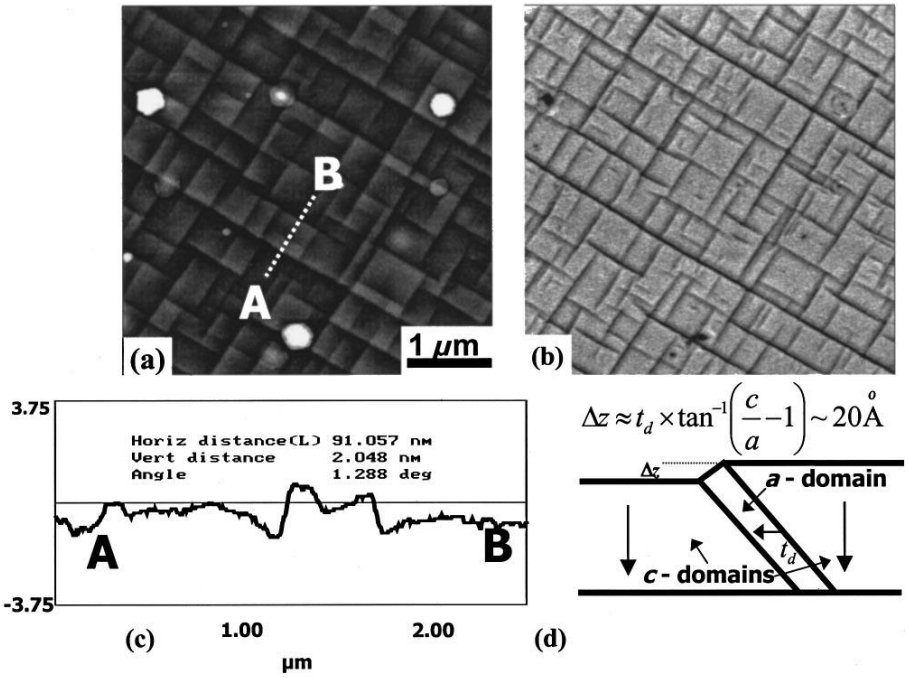

Figure 3.7. (a) Topography and (b) piezoresponse images taken simultaneously for a relaxed PZT thin film. (c) A line scan across AB reveals step edges at the a-domain interfaces, explained by the schematic (d) of the surface relief for a single a-domain[81].

Extending this concept to movies of switching processes, the development of a-domains during poling should be resolvable by topography as it is with PFM for Figures 3.3 and 3.4. Accordingly, Figure 3.8 presents out of plane images before (a) and after (b) development of a new a-domain, alongside the corresponding topography (c and d, respectively). Cross sections along the vertical line, through this new domain, are displayed in (e) and (f).

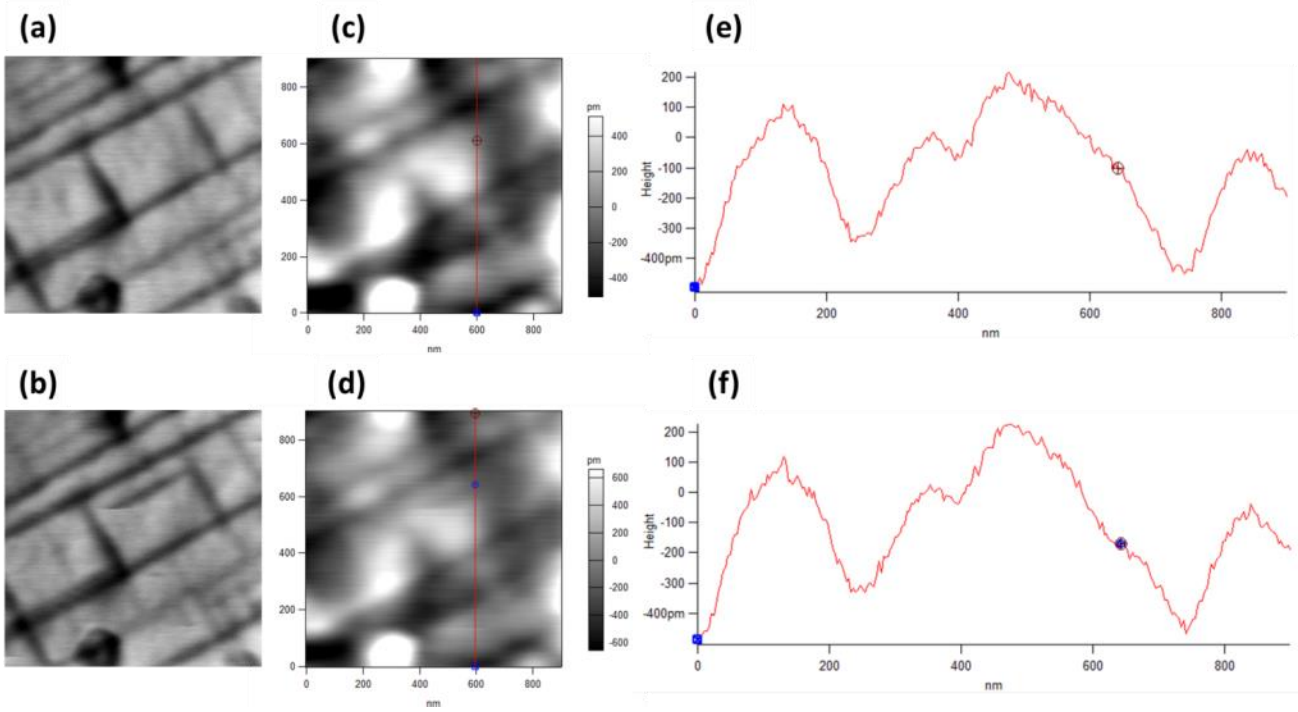

Figure 3.8. PFM out-of-plane image of amplitude before and after a-domain switching (a) and (b); corresponding topographic height (c) and (d); AFM line trace (e) and (f) across the region in (c) and (d).

To better visualize the subtle difference in height between Figure 3.8 (e) and (f), Figure 3.9 overlaps these cross sections and reveals perfect agreement except for a ~1Å step at the new a-domain location. This amounts to a local strain of ~0.1% for the 90 nm film. While the signal to noise ratio for resolving a-domains in this manner is not as strong as it is for pfm imaging, this nevertheless suggests a possibly useful approach for future efforts at simultaneous normal and in-plane domain mapping (which is definitely not easy). This is because a-domains can be distinguished by carefully tracking topography, while out of plane PFM is easily performed for c-domain switching.

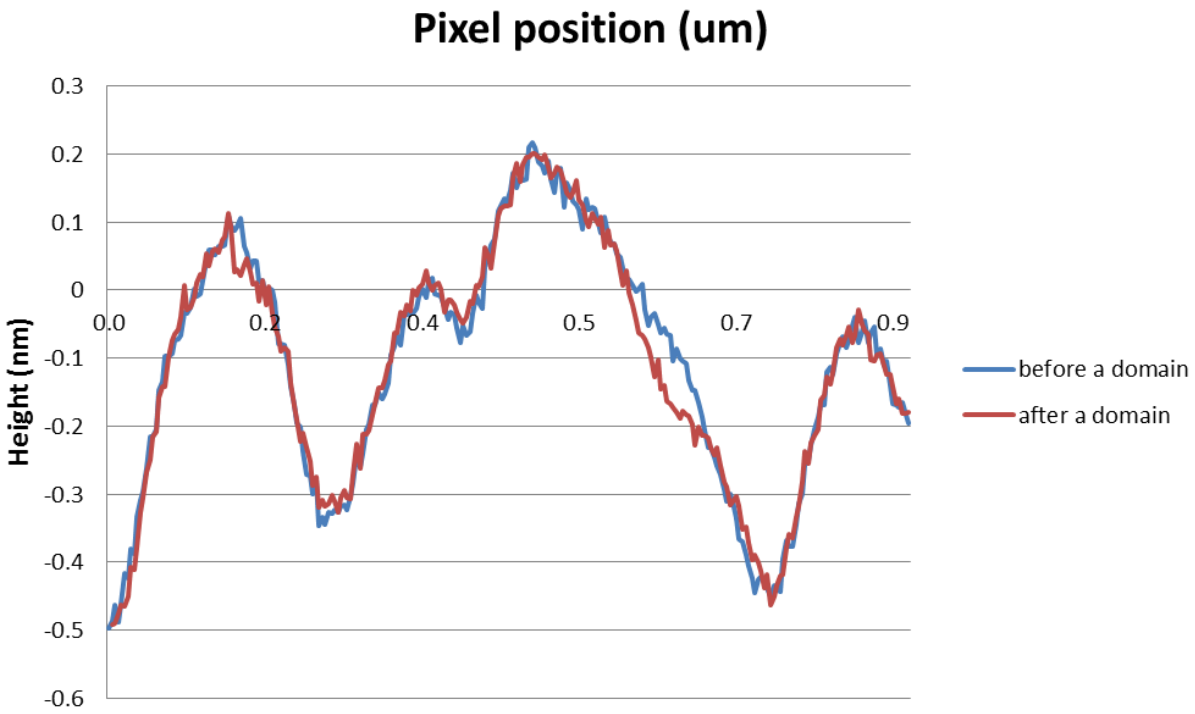

Figure 3.9. Height plot before (e) and after (f) a-domain formation.

3.3 Summary

This chapter describes a-domain formation without a concurrent c-domain switch, according to simultaneous Out-of-Plane and In-Plane PFM. 90° switching (c domain to a domain) energy as well as 180° switching (c^+ domain to c^- domain) energy have been calculated, and the energy barrier for 90° switching is smaller than 180° switching. Moreover, a change in surface height caused by local strain can be related with a-domain switching, suggesting a future approach for resolving such domains by topography tracking instead of PFM. Therefore, a-domain and c-domain switching can be monitored via PFM mode as well as topographic information to provide insights into future domain engineering devices and ferroelectric cell writing.

Chapter 4 Nano-Sculpted Polydomain PZT

The ferroelectric and piezoelectric properties of thin films are often diminished from the bulk. This can be due to substrate clamping effects, such as decreasing tetragonality for c-axis domains. It also can result from strain relief mechanisms, such as the formation of orthogonal a-domains, which decrease the volume fraction of properly oriented c-domains. One common method to address this challenge is to relieve strain via nanostructured instead of continuous epitaxial films.

To prepare such specimens, standard semiconductor industry microfabrication routes are commonly applied, including top down etching or lift-off procedures, as well as straightforward deposition of isolated islands via bottom up growth procedures. In many instances, though, FIB milling is much simpler to achieve due to its straightforward operation[82].

4.1 Focused Ion Beam Processing

The patterning of ferroelectric film has drawn much interest as nanoscale features with high aspect ratios of thickness : area have demonstrated enhanced piezoelectric properties[83]. It is crucial to develop a method to continue to shrink dimensions, and to reduce common sidewall damage that is caused by many patterning processes. The most common is Ga^+ ion Focused ion beam (FIB) milling, reported by A. Stanishevsky to enable fabrication of PNZT-based capacitors via direct material removal and thus fabrication of nano-islands down to 130 nm on a side[84]. The depth of materials removal is up to 400-500 nm. An example is shown in Figure 4.1, which demonstrates square features (4, 1, or 0.25 μm^2 on a side) exposed by milling surrounding trenches.

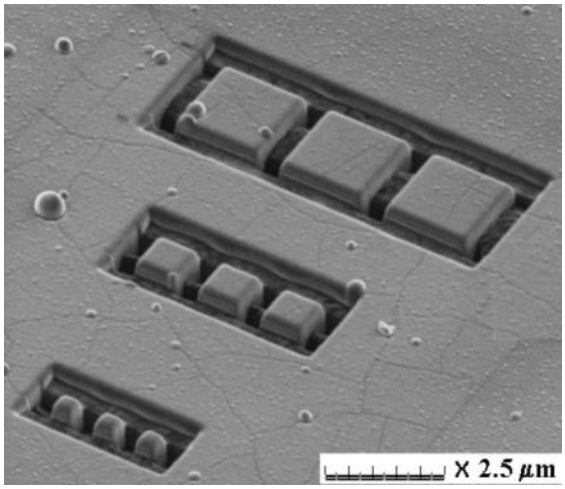

Figure 4.1. PNZT structures with the sizes of 4, 1, and 0.25 μm^2, milled by FIB[84].

However, FIB processing can cause structural damage and ion implantation. A. Schilling etc. observed gallium ion implantation as well as the loss of lead and oxygen at the damaged region[85]. Figure 4.2 shows the surface of the PZT layer at original state in (a) and after FIB processing with accumulation of Ga^+ ions revealed as bright spheres in (b)[86].

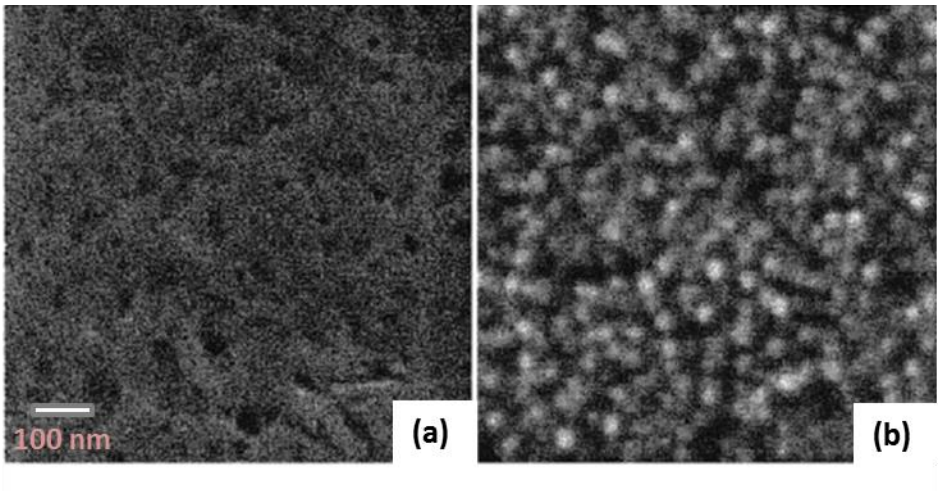

Figure 4.2. Image showing the initial surface of the PZT layer (a), and the post-FIB surface with bright spots indicating Ga formation (b)[86].

Despite FIB milling using Ga^+ allows obtaining nano-size PZT structure, such milling introduces gallium ion implantation to the film, resulting in shifted or collapsed ferroelectric hysteresis

loops, and even loss of ferroelectricity. Moreover, post annealing process is required for patterned features to partially recover ferroeletric properties after FIB[86].

As an example of post annealed FIB-prepared ferroelectric microstructuring, Nagarajan etc. reported the increase of polarization response for micro-scale islands fabricated using Ga+ focused ion-beam (FIB) milling as shown in Figure 4.3 [76].

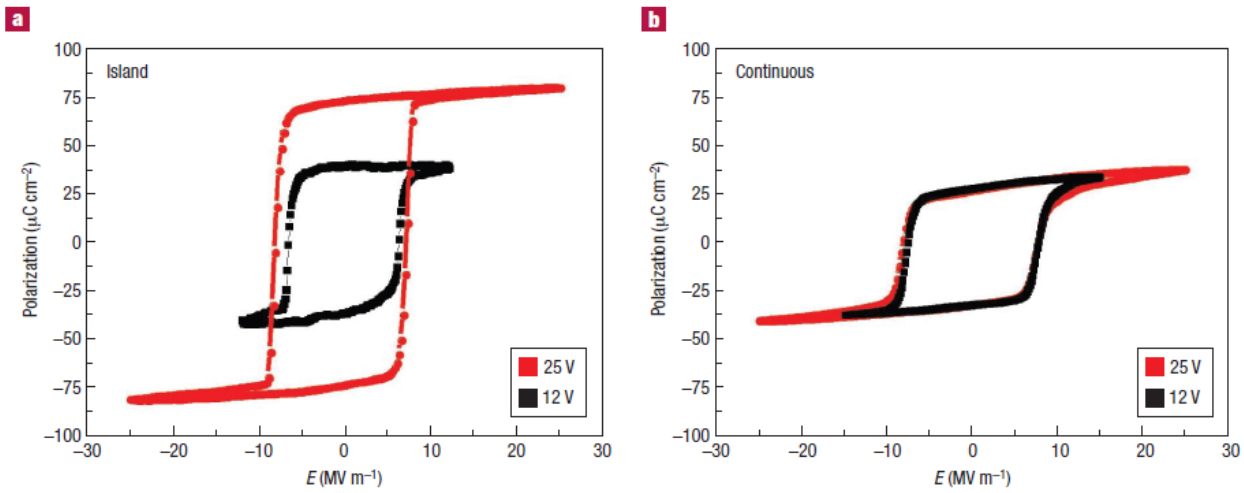

Figure 4.3. The effect of the movement of ferroelastic domains on the polarization response of a nanostructured island (a) compared to a continuous film (b).

4.2 Nano-sculpting Technique

In this chapter, we present a unique technique of fabricating nano islands to obtain desirable sizes and strain relief with minimal structural damage: Nano-Sculpting. Unlike FIB that entails complicated procedures and high costs, an extremely stiff diamond probe (CDTP-NCHR) has been employed here in AFM scanning to reveal mesas down to 200 nm^2 on a side. With a force constant of 125 N/m, this probe can easily abrade materials at high AFM force load with high speed, as well as image topographic features. Additionally, it is much easier to operate for beginners and customize island size and configurations in various ways. For instance, Figure 4.4 (a) and (b) demonstrates six relieved islands in an image 8 μm on a side via using the Nano-

sculpting methodology. The six ~2 µm x 3 µm sized islands were created in this manner in only ~70 minutes based on ~90 nm deep surrounding trenches.

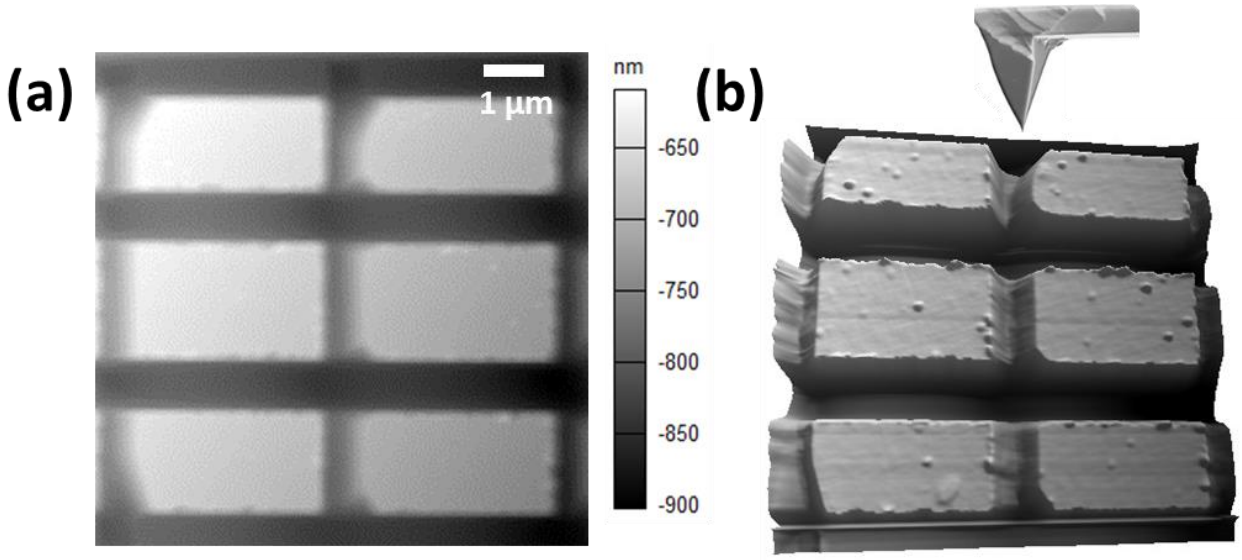

Figure 4.4. AFM height image of 6 islands (a); 3d sketch of the probe and islands after milling (b).

To illustrate how the mesas are formed, Figure 4.5 depicts successive steps in milling channels in an initially continuous film, opening up gaps 80 nm in depth and ~ 500 nm in width. By setting the imaging ratio of width to height to 16: 1, we constantly scanned the same regions with applied forces as high as ~28000 nN due to the hardness of the PZT thin film. This resulted in gradual removal of the local film, which was then repeated to prepare seven overall trenches and hence six mesas with equivalent sizes and shapes.

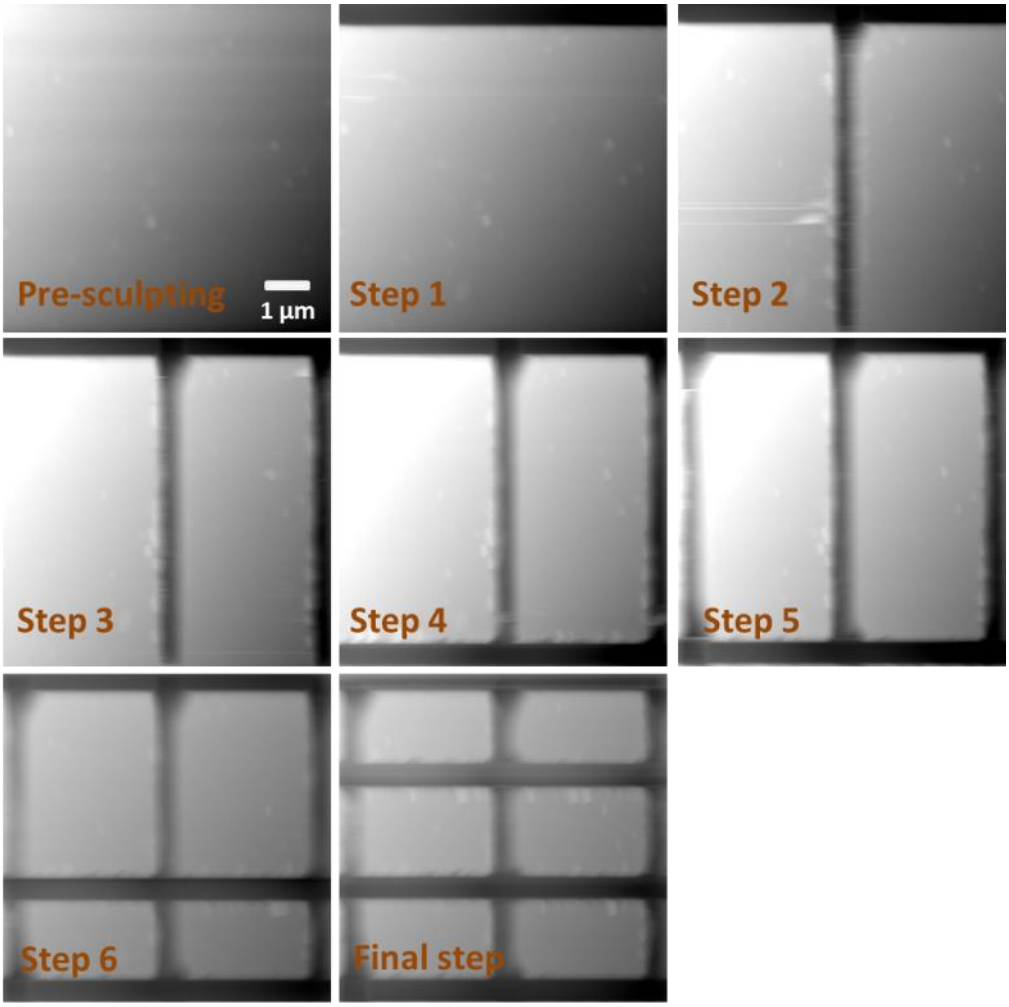

Figure 4.5. Steps to mill materials and generate mesas using nano-sculpting technique.

By using the same strategy, we also designed and prepared a 4x4 array of mesas in a PZT thin film to create 16 identical mesas with sizes of ~ 500 nm on a side as shown in Figure 4.6. As the radius of the tip is appoximately 100 nm and it has a conical shape, the individual mesa would possess a pyramidal structure when the lateral dimension gets much smaller. This technique allows us to study the ferroelectric properties of thin films at high ratio of lateral dimension vs. thickness, which may plays an important role in strain engineering.

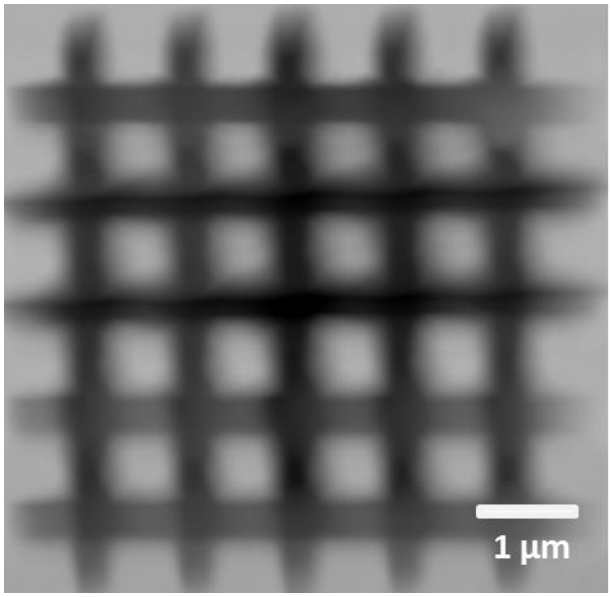

Figure 4.6. 16 islands fabricated in PZT thin film.

4.3 Pre and Post Sculpting

To further explore this probe milling method would affect the domain and switching dynamics, a careful experiment has been conducted on the PZT thin film by tracking the PFM signal before and after milling, Figure 4.7. A 1.5 µm x 1.5 µm island is delineated with surrounding films removed. Pre-milling, the OP signal was recorded, while post-milling OP signal was again studied for comparison, Figure 4.7 (a) and (b). The dashed rectangular overlay in (a) identifies the region corresponding to the microscale island in (b), proving that no appreciable changes occurred during the milling process for the a-domain patterns. Figure 4.7 (c) shows a topography image of this island with approximately 50 nm height difference.

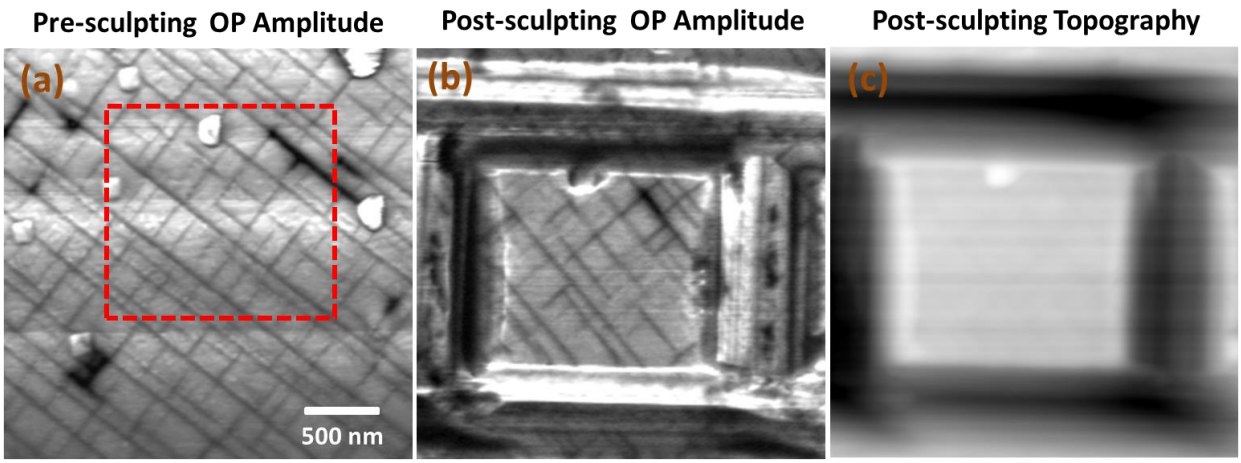

Figure 4.7. OP amplitude image before (a) and after (b) milling; AFM height image of the fabricated island (c).

The intricate a-domains remain after formation of the finely scaled micro-mesa of PZT. The contrast for some of the finest domain walls is difficult to detect, but this is not surprising since the post-images are acquired with the same AFM probe as the pre-images, and there is always the possibility of some change (worsening) in tip shape during the nanosculpting process.

This mesa has been fabricated at medium milling speed by applying relative small force. To accelerate the sculpting speed, a much higher force was applied to pattern mesa in a less time-consuming way in Figure 4.8. OP amplitude pre and post milling has also been shown in Figure 4.8 (a) and (b). Comparing with the milling time of mesa shown in Figure 4.7, it took approximately one third of the time to fabricate mesa in Figure 4.8. While not apparent in (c), there is possible evidence in the post-milling PFM image Figure 4.8 (b) of the formation of a sub-surface crack, presumably induced by the mechanical processing step. Such features have only been observed in approximately 5% of mesas fabricated as part of this body of work. The example in this figure is selected to highlight the possibility of damage of high speed and even sub-surface sensitivity of PFM, but is not the norm.

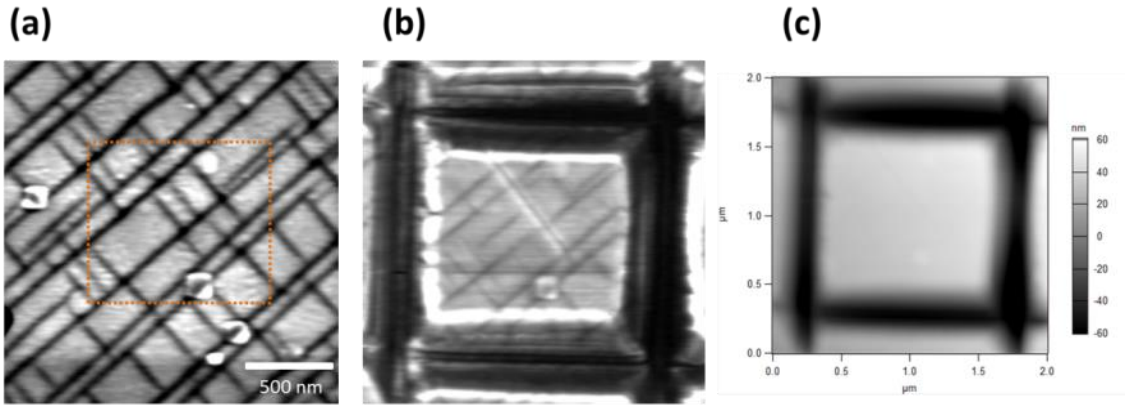

Figure 4.8. OP amplitude image before (a) and after milling (b); AFM height image of the fabricated island (c).

The domain switching dynamics were next monitored as in Chapter 3, by applying a 3 $V_{peak\ to\ peak}$ AC bias plus successively greater DC voltages as shown in Figure 4.9. When applying -1.35 Vdc, the fabricated mesa has just started to switch from the edges, possibly due to partial declamping from the substrate. There suggests that the nano-sculpting process does not cause domain wall pinning at the sidewalls, otherwise switching be expected to be hindered at these edges instead of initiating there. The apparent crack, on the other hand, clearly impedes domain wall motion and full switching of the mesa, which is finally only completed once the voltage reaches -2.2 Vdc.

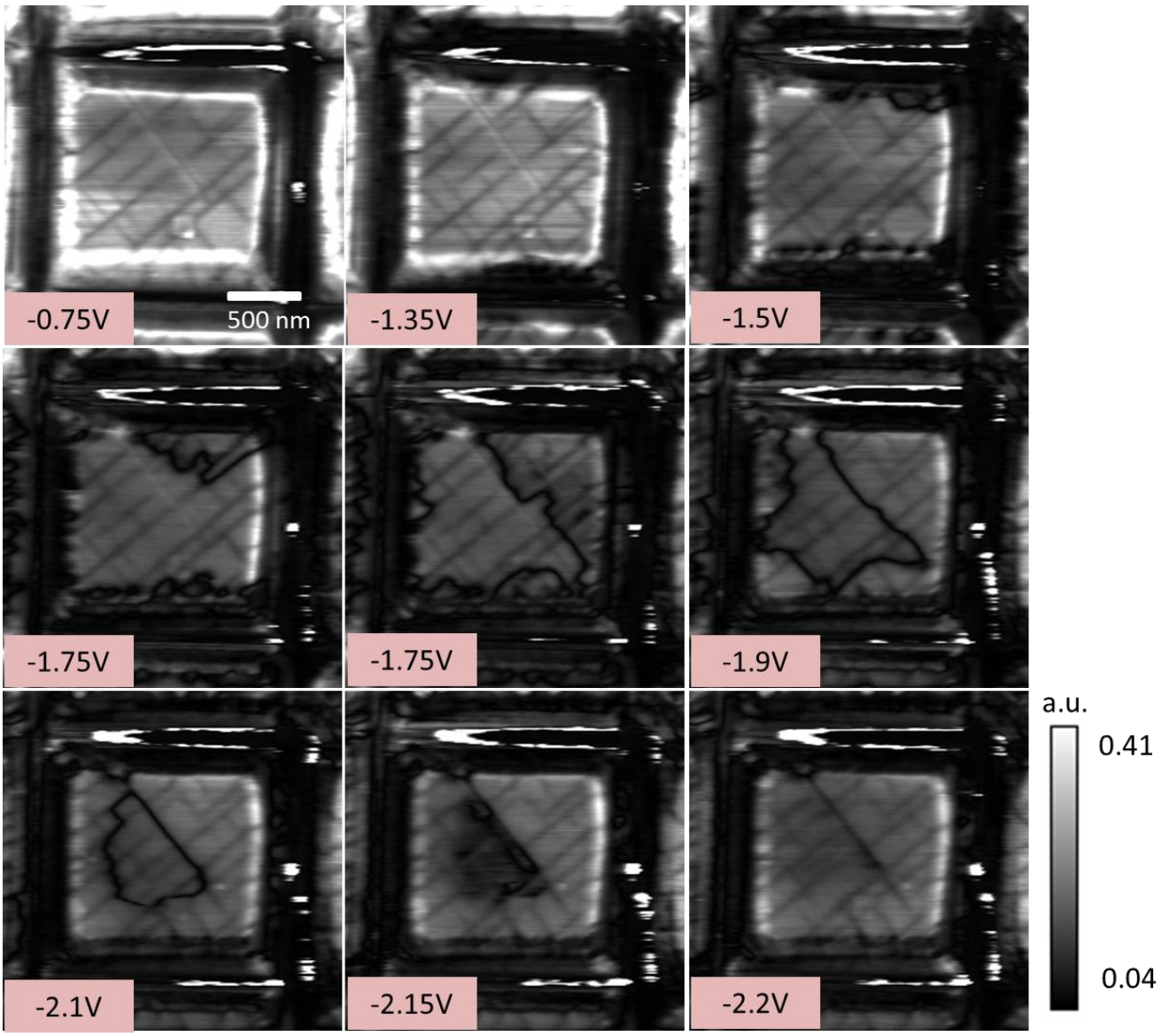

Figure 4.9. PFM OP domain switching at different voltages.

To prove that nano-sculpting does not damage bipolar ferroelectric switching, Figure 4.10 demonstrates complete switching first in the negative direction, then positive, then negative again. Each excursion upon negative biasing follows essentially the same pattern, with growth from the feature edges towards the center, hindered by the apparent sub-surface crack. During the ferroelectric switching cycle of negative-positive-negative voltage, switching dynamics is stable and hysteresis loop is not disturbed.

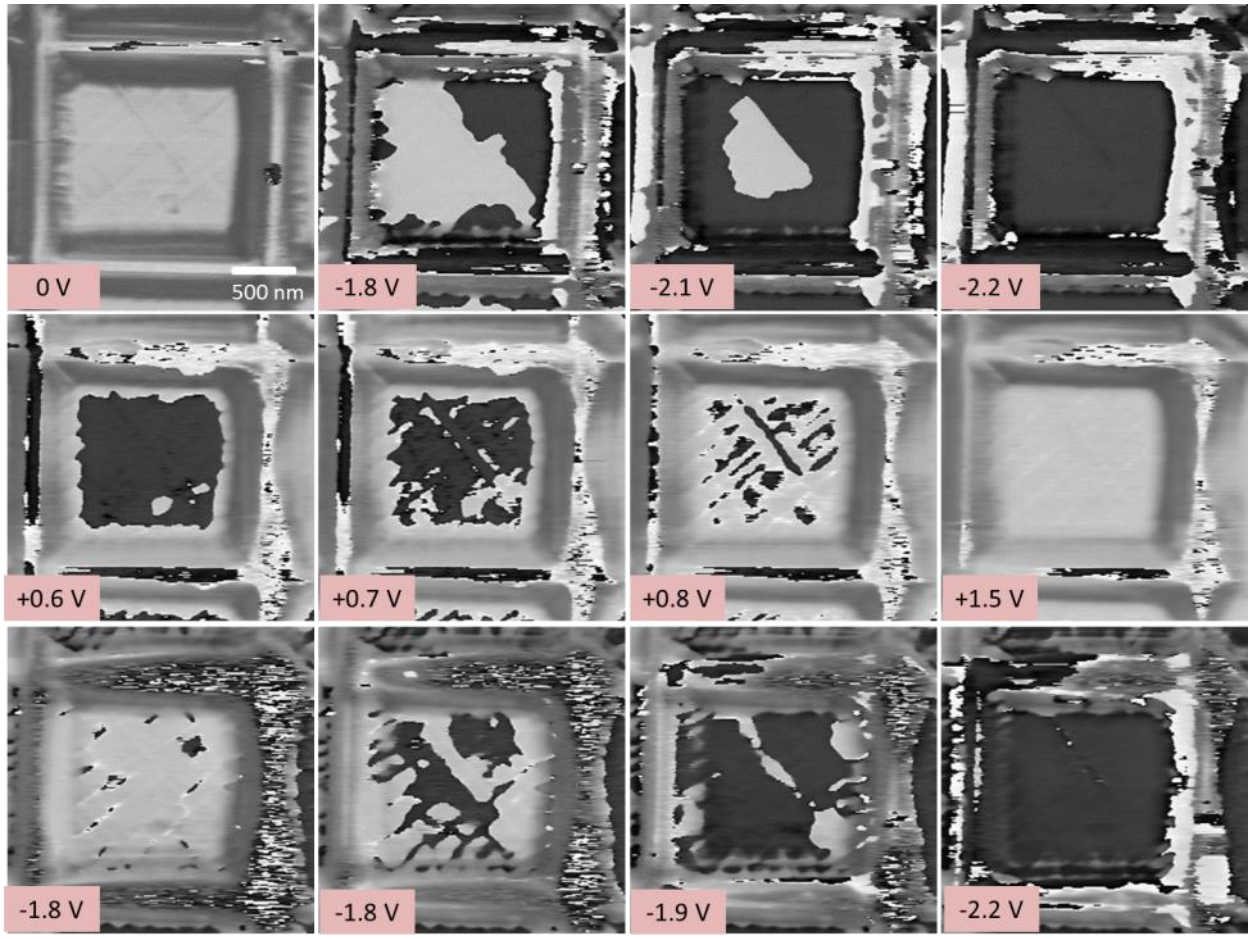

Figure 4.10. OP phase images of switching process upon positive and negative voltages of PZT thin films.

4.4 Six Mesa Switching

Extending the approach presented above, but also investigating in-plane a-domains which may be more sensitive to domain wall pinning, a set of 6 additional mesas were prepared. Following

nanosculpting, their OP and IP pfm signals are displayed in Figure 4.11 (a) and (b). Both c- and a-domains have been observed without dramatic deformation.

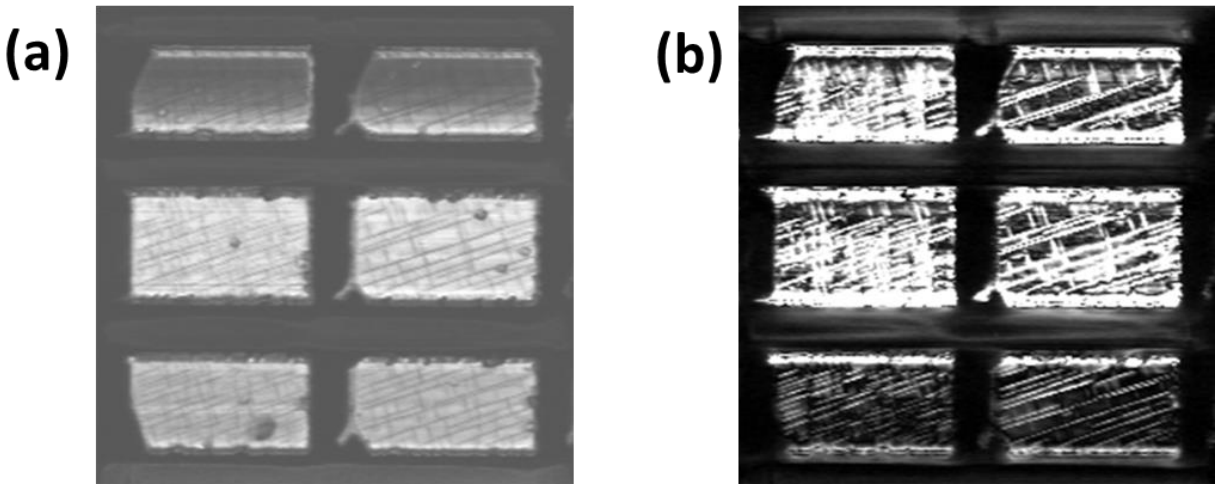

Figure 4.11. OP (a) and IP (b) amplitude images of the 6 mesas.

The two mesas in the center of the images were found to be able to be switched in the normal direction. The rows of mesas at top and bottom, however, could not be poled as the adjacent milling was apparently sufficiently deep that it even removed the surrounding back electrode and hence electrically isolated these 4 microstructures. Focusing just on the central row of still-active mesas, then, Figure 4.12 (a) presents a sequence of 12 images taken from a longer movie of switching, again confirming that the islands are still ferroeletric. Nucleation and growth begins once more at the periphery, though proceeds at different rates perhaps related to simple heterogeneities in the spatial and energetic landscape for nucleation. The number of frames to initiate this OP domain switching has been mapped for each pixel in Figure 4.12 (b). Most domains have switched in just 3 frames for the left island; while half of the domains only started to switch after 10 frames for the right island. No obvious strain relief benefits are present in the images, as expected both because the films are somewhat strain relieved by in-plane domains already, and also because the mesas are rather large. This leads us to the exploration of finer island, with an area less than 1.5 μm^2.

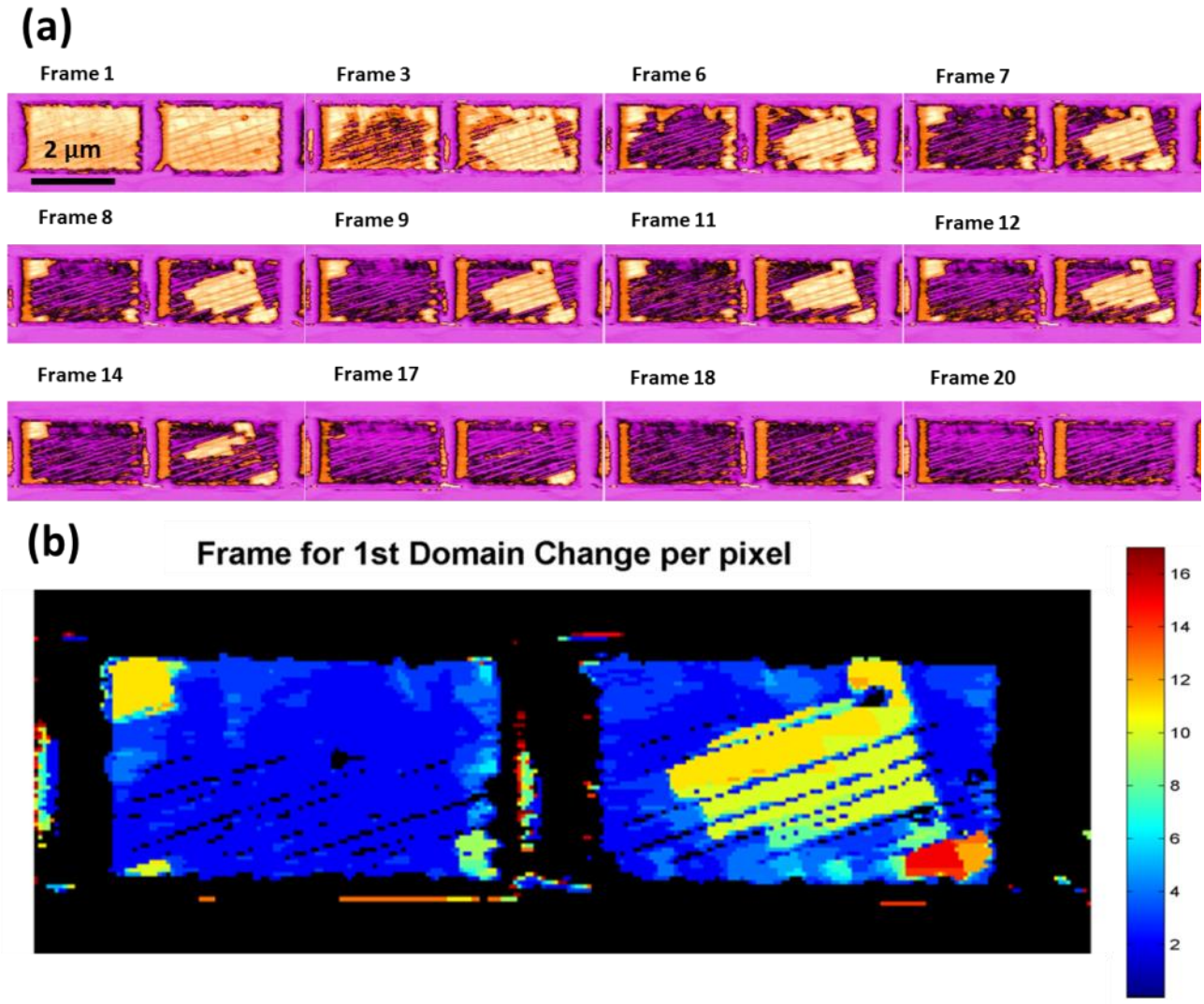

Figure 4.12. (a) PFM amplitude image sequences of OP switching under external voltage in 8 µm x 8 µm area. (b) Imaging frames taken for the first domain switching at each pixel.

4.5 Piezoelectric Enhancement on Edges

Previous report of the antennae structure enjoys an improvement at the edges due to strain relief[87]. This fact has also been approved on PZT thin films. A ~1 um^2 island with almost complete strain relief has been examined via PFM, OP amplitude signal was recorded in Figure 4.13 (a). It illustrates a strong enhancement of piezo response on four edges, compared with the rest of this isolated nano island. The edges are the most unclamped area, while the center area

has the least strain relief. This is remarkable given the fact that piezo response has been studied many times, but no direct amplitude enhancement has been mentioned.

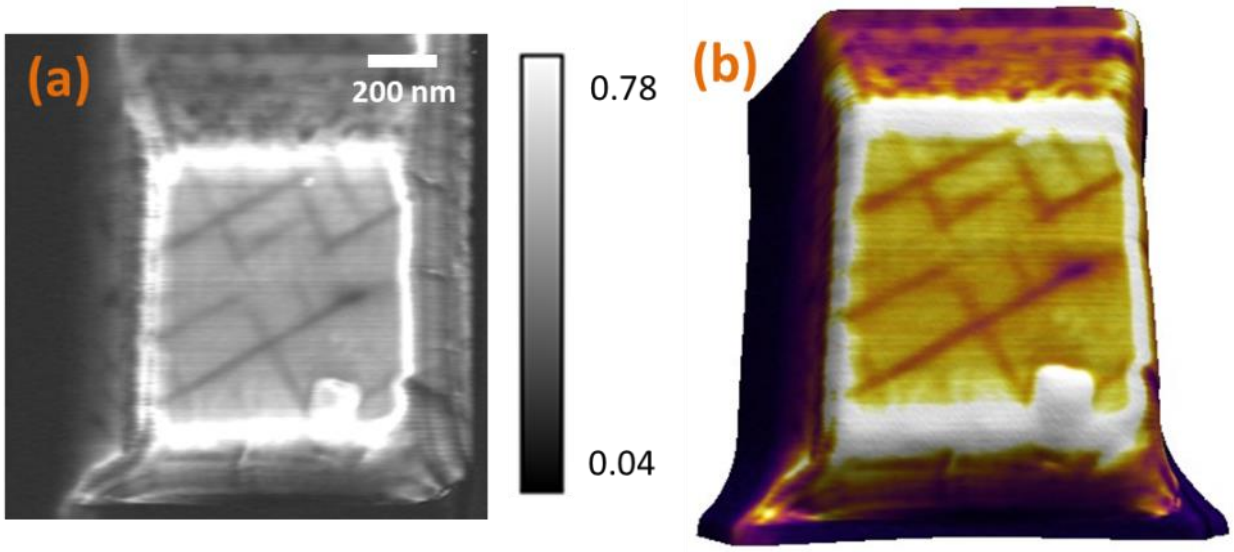

Figure 4.13. PFM amplitude image showing the enhancement on the edges in the 1.4 μm x1.4 μm region (a); 3d montage (b) of amplitude image (a) superimposed on a 3-dimensional depiction of the topographic height.

The size of the finest island structure can be as small as 0.16 μm^2 via this technique. Figure 4.14 illustrates a 400 nm x 400 nm nano island with a strong proper ferroelectric response.

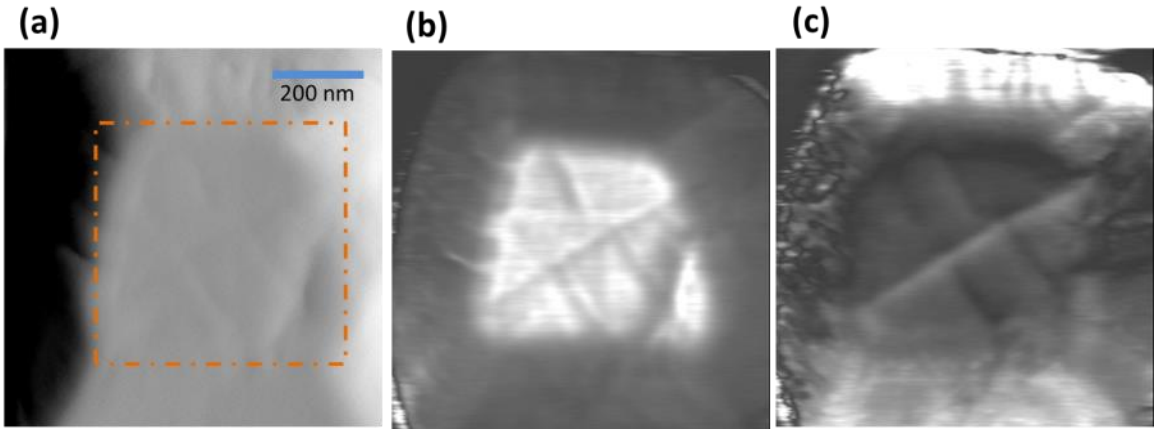

Figure 4.14. Deflection (a), OP amplitude (b) and IP amplitude (c) for PZT nano island.

4.6 Nine Mesas Switching with Various Strain Relief

For the PZT/$SrRuO_3$/$GdScO_3$ thin film, in the absence of in-plane domains the in-plain strain can be calculated based on mismatches in the lattice parameters between the film and substrate. The lattice parameter for GSO is 3.968Å, for the intervening thin back electrode SRO is 3.93Å, and for PZT is 4.036 Å as shown in Figure 4.15 (assuming $SrRuO_3$ and $GdScO_3$ are elastically isotropic). Thus the film inherently experiences a large tensile strain from the substrate clamping, which is partially relaxed by the formation of in-plane domains. By applying the nano-sculpting approach, further strain relaxation can take place causing local changes in the piezoelectric and ferroelectric properties.

$$\varepsilon_{xy}=\frac{a_{GSO}-a_{SRO}}{a_{GSO}}=\frac{3.968\text{Å}-3.93\text{Å}}{3.968\text{Å}}=0.96\% \qquad (10)$$

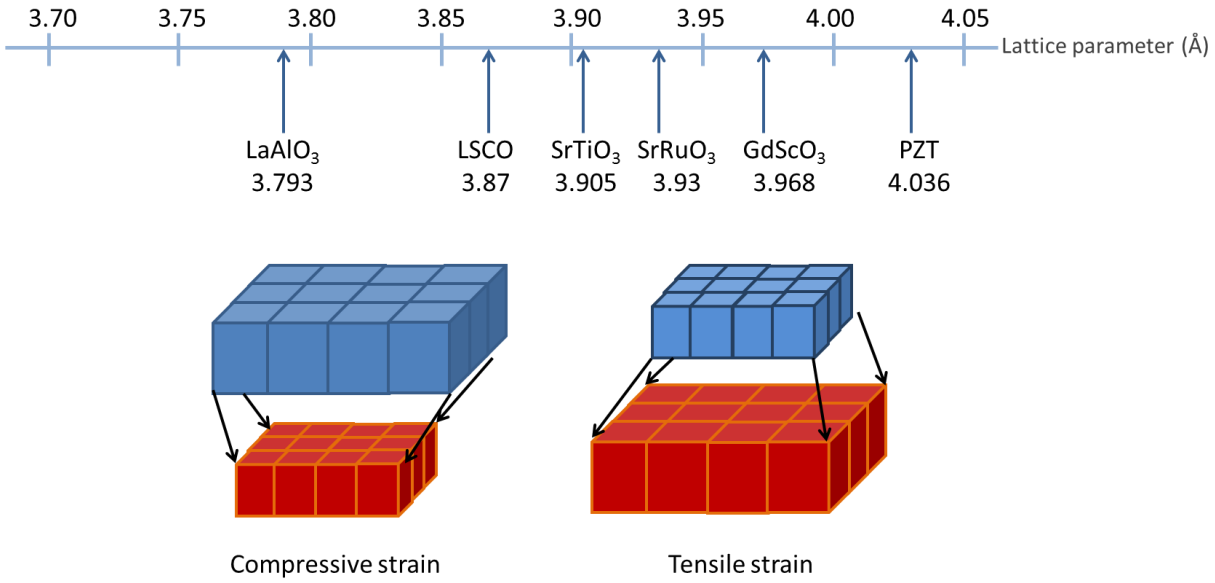

Figure 4.15. Lattice parameters in the bulk state for materials relevant to this work (top), with sketches of films grown in compression (left) or tension (right) when deposited epitaxially on substrates with smaller or larger lattice parameters, respectively.

To illustrate this theory, we can relate the strain with trench depth by creating a nine-island tic-tac toe shape with ranges of trench depths in 5 μm x 5 μm area in Figure 4.16. Each trench in different depths is realized by applying 9 V of set point with different milling time.

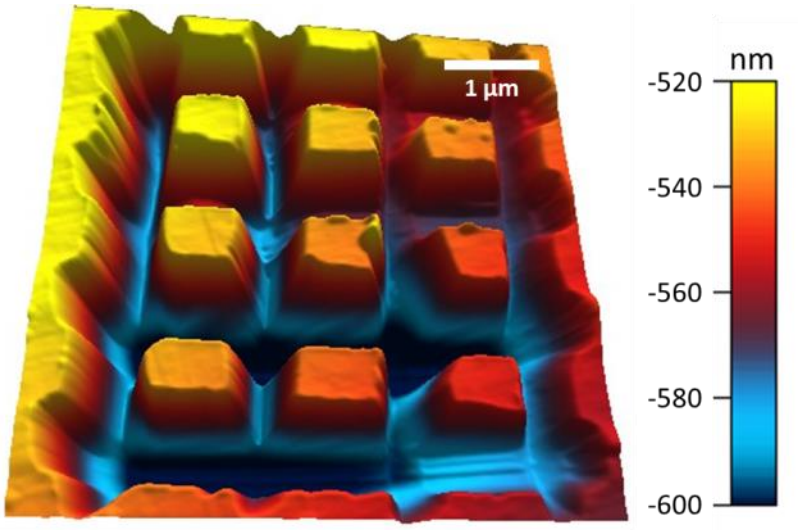

Figure 4.16. 3d topographic AFM image of 9 islands in PZT (90 nm) thin film after milling.

Therefore, nine isolated mesas with approximately the same size have been named from A to I according to the trench depth in Figure 4.17 (a). Figure (b) shows that mesa A has the smallest trench relief depth; B has medium relief depth, while mesa C has been relieved the most in the top row mesa. This is also true for mesa D, E, F as well as G, H and I. In addition, the mesas in the middle row D, E and F is slightly more relaxed than A, B and C respectively. Moreover, mesa G, H and I relieved more than D, E and F respectively. Upon applying external negative voltage on the nine mesas, we can monitor the out-of-plane switching for each mesa in Figure 4.17 (c). -1 Vdc was applied as an initial voltage in frame 4, some OP domain orientations has been reversed in mesa A at first place, no obvious switching event has occurred in other mesas. Mesa D began to switch in Frame 5; followed by mesa G with increasing voltage. Mesa with higher strain relief such as C, E tend to switch later time, followed by F and H. Mesa H is the last

one to complete switching as mesa I didn't switch possibly due to the trench depth is too deep that electrode layer has been removed around that area.

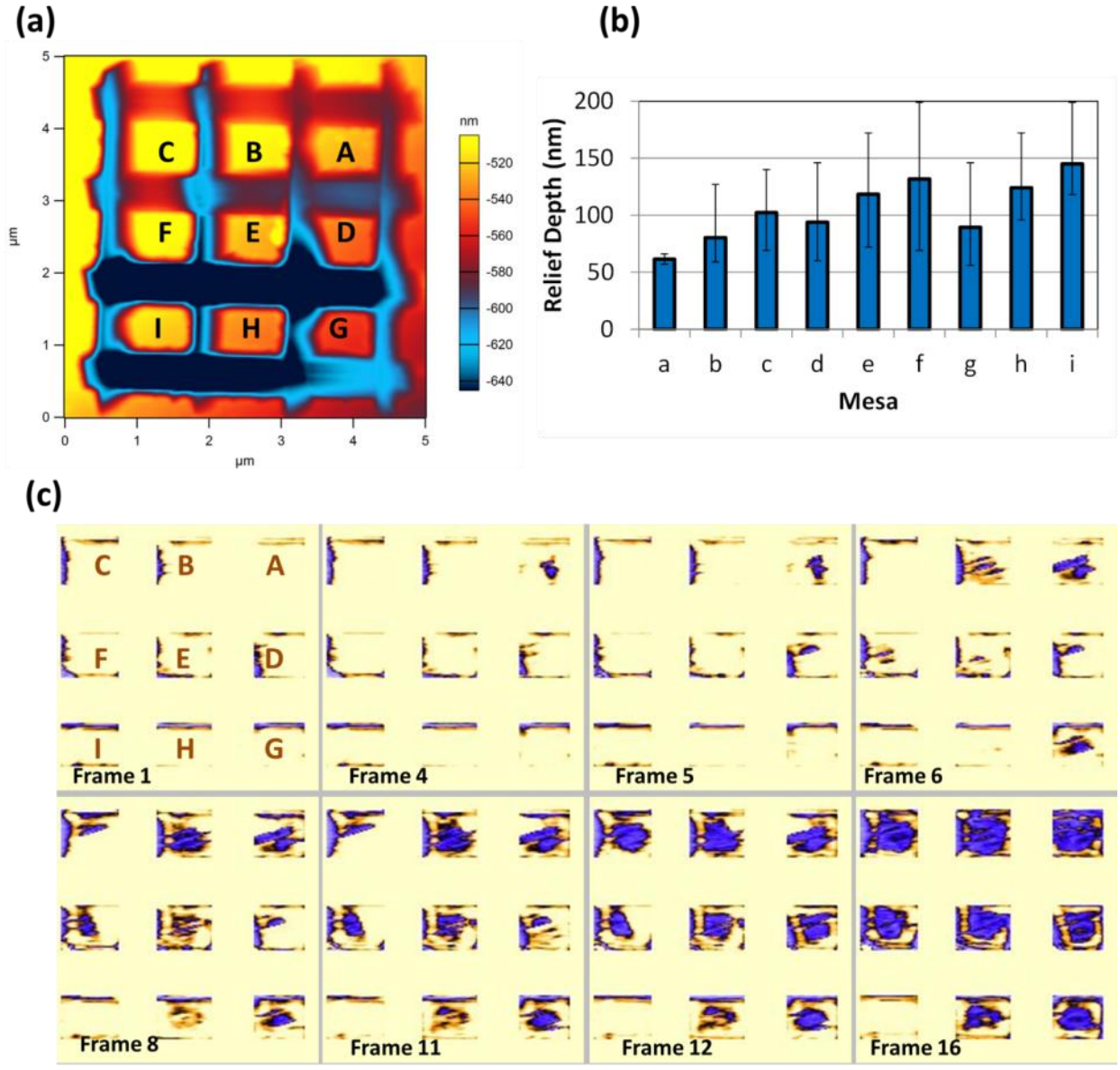

Figure 4.17. AFM height image for 9 mesas (a); trench relief depth for each mesa (b); switching progress for each mesa (c).

To analyze the switching behavior under different strain-relieving circumstances, the activation switching energy was calculated. Although it looks straightforward to determine the first frame to switch, a range of biases and switching durations is required to switch an entire region. In this

way, we consider that the poling energy of each single pixel can be proportional to the applied power*time. In PFM switching it is very complicated as the total energy during poling can integrate over all imaging conditions (DC, AC, linear ramp, or nonlinear ramp). Here we come up with the equations below:

$$P_{resistive} = IV = \frac{V^2}{R} \tag{11}$$

$$Energy = P * t_{applied} = \frac{V^2}{R} * t_{applied} \tag{12}$$

Non-linear bias/time conditions can thus be determined. By tracking the activation energy to switch the first domain pixel by pixel, a map of cumulative switching energy was shown in Figure 4.18 (a).

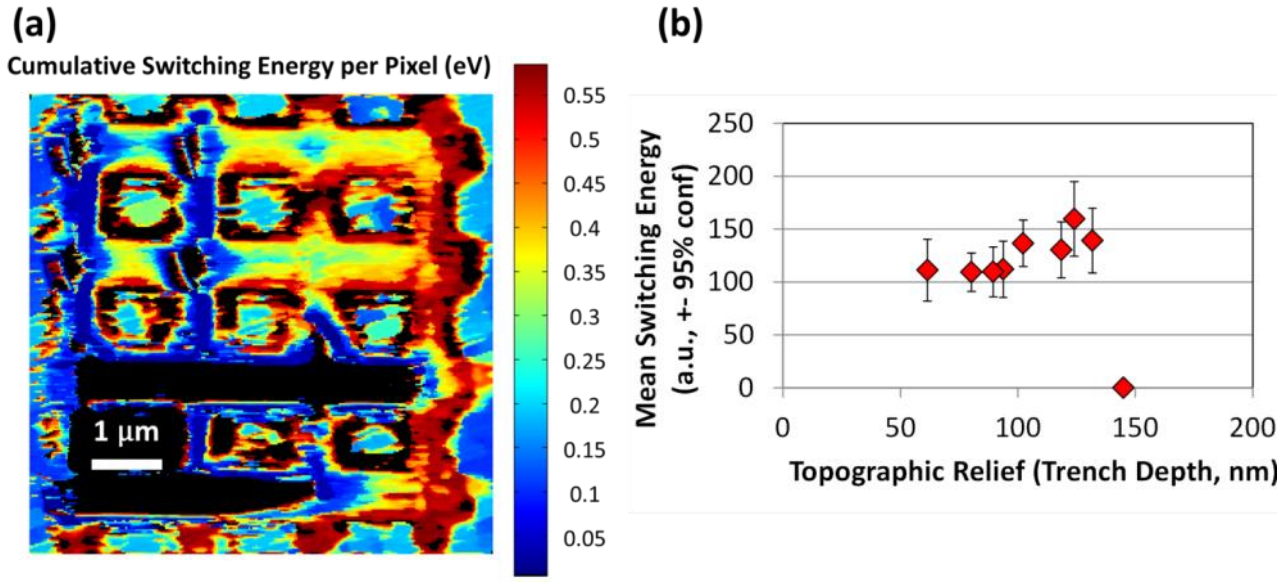

Figure 4.18. Switching energy required for each pixel (a); plot of the switching energy vs trench depth (b).

Notice that the trenches around some islands only need less than 0.05 eV to switch, as thinner layers tend to switch faster. For mesa A D and G, switching voltage of first domain ranges from

0.05 to 0.25 eV, the average energy required is ~0.15 eV. While for more strain relieved mesa B, C, and E, the switching energy varies from 0.2 to 0.35 eV. Mesa F and I require more than 0.4 eV to complete the switching process. Also continuous film at the edges of the image switches as low as ~0.15 eV. This fact may indicate that the more topographically relaxed of the mesa, the higher energy is required to switch. Figure 4.18 (b) presents mesas with ~125 nm topographic relief take ~ 30% more energy to switch than mesas with 50-80 nm relief. Thus, the switching energy depends on the strain relief.

4.7 Switching Dynamics after Nano-sculpting

To understand the mechanism, we can zoom in to one single mesa and carefully study the mesa switching dynamics shown in Figure 4.19. The amplitudes image at 0 Vdc represents domain configuration before switching; no a-domain creation has been observed during switching according to Figure 4.19 (a). Topography has not been changed either upon voltage applied in Figure 4.19 (b) confirming no apparent accumulation of surface damage. Therefore, we can assume that a-domain creation is not as preferred in the mesa structure comparing to continuous film. In principle, tensile strain has been relived around the mesa feature; new a-domain thusly cannot be formed due to the change of mechanical strain.

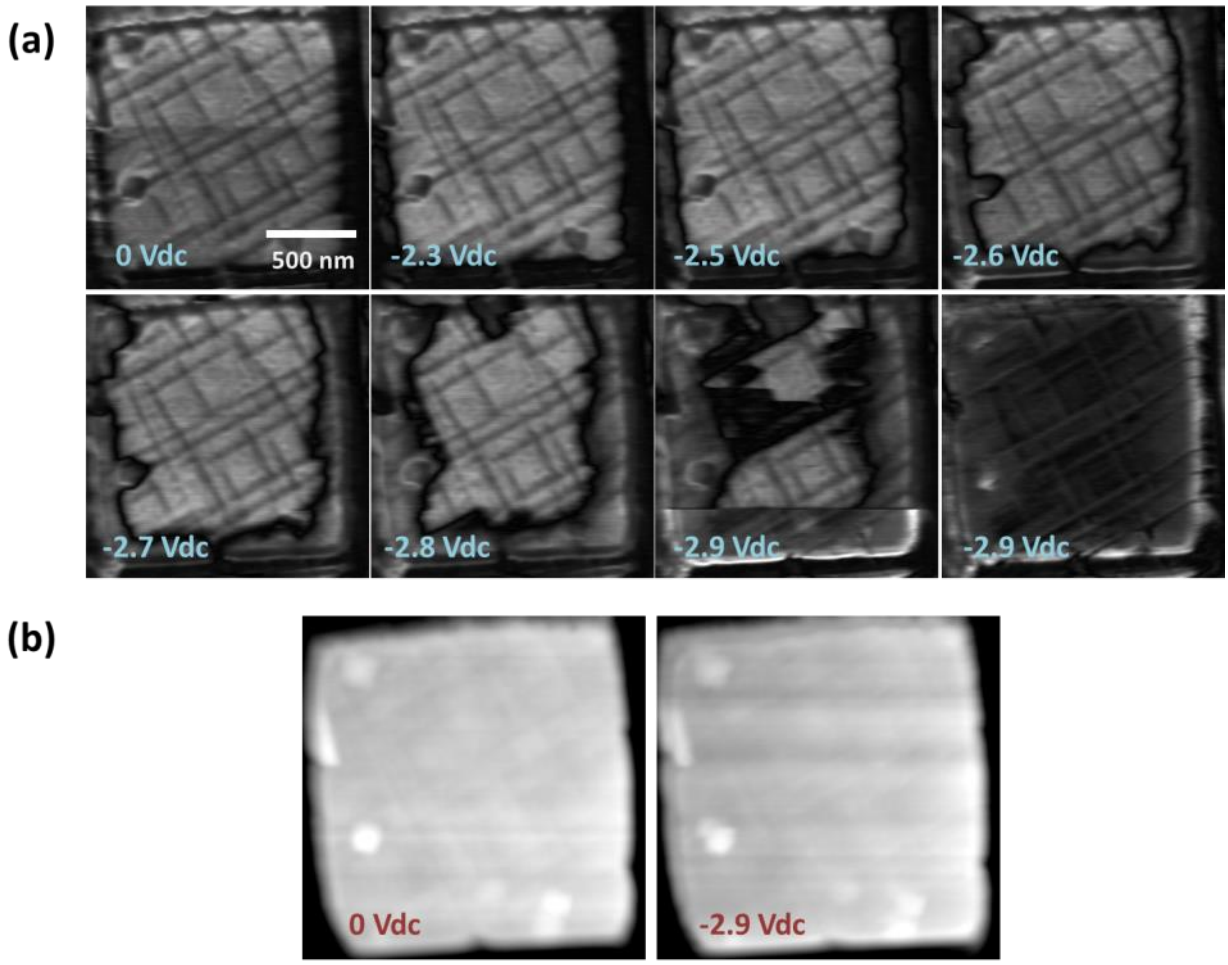

Figure 4.19. AFM amplitude images of mesa switching process under voltages (a); Topographic images before and after switching (b).

Hence, c-domain 180° degree switching in mesa structure was dominating during switching behavior. The increment in the electrostatic energy of the domain upon bias can be calculated as

$$-\int_0^{\vec{E}} \vec{P}\cdot \mathrm{d}\vec{E} \approx -\vec{P}\cdot\vec{E}\,, \qquad (13)$$

where $\vec{P}$ is the polarization and $\vec{E}$ is the electric filed[73]. Consequently, the energy barrier for the c-domain switching from as-grown state to the opposite polarized orientation along c-axis is :

$$\Delta U_c = -P_c \cdot V/d. \qquad (14)$$

For different mesa structures above, the relaxation behavior is different as we designed. The mesa with higher trench depth would be more relaxed and experience higher polarization in c-direction as discussed earlier. According to the equation ΔU_c above, switching energy barrier height for c-domain is proportional to the value of polarization. We can conclude that higher switching energy is required for more relaxed mesa.

Via nano-sculpting technique, we can microfabricate fine sizes of mesas with ranges of topographic strain relief. By controlling the switching energy, each individual island can be switched accordingly. This interesting phenomenon sheds light on the future ferroelectric devices in realizing ferroelectric reading and writing with electrical-control.

4.8 PZT Mesa without a-domains

It is also critical to investigate the PZT thin films without 90° a-domain which is in different strain state. We studied the 30 nm PZT thin film grown on $SrRuO_3$ electrode and buffered on $SrTiO_3$ substrate with the same technique, and several mesas have been made with different sizes and different depth. The a lattice parameter for $SrRuO_3$ is 3.93 Å and $SrTiO_3$ is 3.905 Å, while PZT is 4.036 Å shown in Figure 4.15. Thus the first layers of PZT are deposited on a strained SRO layer[79].

By calculating the total elastic strain, it's compressive strain for the PZT/$SrRuO_3$/$SrTiO_3$ heterostructure system with thicknesses less than 70 nm[88]. This PZT film with relative larger tetragonality compared to bulk value shows a fully polar-axis-oriented domain structure shown in Figure 4.20 [89].

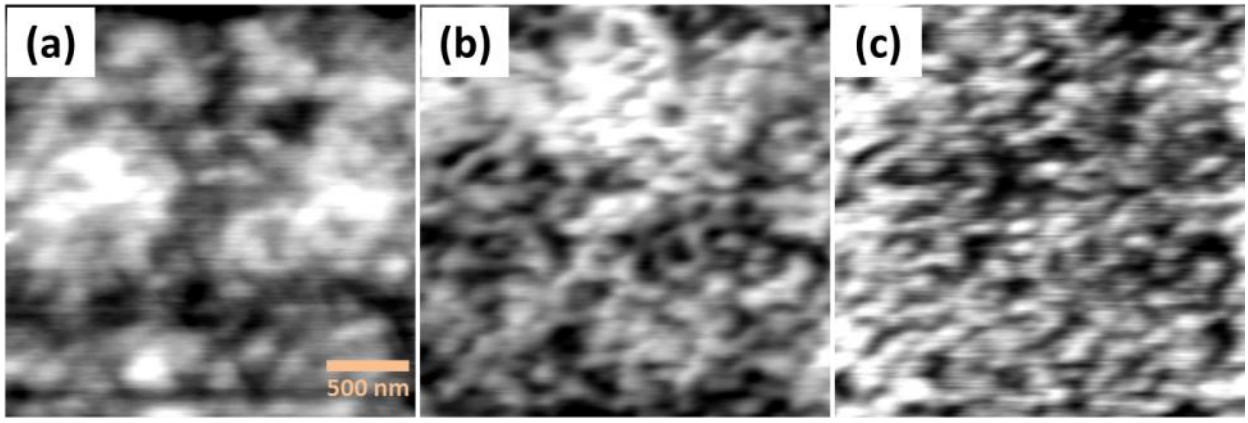

Figure 4.20. Topographic image of PZT/SRO/STO thin film in 3 µm x 3µm size (a); OP amplitude signal (b); OP phase signal (c).

The nanosculpting technique has been applied to fabricate four mesas with different trench depth in Figure 4.21. Four mesas have similar same sizes ~1 μm^2, top two trenches are ~60 nm in depth, the bottom trench is ~90 nm; two left trenches are ~30 nm while the very right trench is as deep as 60 nm. At original state before milling process, the PZT thin film is highly strained in compression. Thus, the c-lattice parameter has been increased due to the tensile strain in z axis. By eliminating the surrounding materials of the mesas, the film has been unclamped and retains relaxation. Thus the ferroelectric properties can be refined as well.

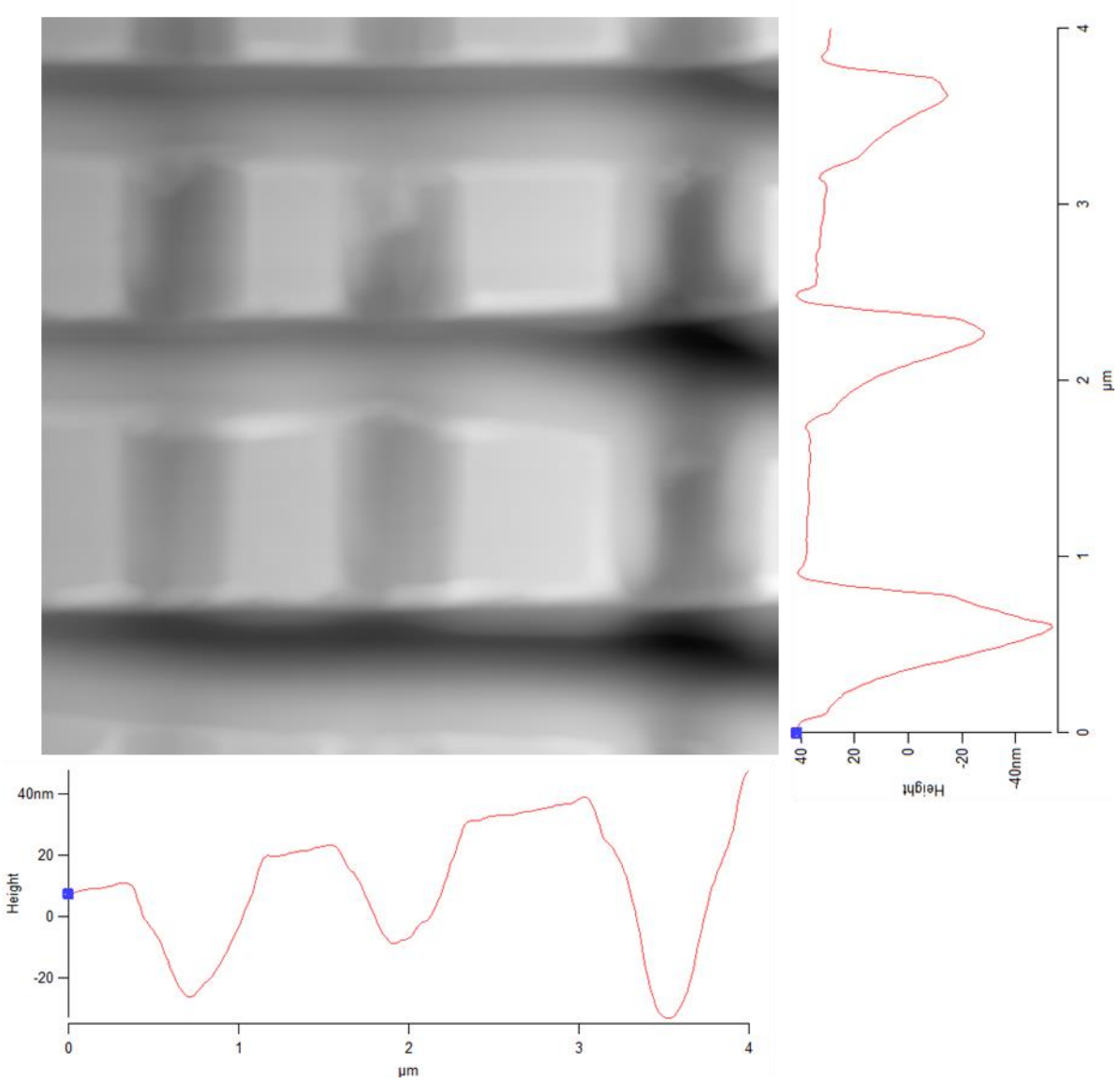

Figure 4.21. AFM topographic image of the 4 mesas with milling trenches around. Top right and bottom histogram are cross sections for the corresponding trenches.

Via applying external voltage to the four mesas, we can study the domain switching behavior of the mesas displayed in Figure 4.22. Domains on each mesa all show a strip shape at initial state with -0.6 Vdc and 3Vpp AC bias, domain growth is dominated during the switching process. As the voltage increased up to -1.3 Vdc, the switching process has been completed as all domains are oriented at the same direction [001] or [00-1].

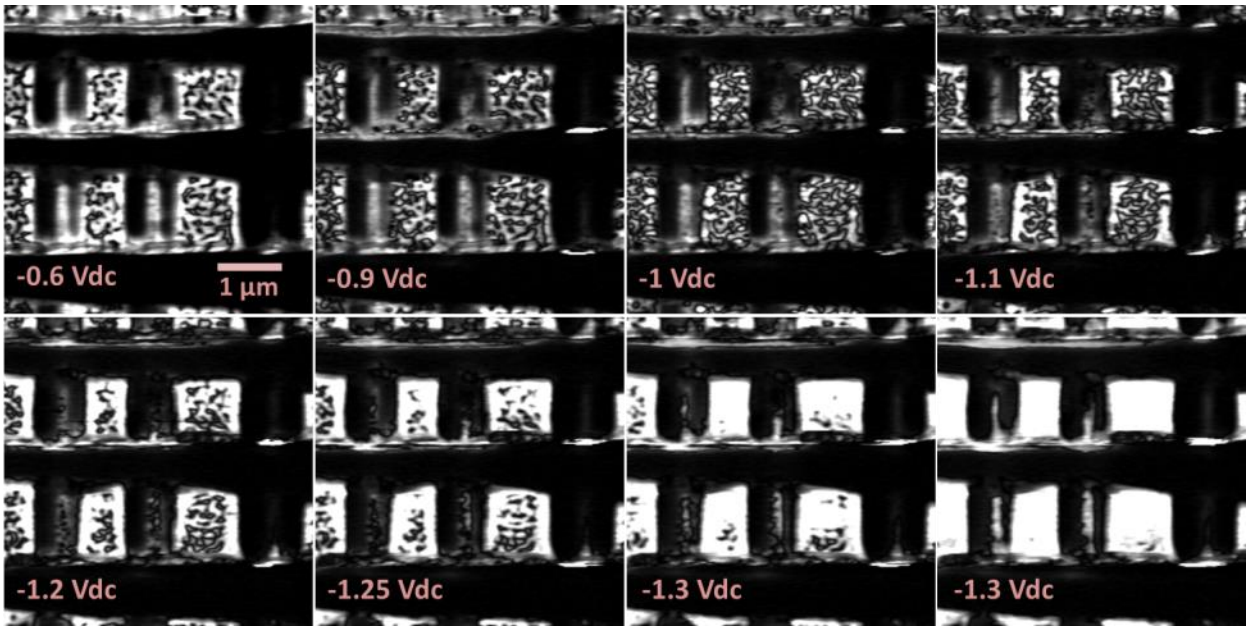

Figure 4.22. PFM amplitude images upon increasing voltage magnitude for 4 partially strain-relieved mesas.

By tracking ferroelectric domain switching pixel by pixel, Figure 4.23 depicts a map of the switching orders for all 4 mesas. It shows the switching progress as the edges of mesas take only 5-10 frames to switch while centered regions need to wait 15~20 frames to observe the occurrence of the first domain change. This phenomenon is crucial as the edges of mesas are mostly relaxed with c close to the bulk value. Therefore, we propose that in addition to enhancements in piezoelectric properties at strain-relieved feature edges, the coercive field can also be related engineered to the relaxation condition.

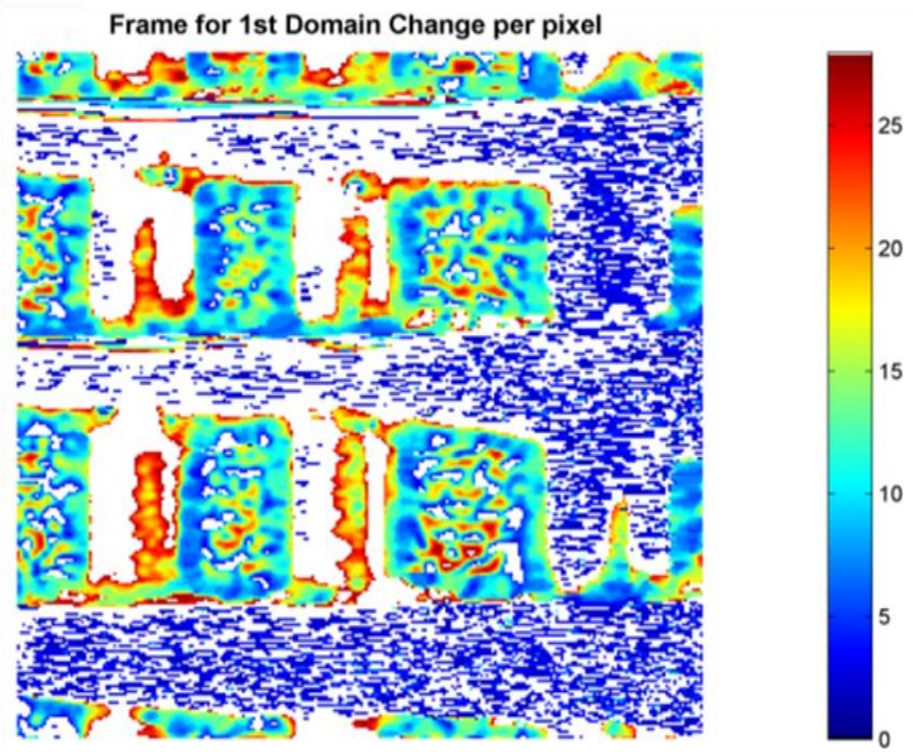

Figure 4.23. Number of frames for the first domain change per pixel (b).

The cumulative switching energy has also been considered in Figure 4.24 (b), demonstrating that the activation energy for mesas with topographic relief in this no a-domain PZT film. The average switching energy at the edges for each mesa is ~ 0.06 ev while the centered area requires ~0.14 ev to switch. Again, it proves the edges require less energy to switch possibly due to higher density of nucleation and minimal damage during the milling progress.

More studies needed to investigate the properties of switching dynamics of nano PZT mesas with no a-domain such as dislocation investigated by TEM. More information will be discussed in the Future Work Chapter.

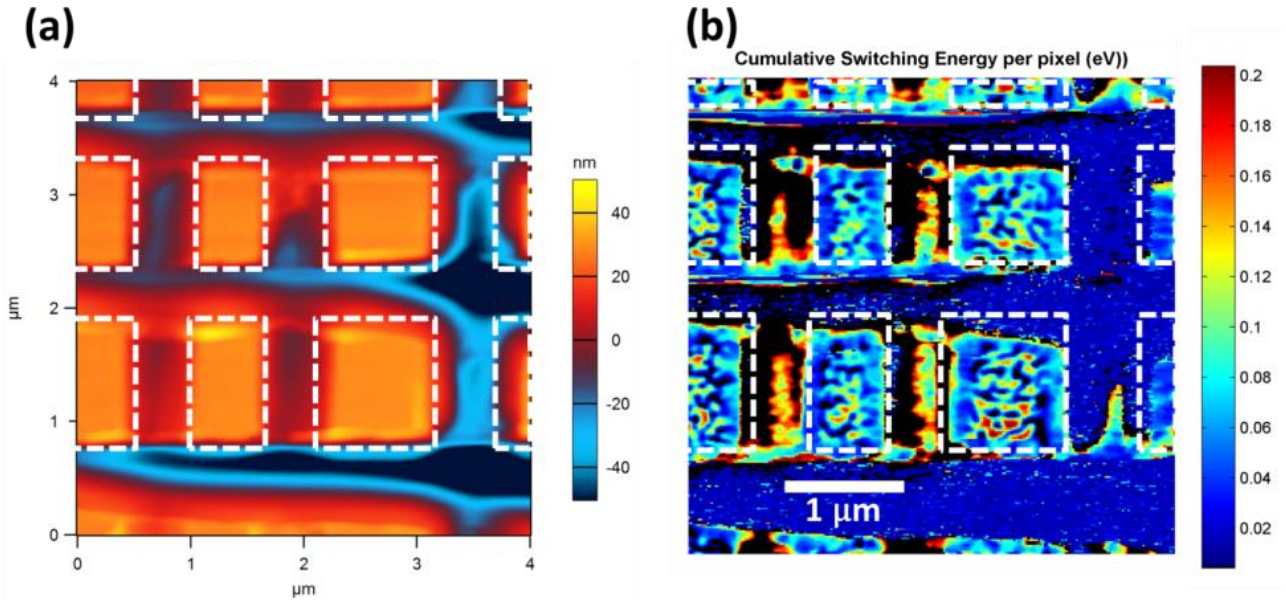

Figure 4.24. AFM topographic image of 4 mesas (a), switching energy barrier needed for each pixel in all mesas (b).

4.9 Summary

We present a unique technique to pattern ferroeletric sample with less damage compared with Focused Ion Beam method: Nano-Sculpting. This approach to fabricate micro-structured PZT mesa does not introduce remarkable change to topography or as-grown a-domain configurations. No disturbance of ferroelectric domain switching process has been detected. Via Nano-Sculpting, in-plane tensile strain has been partially relieved leading to an enhancement in the ferroelectric polarization.

In addition, we have shown the switching dynamics for several different domain structures. More strain-relieved mesas with enhanced piezoelectric properties exhibit a higher activation switching energy than the more highly clamped adjacent continuous film. Our study of ferroelectric and ferroelastic switching in variously microstructured strained PZT thereby allows novel investigations into their enhanced ferroelectric properties and the switching behavior of nanodomains.

Chapter 5 Geometrically Strain-Relieved PMN-PT thin films

5.1 PMN-PT Normal Enhancement

Lateral subdivision of piezoelectric thin films improves functional properties such as piezoelectric constant and dielectric response through declamping of the substrate –film stress[87, 90]. This chapter presents the measurement of d_{33} along patterned PMN-PT with various strip structures via two characterization methods. Piezoresponse force microscopy indicates the local piezoelectric strain; while X-ray diffraction shows the intrinsic piezoelectric property. These results shed light on the functionality due to declamping in piezoelectric materials.

Piezoelectric response with high resolution was realized by Piezo Force Microscope (PFM). The patterned structures were imaged in contact mode with applied forces of approximately 286 nN. The conductive diamond probe (CDT-FMR) was grounded while the bottom electrode was biased for piezoactuation at small voltage. In order to minimize error signal, the acquired signal was calibrated by a quartz crystal with a known d_{33} coefficient of 700 pm/V, indicating a calibration factor of ~ 5x to the detected response.

In this measurement, we carefully studied the PMN-PT arms with width of 2 μm, 1 μm and 0.75 μm which are the narrowest and may exhibit the strongest strain relief. Before the measurement, a poling prodcedure of +5 Volts (DC) for 15 minutes and 40 minutes of room temperature aging was performed to prevent back switching. During scanning, a DC bias was applied to the bottom electrode with AC signal of 0.8 $V_{peak\text{-}to\text{-}peak}$ at resonant frequency of ~500 kHz. To characterize d_{33}, the piezoelectric strain was achieved via DC offsets ranging from 0.4 to 1.5V. Leveraging

multi-parametric concepts reported previously[91], the DC bias was increased by 100 mV and PFM signal recorded by consecutive image frames of the same area. There was spatial drift during scanning which was less than 35 nm in overall images which was corrected afterwards by shifting to align topographic features.

Obtained data for all 3 mesas was demonstrated here in Figure 5.1, topography (top row) as well as piezo response image at selected DC bias conditions (bottom rows). The PFM response relies on the external voltage with clearly resolved individual grains. We also notice that the signal has been enhanced as AFM tip fall off the sidewalls causing by the changes of the contact area.

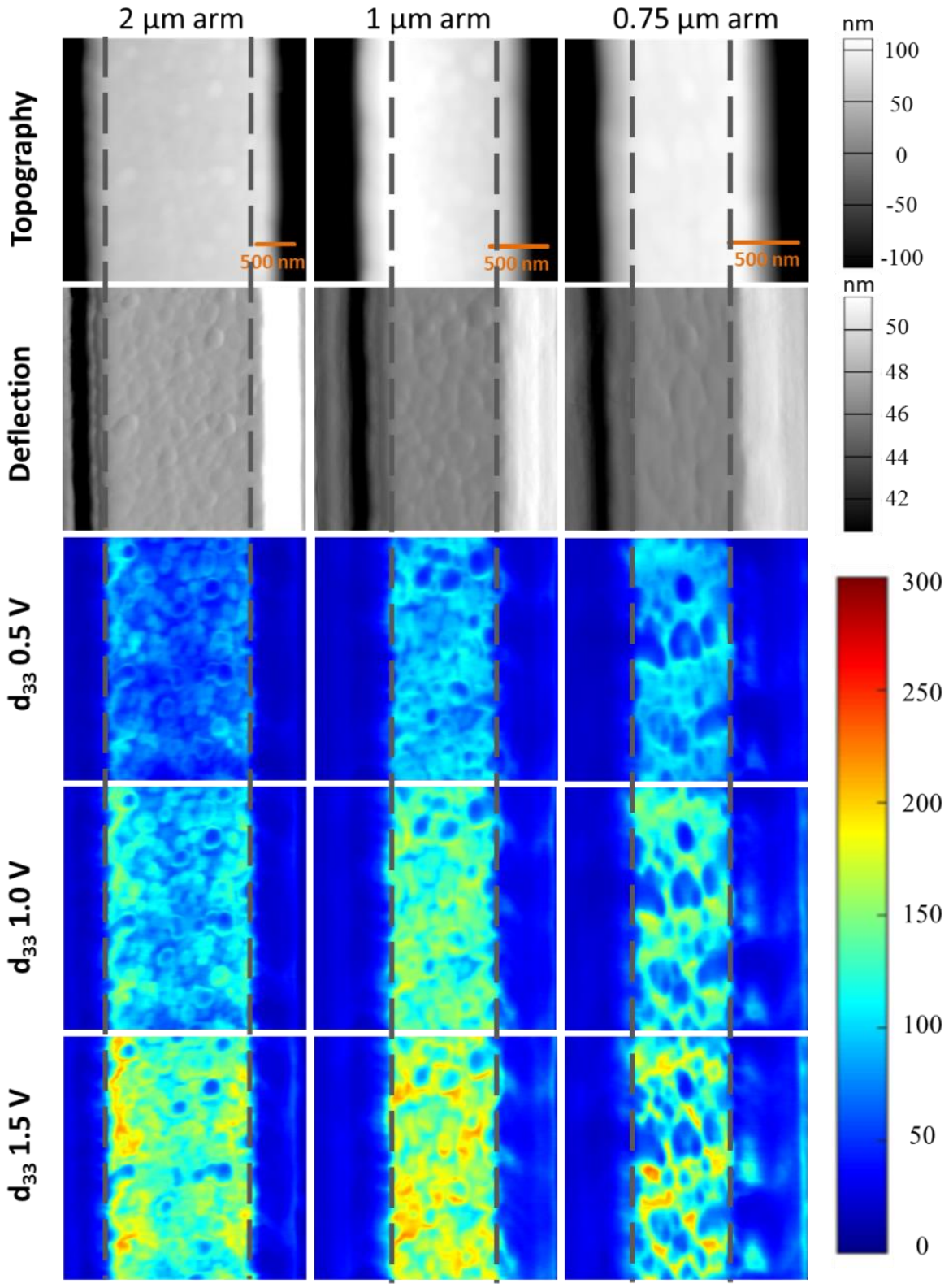

Figure 5.1. Topography, deflection and piezoresponse (amplitude) maps, with DC biasing of 0.5, 1.0, and 1.5 V.

The intrinsic d_{33} coefficients can be calculated pixel by pixel via extrapolating the achieved d_{33} signal at corresponding DC offset back to 0 V. This approach is to prevent the possibility of back-poling of actual 0 DC measurements. As the voltage is increased from +0.4V to +1.5V, the piezo response is linear with a fitting parameter of 0.99, along with the calculation of the standard deviation of error. Figure 5.2 depicts the results of extracted d_{33} with resolved d_{33} coefficient for the 3 mesas in the top row and standard deviation error for d_{33} displayed in the bottom. All maps reveal the arm geometry dependence of piezoelectric coefficient pixel with ~256 x 256 pixel resolutions at the same color contrast.

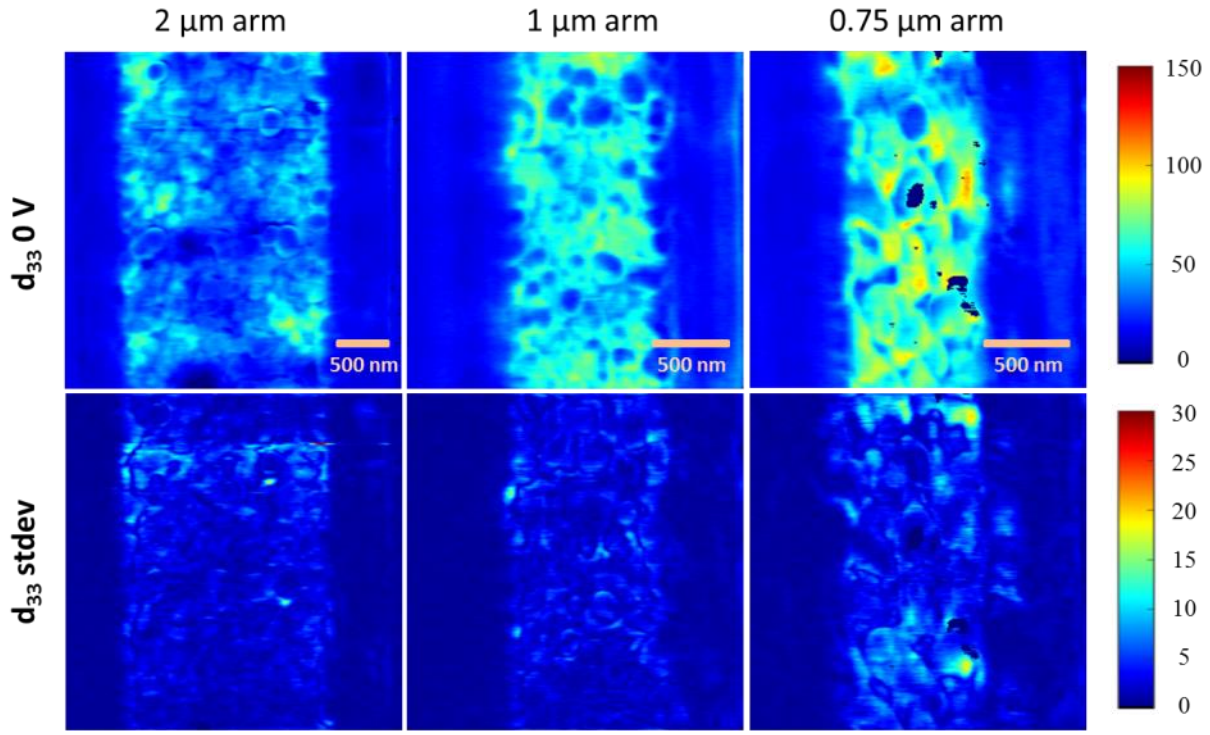

Figure 5.2. Maps of the calculated d_{33} coefficients at 0 bias (top row), and the negligible standard deviation of error for d_{33} (base, displayed with a 5x enhancement in the contrast scale), for microfabricated 2 um, 1 um, and 0.75 um arms.

The spatial map in Figure 5.2 is suggesting that regions with strain-relieved piezoactuation enhancements would likely have finer grains, a higher degree of texture, or even epitaxy for greater spatial uniformity. Accordingly, the mean, and the peak (optimized), d_{33} coefficients

determined along the y axis of the images in Figure 5.2 are displayed in Figure 5.3 for all three microstructured arms.

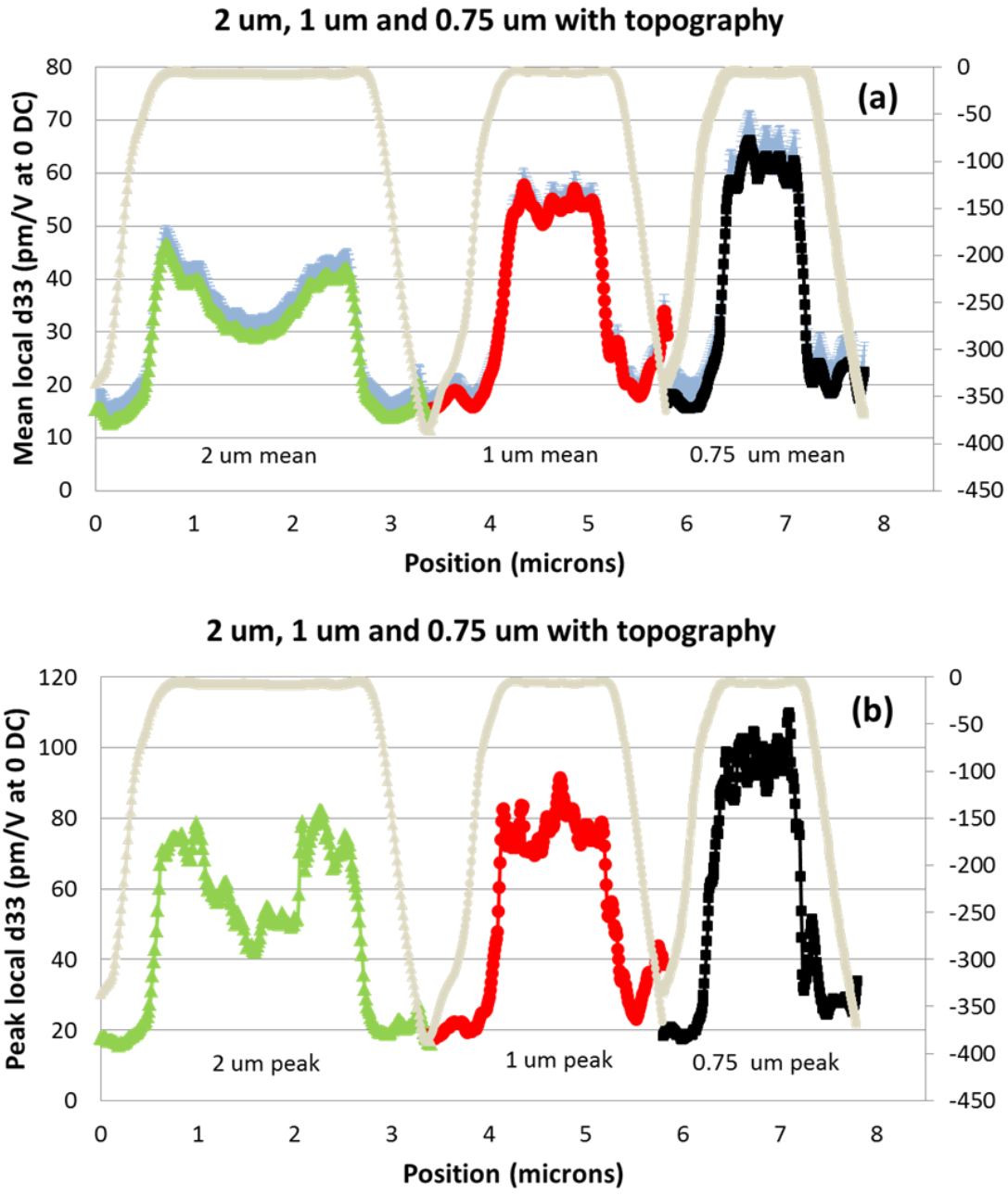

Figure 5.3. Intrinsic d_{33} coefficients across 3 microfabricated feature dimensions (left axes), overlapped with topography (right axes), for the (a) mean value with standard deviation error bars superimposed, and (b) for the peak values (not greater d_{33} scale).

For the 2 μm arm structure, the PMN-PT film exhibits an intrinsic d_{33} coefficient of ~40 pm/V in the center and 80 pm/V peak value near the sidewalls. This enhancement of d_{33} at the edges supports the hypothesis that the sidewalls of the 2 μm arm are declamped, relieving substrate-induced strain[92], as compared to the still-clamped center of the 2 μm or larger arms. This extends spatially over a range of approximately 600 nm, suggesting that arms narrower than 1.2 μm should benefit from at least partial declamping throughout. This is confirmed by laterally uniform mean and peak d_{33} values across the 1 μm and especially 0.75 μm arm structures. Their average peak d_{33} coefficients are approximately 80 pm/V and 90 pm/V, respectively. Qualitatively, these results are equivalent to beam line diffraction data on identical specimens[93]. Ongoing work aims to identify if still smaller features will exhibit further enhanced d_{33} coefficients, and whether such declamping will influence domain polarization dynamics and stability[34].

5.2 Frequency Dependence

As d_{33} mapping involves the contact resonance tracking to achieve precise results, the signal can vary with texture, contact area between tip and sample, contact force, and other parameters[94, 95]. To measure the d_{33}, the contact resonance remains unchanged during scanning to perform a rather simple measurement at single frequency which can drive the piezo response reasonably as described earlier. To inspect the relation between PFM response and resonant frequency, an example of consecutive images acquired with the same AC bias and sequentially incremented frequencies is displayed in Figure 5.4.

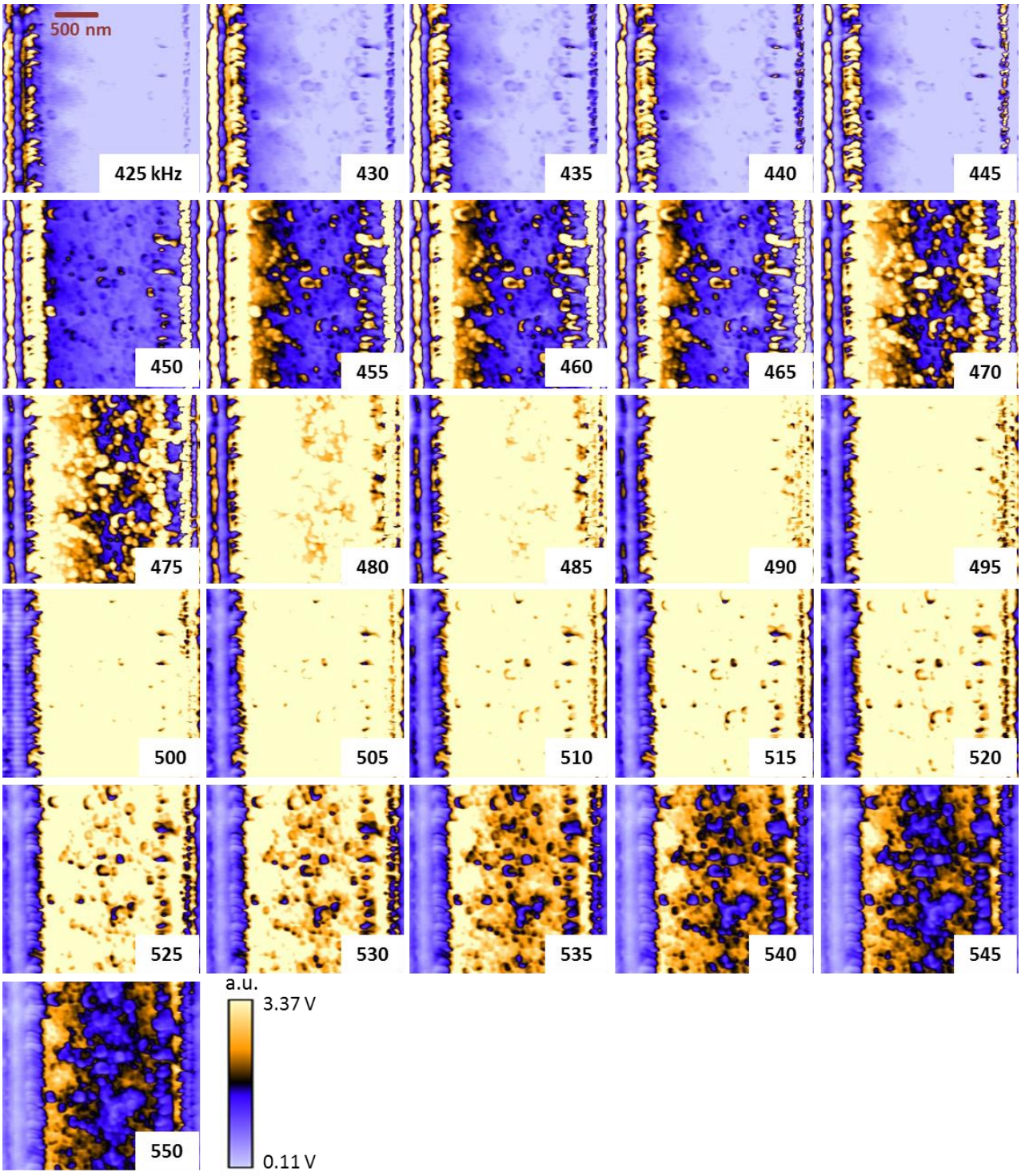

Figure 5.4. Montage of 26 piezoresponse amplitude images acquired with distinct excitation conditions.

By tracking the amplitude response pixel by pixel, as was analyzed with Figure 5.2, the maximum amplitude as well as the corresponding contact resonance frequency can be resolved in Figure 5.5. As shown, the response is uniform in general, with a few exceptions of individual grains. In addition, the signal is affected when the tip 'falls off' of the sidewalls of the microfabricated structures. Of course these areas are clearly distinguished in the topography, and the frequency response. Thus, it is generally sufficient, and extremely convenient, to employ single-frequency imaging for measurements such as in Figures 5.1-5.3. This approach also offers the great advantage that all 3 features can be investigated in one imaging session allowing a more precise direct comparison of their independent results.

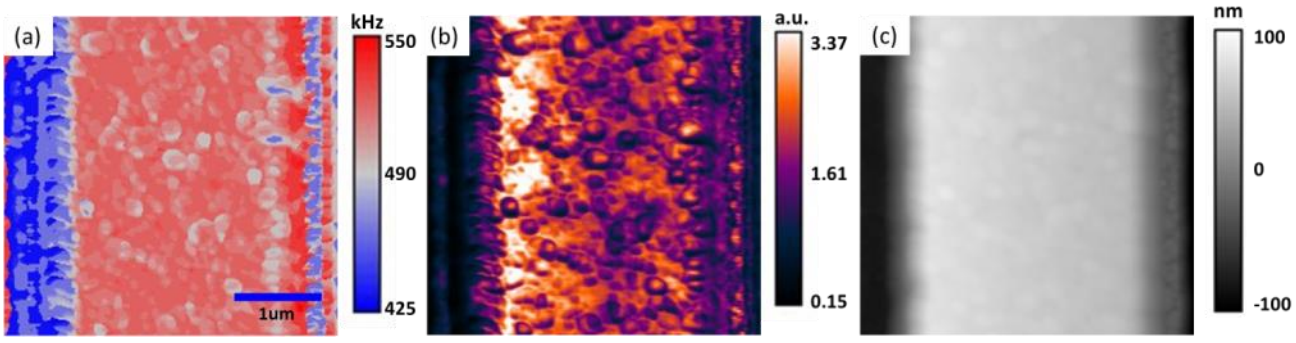

Figure 5.5. Calculated contact resonance frequency (a), peak piezoresponse magnitude (b) and topography image (c).

5.3 XRD

The local piezoelectric coefficient of patterned features was also explored by X-ray diffraction on mesas ranging from 9 µm to 0.75 µm by R. Keech from Pennsylvania State University. d_{33} can be calculated from the linear fit of strain in d-spacing of the PMN-PT peak position as a function of electric field at each position on an arm. Figure 5.6 shows the field-induced shifts in {002 d-spacing (a) as well as the calculated intrinsic d_{33} (b). The lattice parameter in z axis near the edges is increased compared to the center region, indicating the relief of strain imposed by

the substrate, as reported by Bühlmann *et al*[96]. Furthermore, the high field intrinsic d_{33} was extracted from the fitting of strain vs. field along the position.

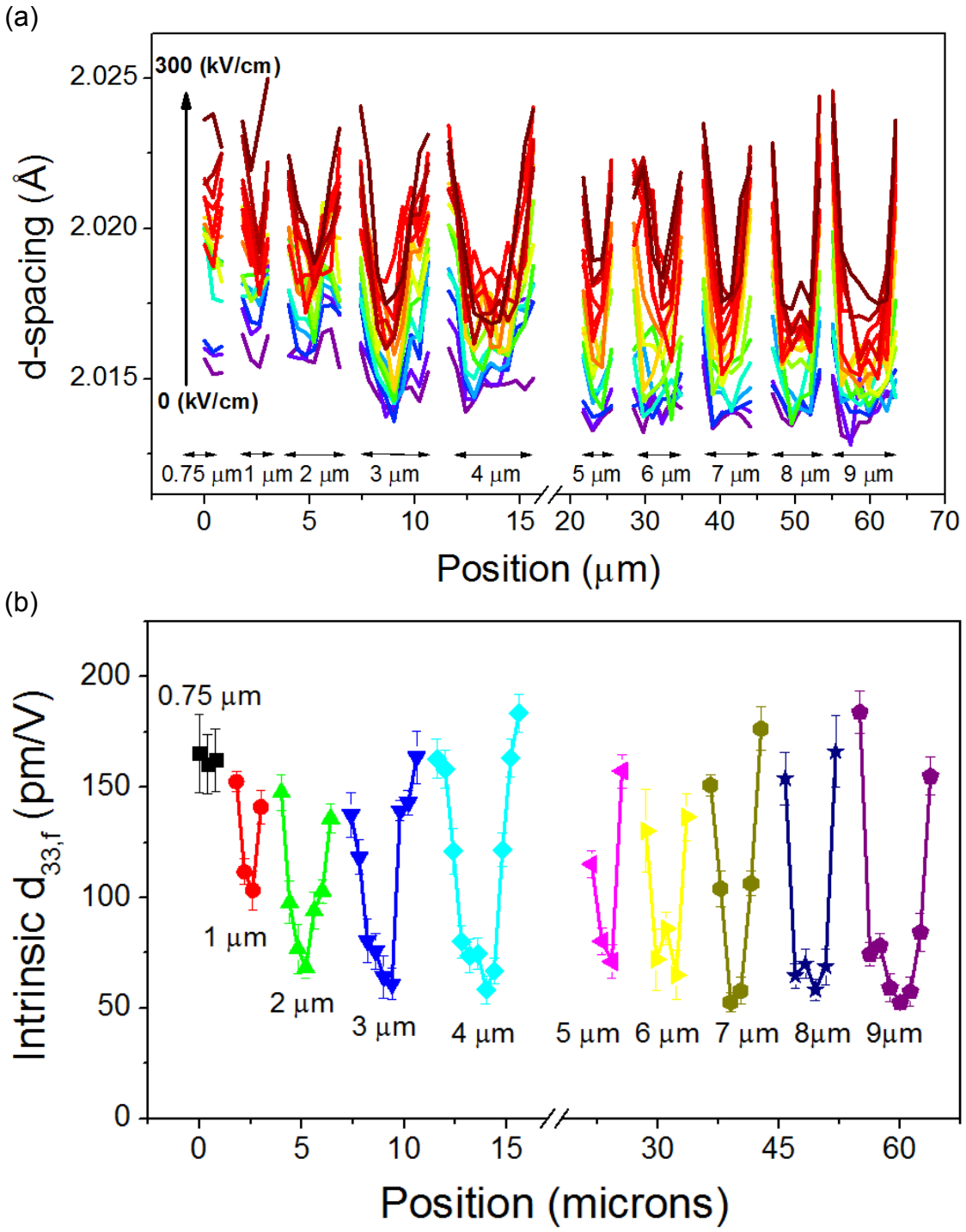

Figure 5.6. PMN-PT d-spacing under increasing DC voltage as a function of position (a); the intrinsic d_{33} coefficient as a function of position was calculated and shown in (b).

The piezoelectric response of PMN-PT film was declamped by using ion etching to form mesas. d_{33} was characterized by piezoresponse force microscopy and nanoprobe X-ray diffraction as a function of position. The piezoelectric coefficient was enhanced ~ 3 times at sidewall compared with clamped value. The edges enabled declamping width of 500-600 nm into the arm feature, thus arm structures with lateral dimension less than 1 μm would experience an entire enhancement along the arm. Observed enhancement in d_{33} via PFM was in strong agreement with data acquired from X-ray.

5.4 PMN-PT In-Plane Enhancement

5.4.1 IP Signal of 2 μm arm

For the PMN-PT antennae structures, we can also measure In-Plane signals of the 2 μm arm structure to determine the lateral relaxation behavior. We recorded lateral signal at different alignment shown in Figure 5.7 by mounting the tip parallel to the antennae structures. A 1.4V AC peak to peak bias is applied at 965 kHz. Also, 0.8V of DC bias are superimposed to prevent ferroeletric back-switching of the PMN-PT film.

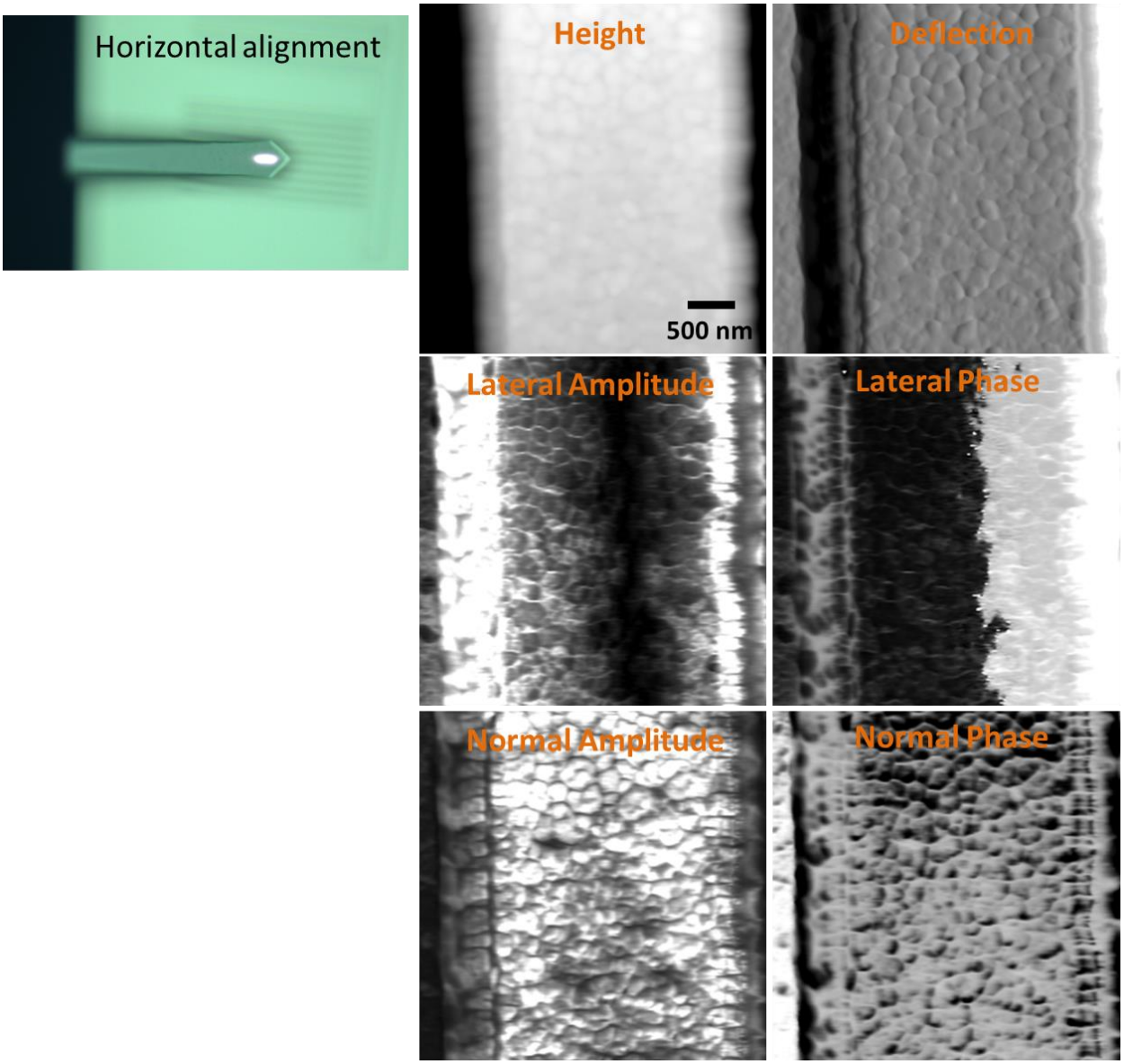

Figure 5.7. Height, deflection, Amplitude and Phase images of Normal and Lateral signals with the probe aligned parallel to the arm structures.

The Normal signal represents d_{33} coefficient of PMN-PT materials along c-axis; while the lateral signal indicates the property of d_{15} transverse piezo constant. The lateral amplitude shows enhancement on both edges of the 2 μm structure and a minimum value around the center area. By combining the lateral phase image with black and white color contrast, we know that left and right side of the 2 μm feature have the opposite In-Plane orientations. To assure this, same

signals were recorded by rotating the sample to 90° and aligning the probe perpendicular to the sample shown in Figure 5.8. At this tip-sample configuration, lateral signal reveals the homogeneous orientation with evenly distributed nanodomains in the lateral amplitude image.

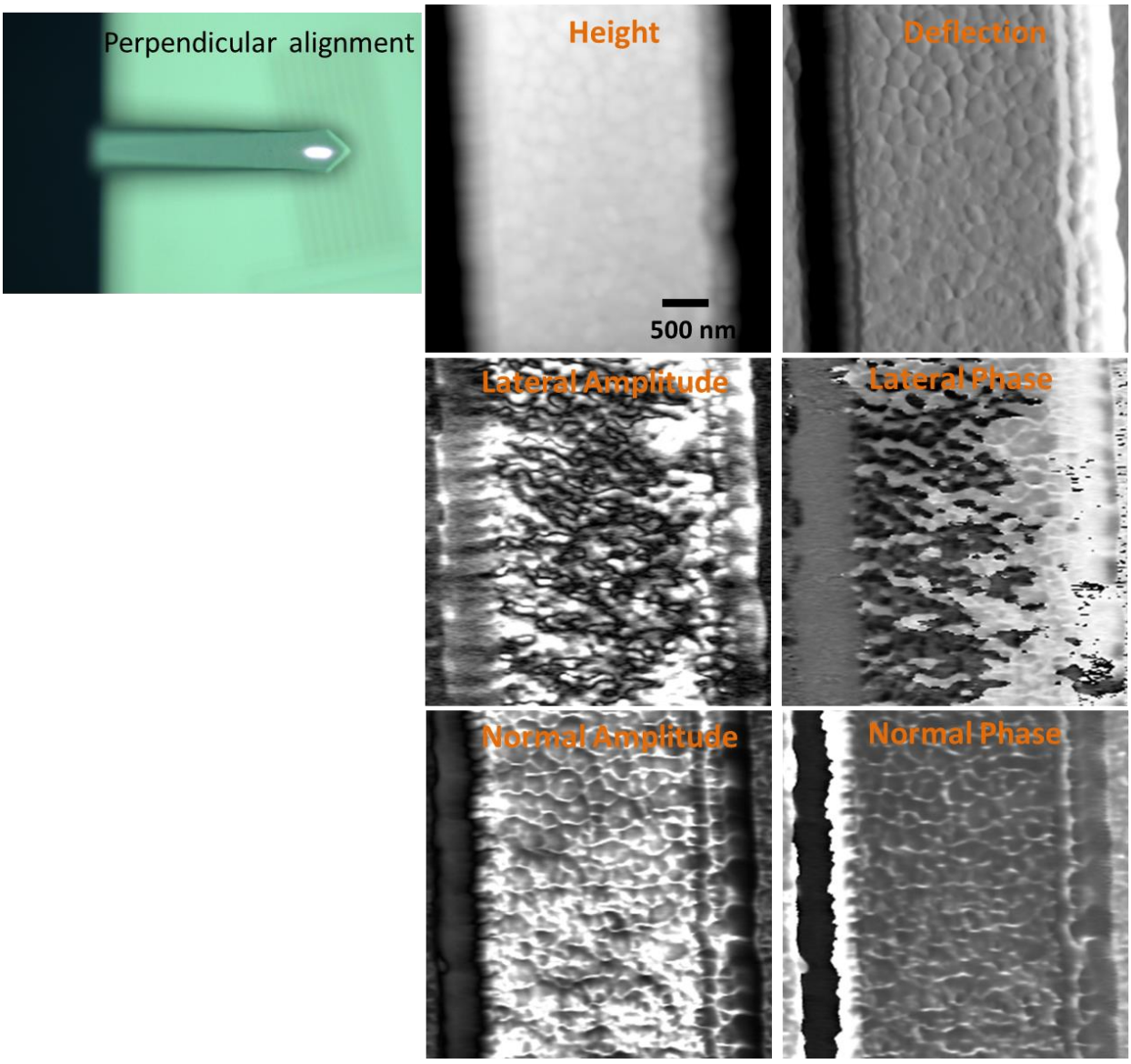

Figure 5.8. Height, deflection, Amplitude and Phase images of Normal and Lateral signals when the probe aligned perpendicular to the arm structures.

To confirm the lateral signal is not induced by the cantilever torsion when climbing the edges of the arm structure, we also imaged the signal when aligning the cantilever and 2 μm arm at 45° as

shown in Figure 5.9. The In-Plane phase signal still demonstrates a black and white (full phase shift) in-plane orientation change, while the amplitude signal clearly reveals that this occurs in the center of the structure. This similar response to Figure 5.7, but here with a geometrically asymmetric experimental configuration, confirms that these results are not an experimental artifact.

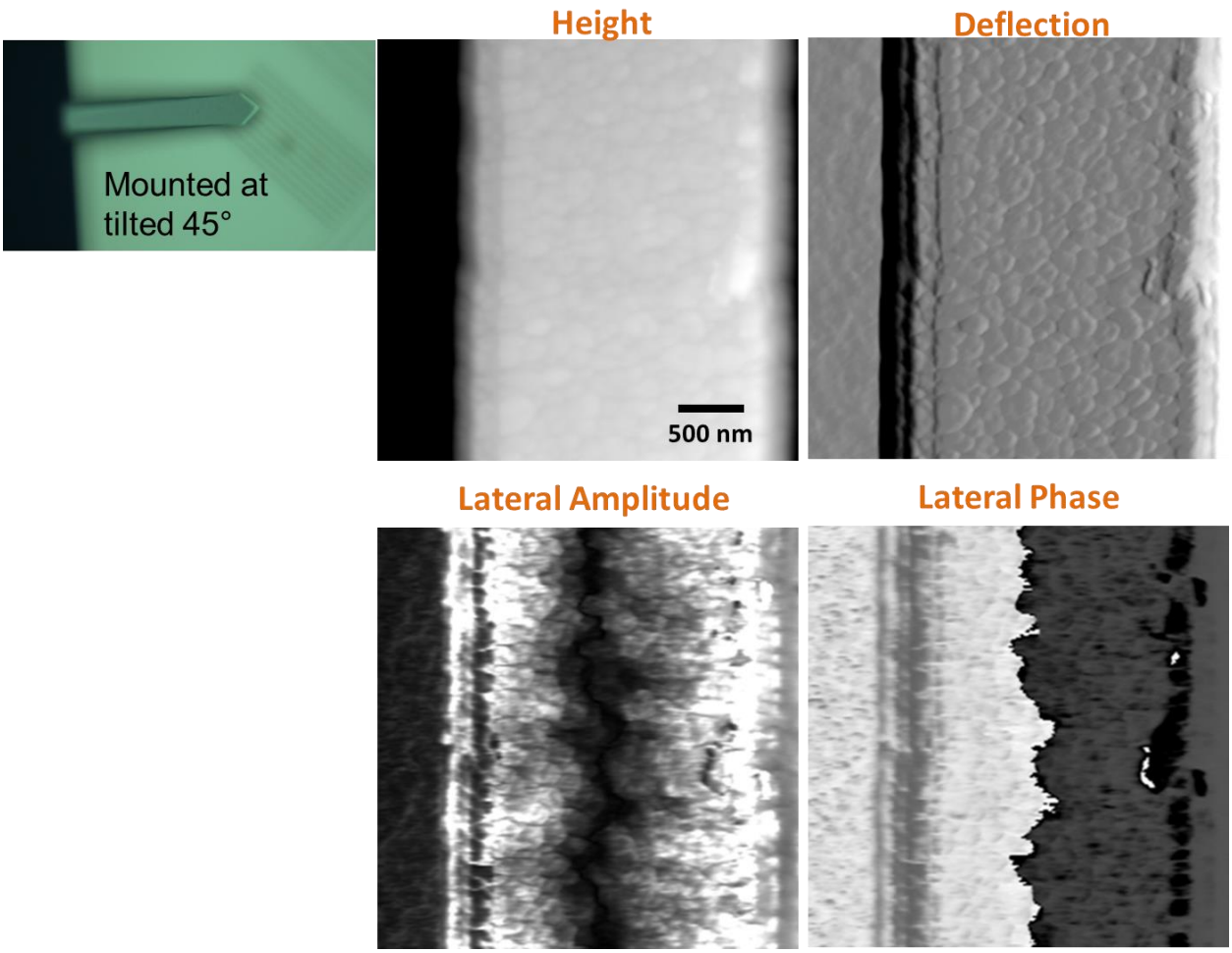

Figure 5.9. Height, deflection, Amplitude and Phase images of Lateral signals when the probe aligned 45° to the arm structures.

More information thus can be extracted by analyzing these signals pixel by pixel using MatLab code. Figure 5.10 displays the map of Out-of-Plane signal (Normal) with enhancement along edges of the feature in figure (b) as well as the In-Plane (Lateral) signal in (c) and (d). Figure (a)

depicts a sketch of In-Plane domains orientations with 2 color contrast and cross section of topography in Z axis. When the probed aligned along the arm features, 90° signal along x axis was captured with either white or black phase contrast along x vector indicating left or right: pink (180°), or blue (0°) orientations; 0° signal along y axis with no signal.

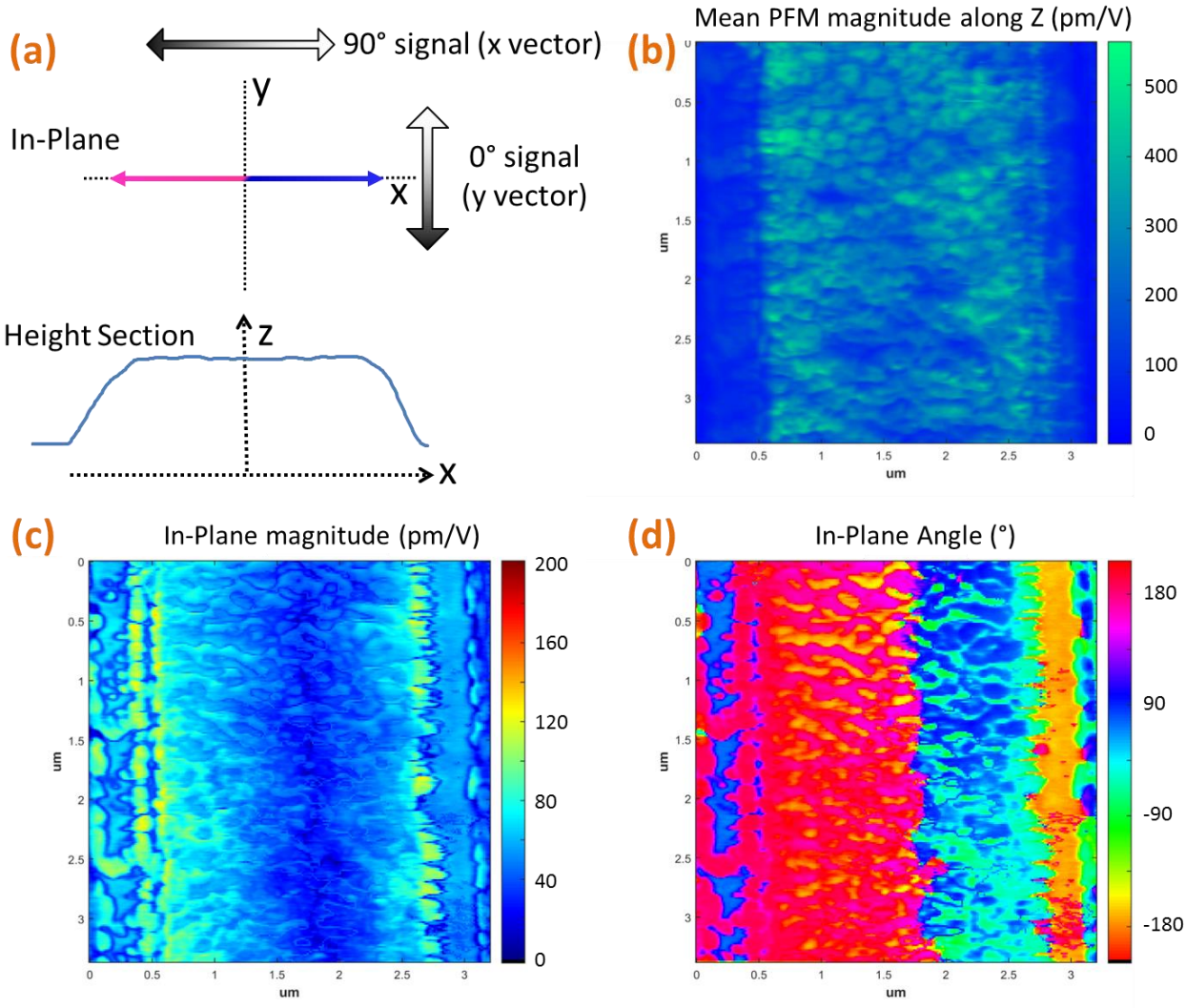

Figure 5.10. sketch of In-plane vectors along x, y axis (a); Oout-of-Plane PFM magnitude of the 2 µm arm along z axis (b); In-Plane PFM magnitude (c); In-Plane angles of orientations (d).

By applying this scheme, In-plane magnitude can be described with edge enhancement of amplitude of 150 pm/V and a sharp dark line of 30 pm/V indicating almost no In-Plane

amplitude near the center of the microstructure. Two orientation angles resulted as well of approximately 0° (blue), and 180° (red) respectively. There are some domains with different color contrast which is believed to be due to topographic convolution at grain boundaries.

Since we now know the OP and IP amplitude at x, y and z axis, the radial response R can be calculated as: $R = \sqrt{x^2 + y^2 + z^2}$ shown in Figure 5.11 (b). Figure (a) demonstrates the map of radial response with edge enhancement of ~2x factor. The elevation angle between R and in plane specified as ψ is calculated in figure (c) revealing dominating 60°; it suggest OP magnitude is much stronger than the IP magnitude. There are some grains with -60° which is probably due to phase wrapping error. Azimuthal angle θ' showed in Figure 5.11 (d) is also described as In-Plane angle in Figure 5.10 (d).

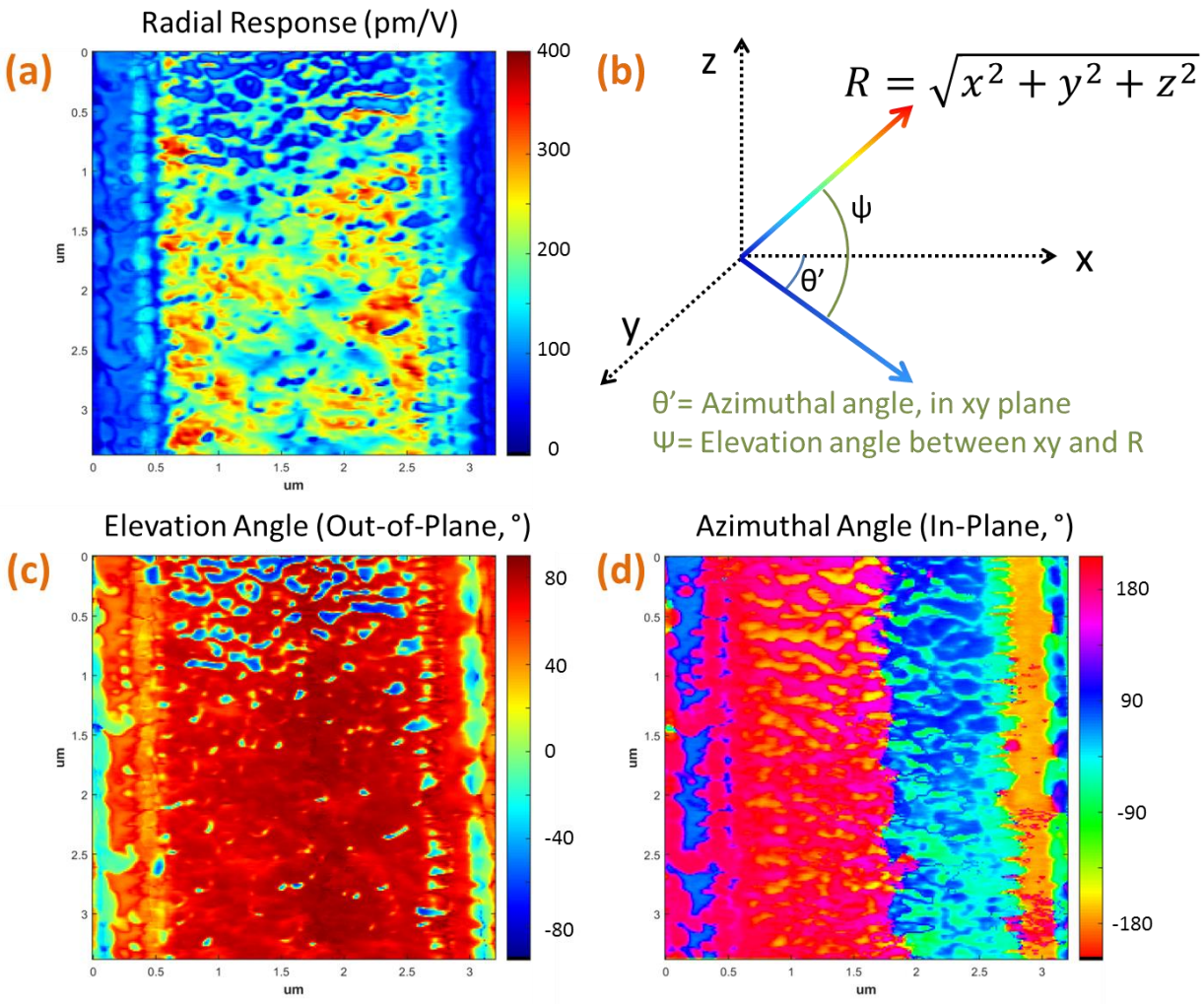

Figure 5.11. Radial response of overall signals (a); (b) sketch of how radial amplitude and angle calculated (b); Elevation angle ψ (c); Azimuthal angle θ' (d).

By analyzing cross-section values along the arm features, plots of radial amplitude can be extracted in Figure 5.12 (a) and (b). Figure (a) shows the cross-section of amplitude in x, y, z and R vector. The mean amplitude of r vector (Vr) in green line and of z vector (Vz) in purple line has similar shape with slightly higher magnitude because the amplitude of Vr is a calculation of Vz, Vx and Vy. Amplitude of Vy is nearly a straight line suggesting equal signal along y axis. Topography in blue has also been superimposed to demonstrate the position of on-arm and off-walls. If we only consider the magnitude of Vx disregarding the orientations, a "V" shape orange

line has been plotted in Figure 5.12 (b) showing a minimum value in the center and maximum signals at edges which are similar to the trend of Vertical signal (Vz). The interesting fact of linear increase of magnitude from center to edges which is unlike Out-of-Plane signal with a "U" shape may give rise to the lateral signal behaving like a thermal expansion coefficient. In other words, the IP signal is gradually increasing along the edges. The In-Plane signal of individual grains orients antiparallel to each other at left and right edges. Visually combining all of this data, (c) presents the topography of the 2 μm arm with a 3-d perspective, and superimposes a sparse array of blue vectors with magnitude and direction indicating the strength and 3-dimensional orientation of the local piezoresponse.

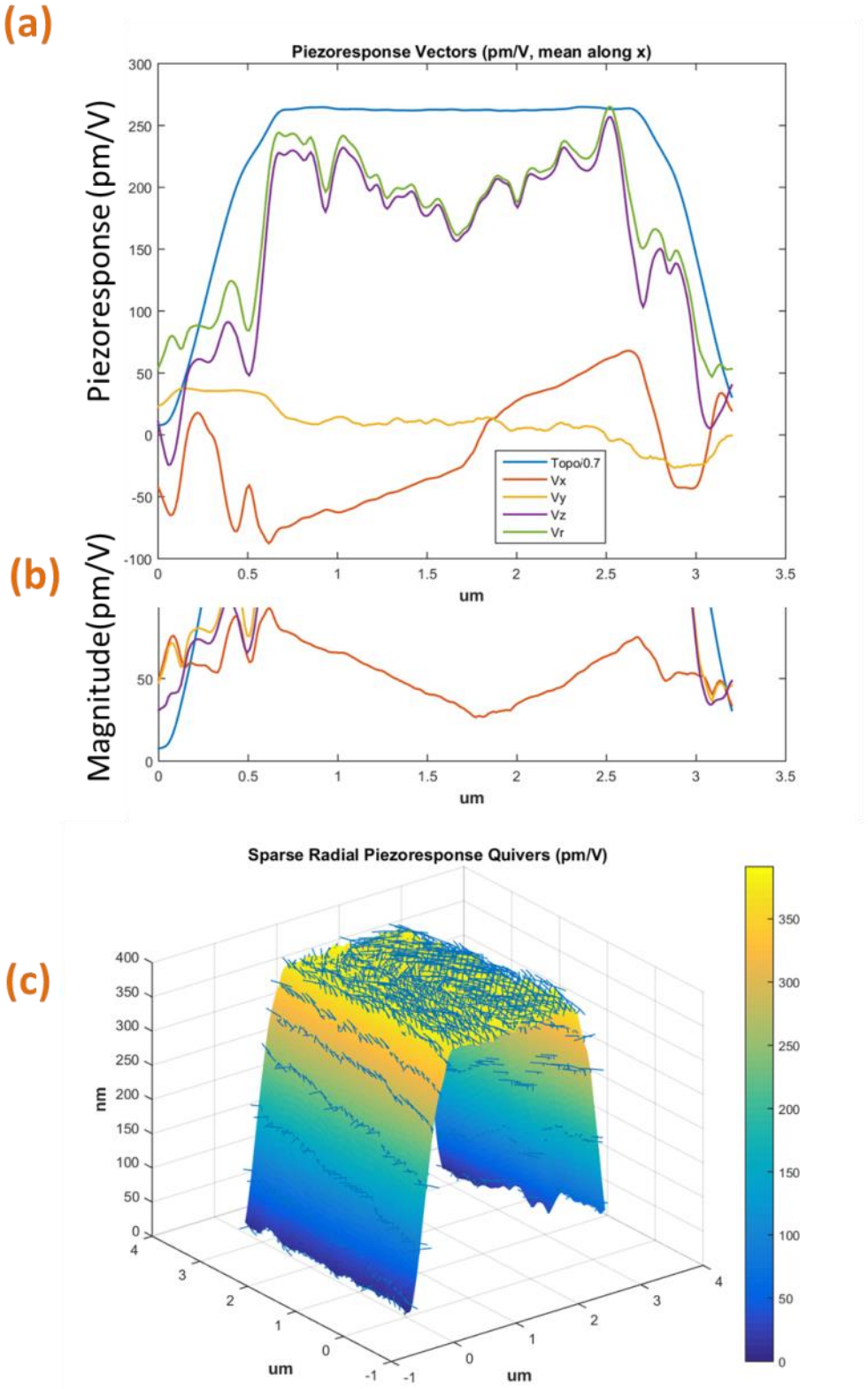

Figure 5.12. piezoresponse of all vectors (a); magnitude of in-pane x vector (b); sparse radical response (c).

A two-dimensional version of Figure 5.12 (c) is displayed in Figure 5.13 (a). If we extract the cross-section signal along the purple dotted line, i.e. the XZ plane, the mean piezo response is reported in Figure 5.13 (b). Again, there are stronger peaks at both edges of the arm as compared to the center, vectored away from the center of the microstructure. Little signal is detected off the wall since there is no electrode. The same scheme has been applied for (c) to analyze the signal along the YZ plane as well (red dashed line). Since the microstructural feature extends indefinitely in the y direction, and any strain relief (or not) is uniform along y since the distance from the strain-relieving free edge is fixed, there is no notable piezo-enhancement.

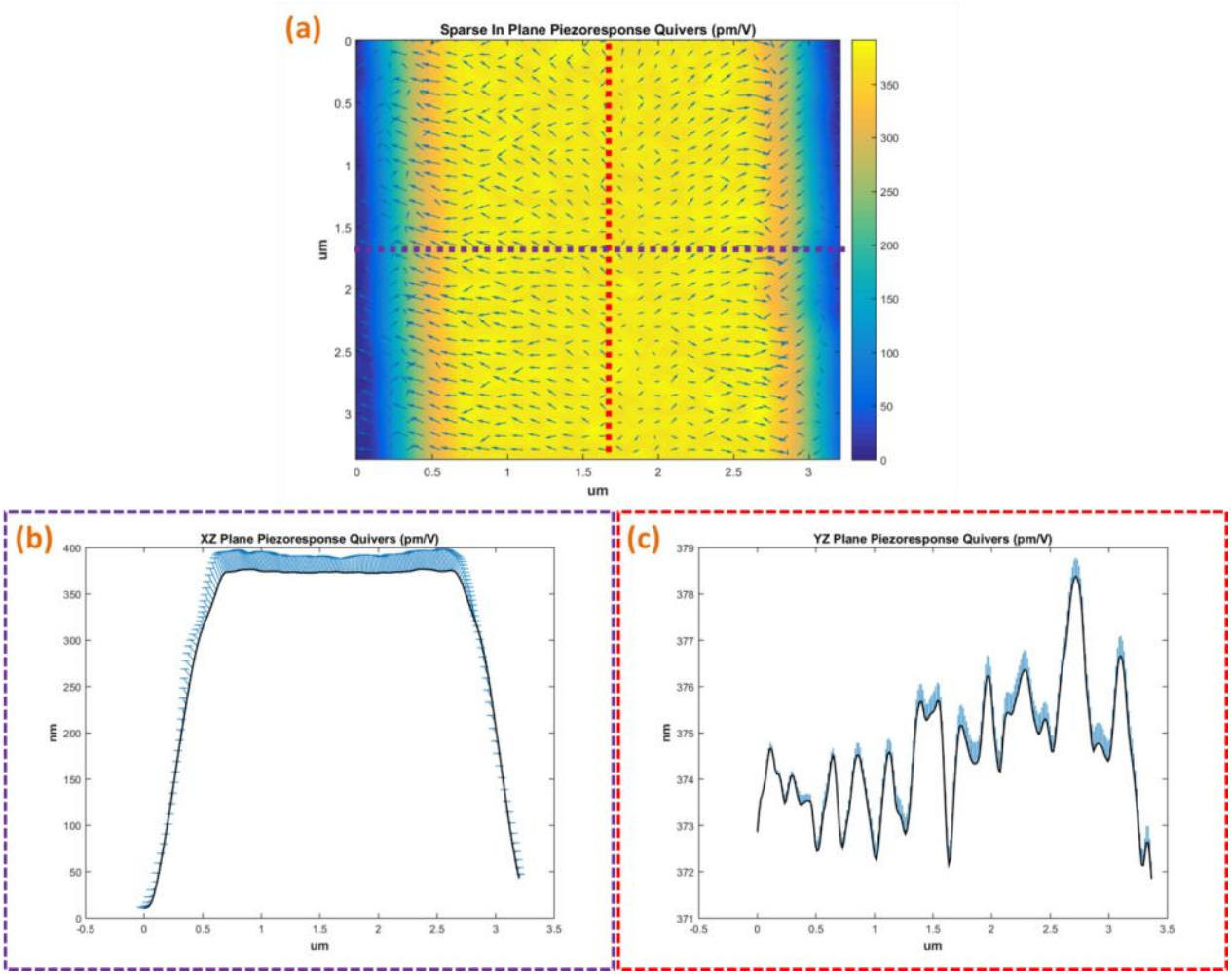

Figure 5.13. sparse of IP Piezo response quivers (a); cross section of the piezo response in XZ plane (b); piezo response in YZ plane (c).

5.4.2 4 µm Structure signal

A primary concern for PFM measurements of microstructures with such an experimental configuration is that the lateral signal may relate to cantilever torsion due to the vertical film contraction or expansion upon applied biasing. To eliminate this influence, a wider 4 µm-arm structure was investigated at its end, which hypothetically should reveal both x and y vectored piezoelectric enhancements. By aligning the probe horizontally to the structure as discussed earlier, we recorded the lateral and normal signal in perpendicular directions as shown in Figure 5.14. Once again, there is a strong In-Plane signal with 180° phase contrast.

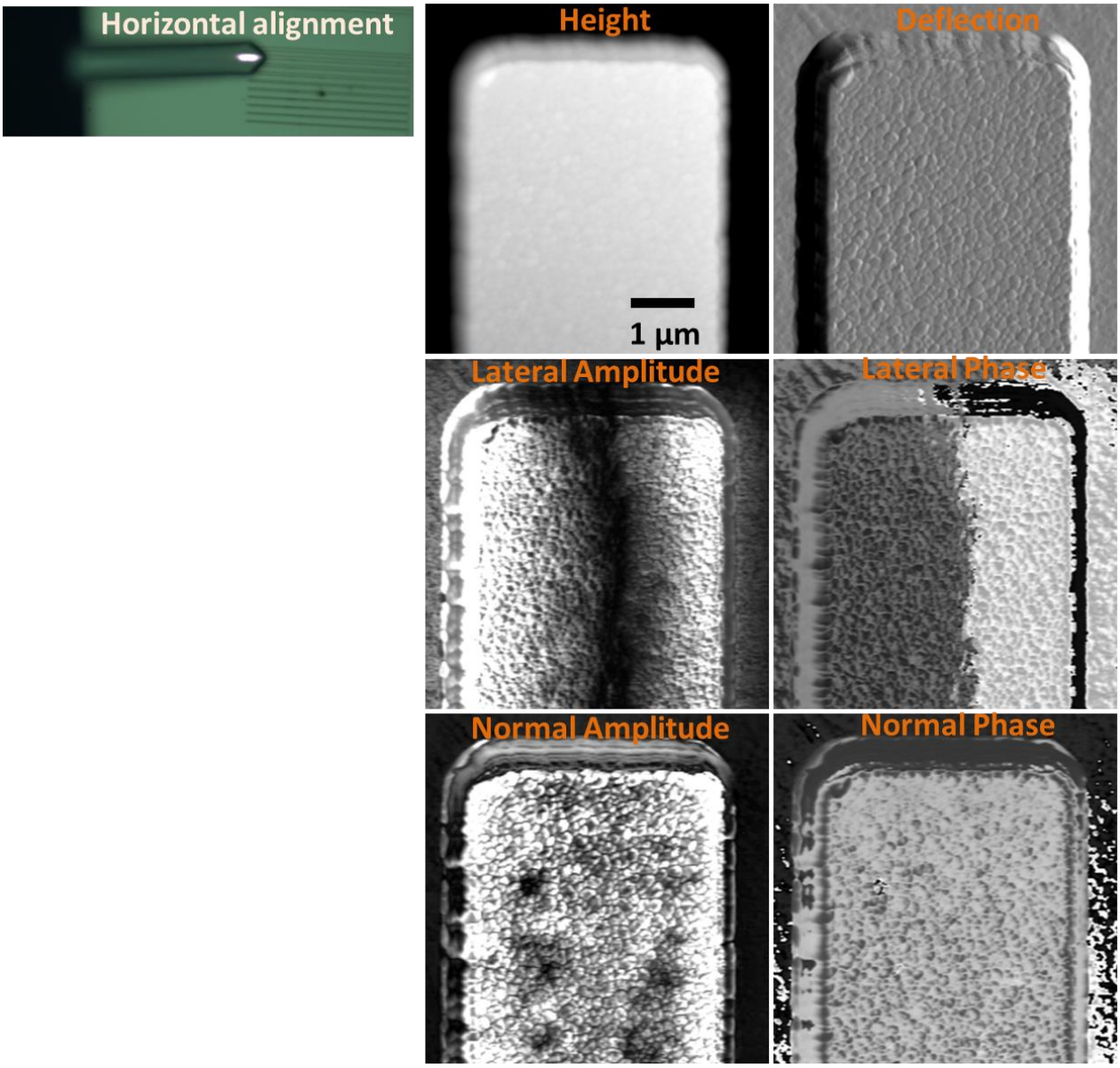

Figure 5.14. Height, deflection, Amplitude and Phase images of Lateral signals when the probe aligned 0° to the arm structures.

Perpendicular alignment is also shown here in Figure 5.15 with no significant phase contrast suggesting the same In-Plane orientation as 2 µm mesa. The experiment frequency is 933 kHz for Lateral measurement and 486 kHz for normal signal with 0.9 V DC signal superimposed on 1.8 V AC (peak to peak). Therefore, two antiparallel IP orientations can be determined as shown in Figure 5.10 (d).

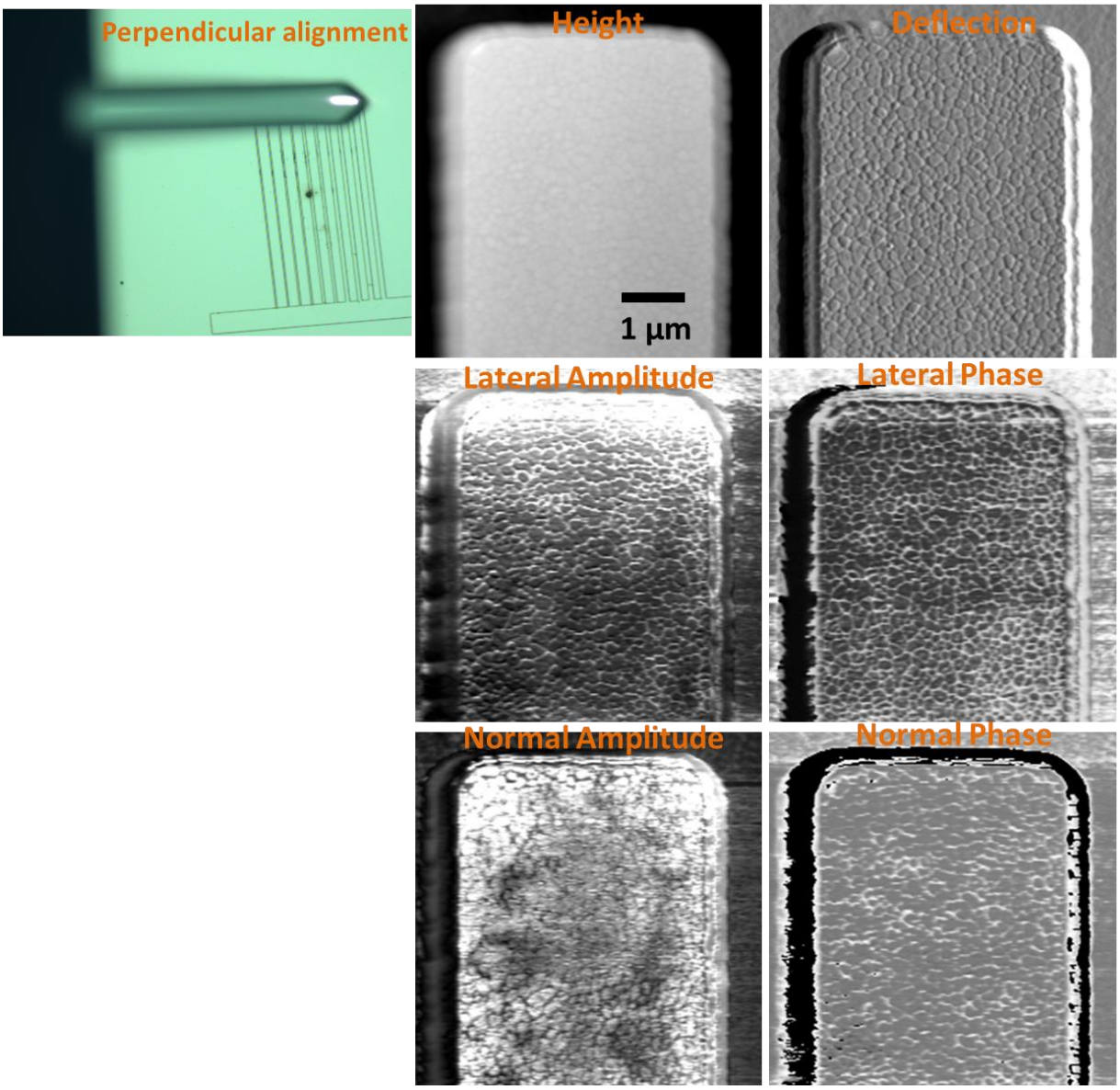

Figure 5.15. Height, deflection, Amplitude and Phase images of Lateral signals when the probe aligned 90° to the arm structures.

The radial response has been mapped in Figure 5.16 (a) of fine resolved grains with different piezo response. This 4 μm structure with 3 relaxed edges generates more freedom to piezo excitation giving that the signal at all edges are increased by ~250 pm/V compared to the central (most strained) region. Furthermore, the highest amplitude response up to 400 pm/V is located at the upper corners of the microstructure, as these locations experience strain relaxation along both x and y axes. This is clearly identified in Figure 5.16 (b), which again depicts the In-Plane signal as blue vectors superimposed on the mesa topography. As before, the local piezoresponse, and hence the corresponding quivers for visualizing this signal, are aligned away from the center of the structure.

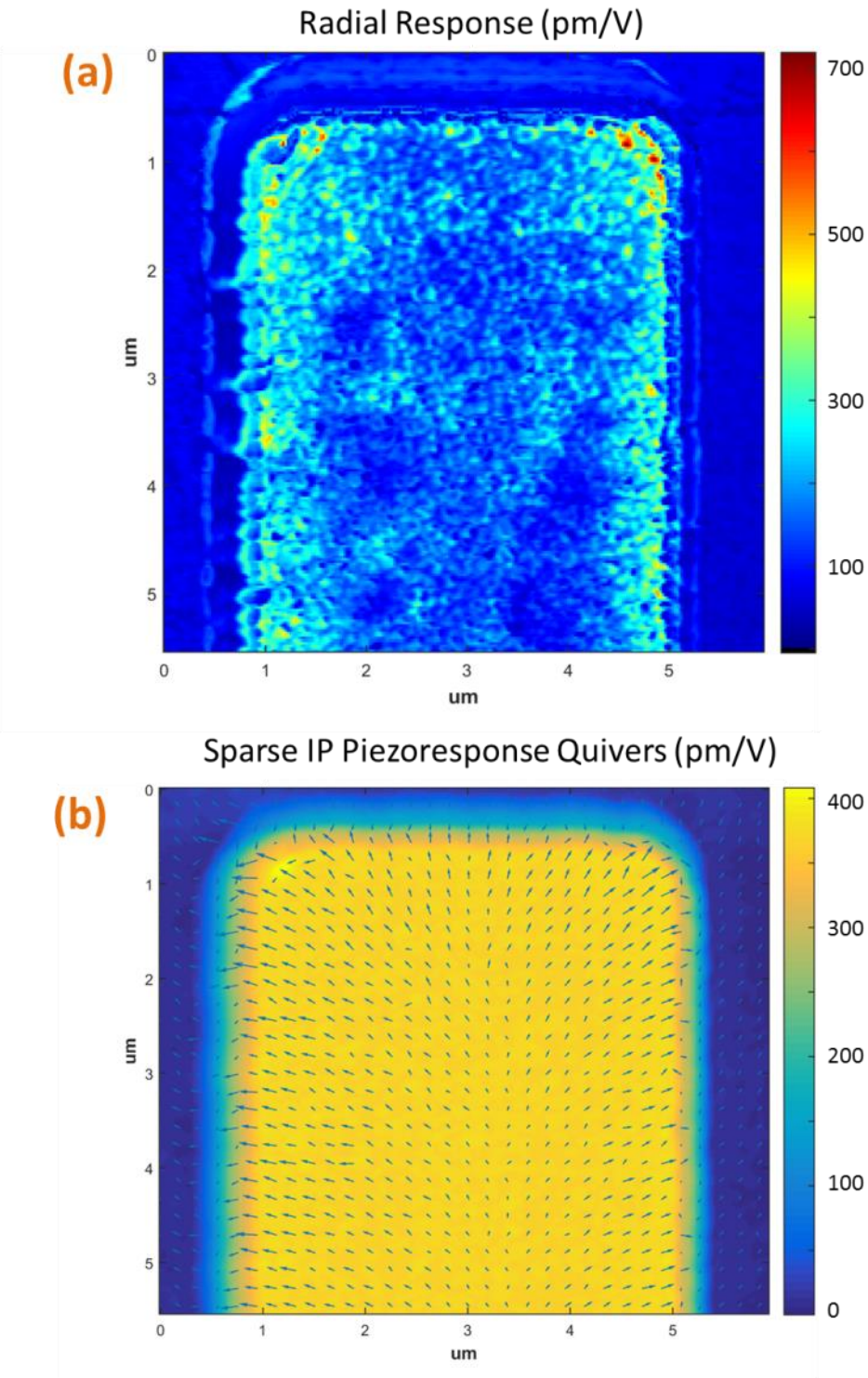

Figure 5.16. Radial response of the 4 µm arm (a), and sparse In-plane piezo response quivers (b).

The mean cross section of topography and piezo response magnitude, for xy, xz and yz planes, is plotted in Figure 5.17. The magnitude of normal signal in yz plane (purple line) and radial response in xz plane (yellow line) are close with peaks at both ends and a long base line in the center forming a wide "U" shape. The peak signals are 600nm away from mesa walls and the baseline is thus ~2.8 μm in width. The piezoelectric enhancement factor is 2x, consistent with the prior results.

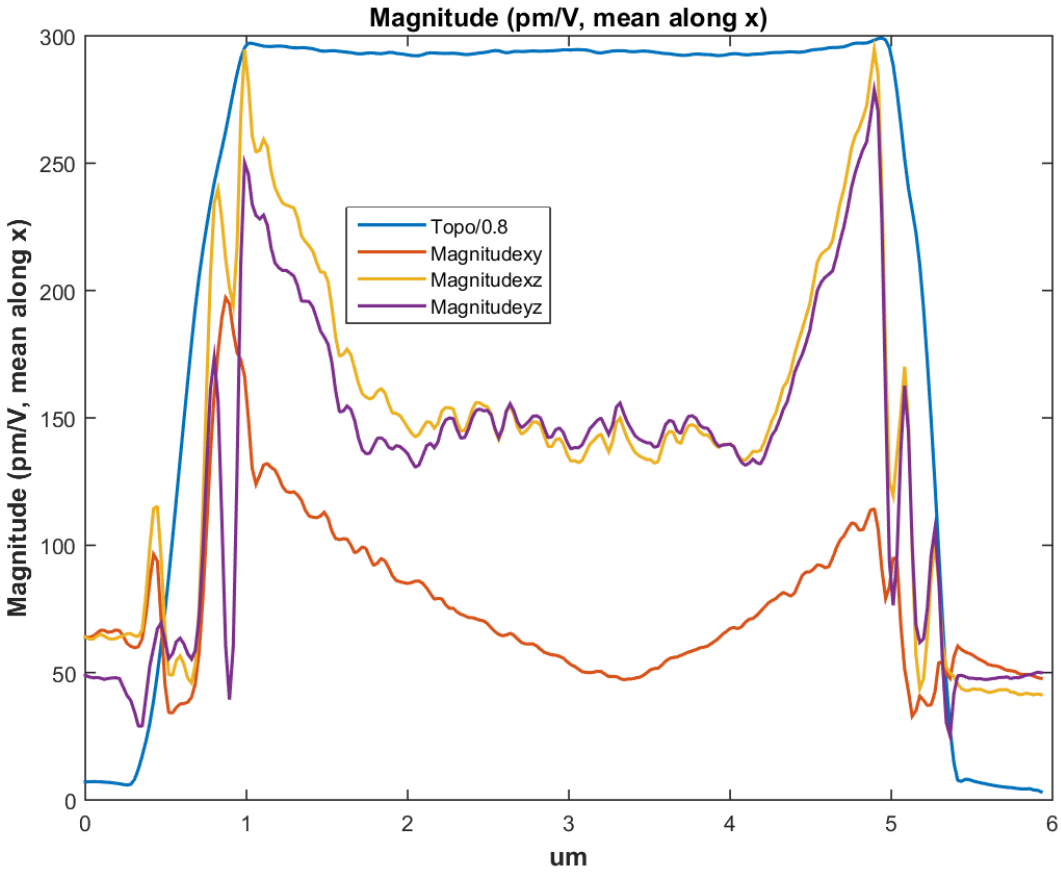

Figure 5.17. Mean magnitude of piezo response in xy, xz and yz planes as well as topographic information.

If the film experience a surface height change in normal direction which is generated by voltage, possible lateral cantilever torsion may be provoked as a result with same shape of OP strain cupping effect shown in Figure 5.18. The orange sketch in this figure represents the OP pfm

signal with strong enhancement at both edges. Therefore, a cupping effect occurs when the probe scanned at the left edge experiencing a vertical surface displacement and bend to the left side with external voltage; the probe would bend accordingly to the right side when scanning at right edge. Along the centered region with no apparent surface change, the probe would scan parallel to the surface. This signal due to cupping effect would be strongly identical to the topographic change, i.e. the OP pfm signal.

The acquired lateral signal in xy plane however has a sharp “V” shape with a minimum value near the center region and gradual increment along the width of the mesa in both left and right directions which is dramatically different from the normal data. Hence, this lateral signal is not induced by the cupping effect of OP signal.

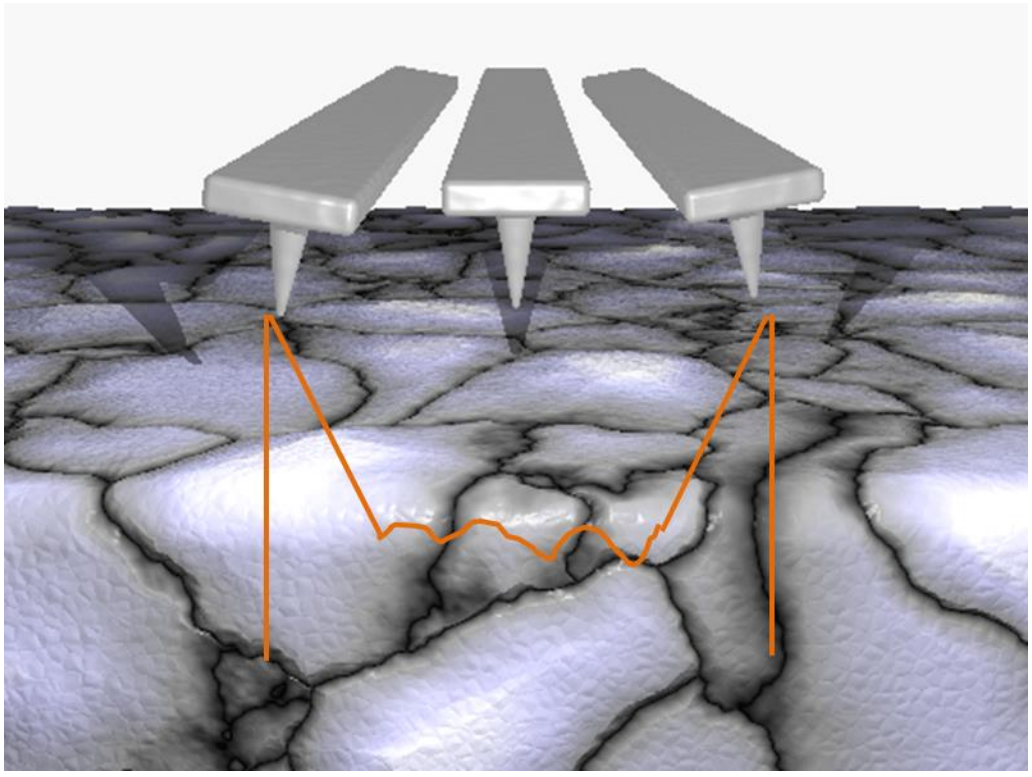

Figure 5.18. Cupping effect when tip scan along the arm.

5.5 Nano-sculpting on PMN-PT Film

PMN-PT film shows piezoelectric response strongly depending on mesa size or the ratio of lateral dimension and thickness which is related to strain behavior. Hence we propose a further procedure via controlling the degree of declamping to influence d33 coefficients and possibly also domain dynamics. Here we employ the nano-sculpting technique to machine mesas of approximately same size with different strain relief, i.e. different depth of trenches around the mesas. We fabricate three mesas centered on the 100 um sized "bulk" like PMN-PT film shown in Figure 5.19; white blank regions were PMN-PT that was removed in this manner while other remains remain unchanged.

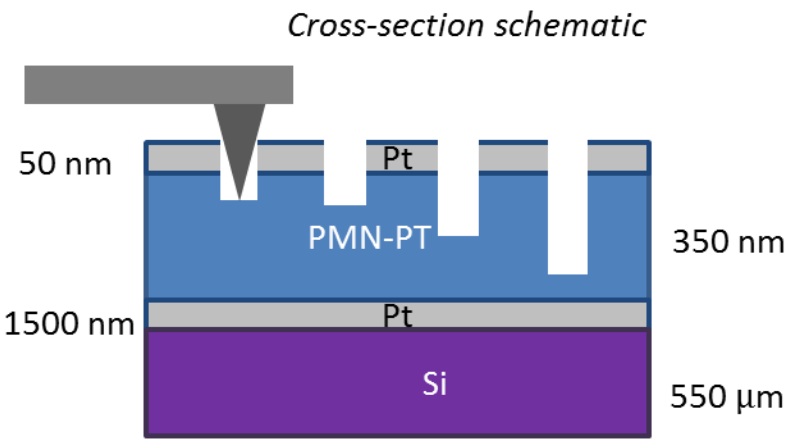

Figure 5.19. Cross-section sketch of PMN-PT films after nano-sculpting.

Figure 5.20 displays the AFM topographic image of 3 such mesas with similar sizes at the top. The trench depth is 200 nm, 280 nm, and 450 nm from left to right at the bottom image. The desired mesa size is ~ 1.5 µm x 0.8 µm; though the extensive milling necessary for deeper trenching caused the more-exposed mesas at right to be slightly smaller than the mesas at left. In terms of strain, the left mesa has the least strain relief; meanwhile the mesa on the right experiences the highest degree of substrate declamping.

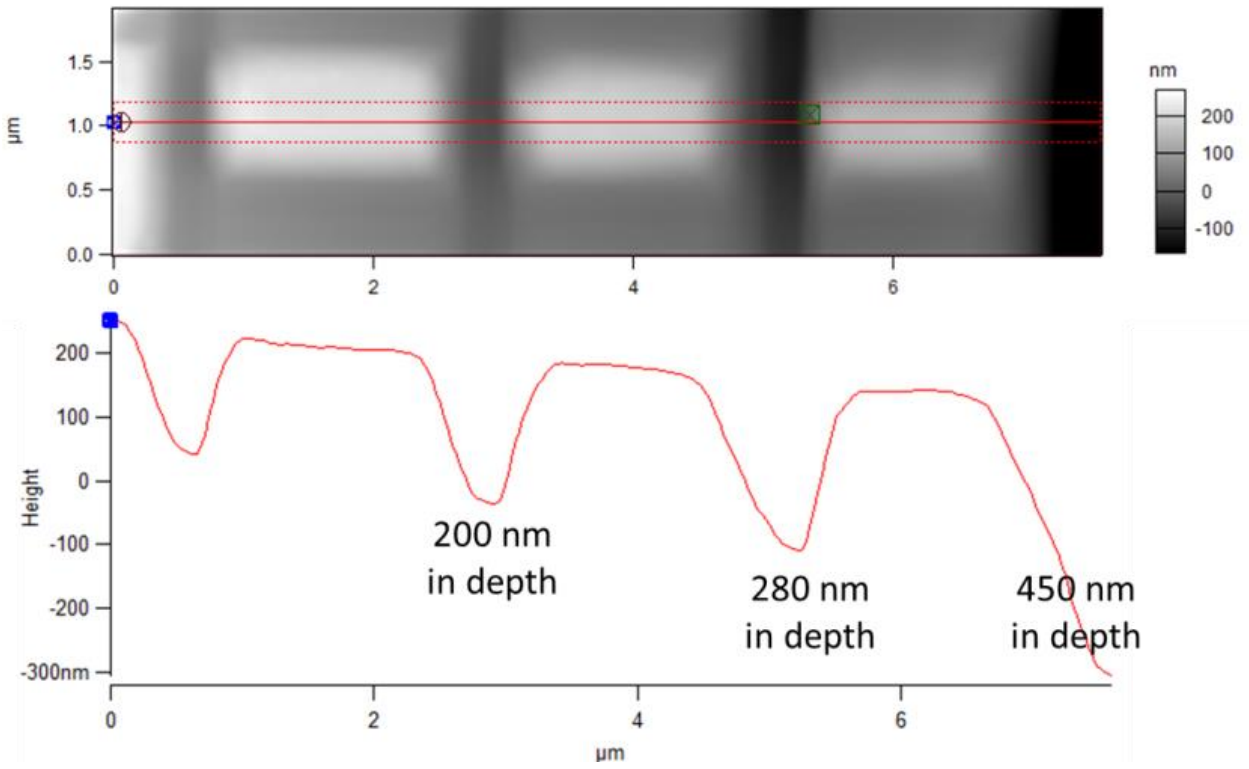

Figure 5.20. AFM topography (top) and trench depths of mesas in cross-section (Bottom).

By applying 1.2 Vpp AC plus 0.6 V DC to the bottom electrode and floating the conductive diamond coated AFM probe acting as the top electrode, the PFM normal amplitude was recorded at 439 kHz. Figure 5.21 presents the resulting normal piezo-amplitude superimposed on the height of the successively more strain-relieved mesas. The amplitude for the most relieved mesa, at right, is as high as 120 mV while the other two mesas are ~ 90 mV. This significant result corresponds to our hypothesis that strain engineering by AFM based nanosculpting may control the local piezo response.

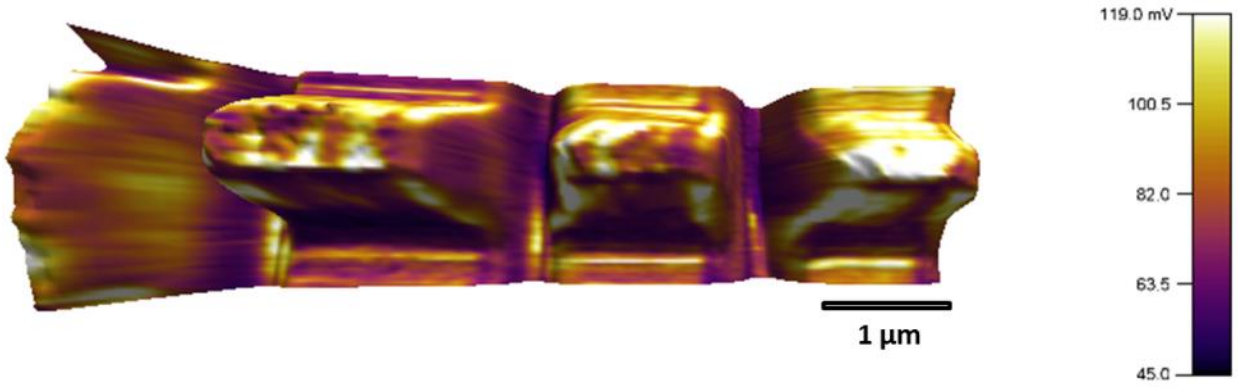

Figure 5.21. 3D Image of PFM amplitude superimposed on Height of 3 mesas.

To quantify the intrinsic d33 (at 0 V DC bias), we use the same pixel by pixel approach as described earlier to map out the piezo response. A DC voltage sweep is thus applied to the three mesas, ranging from 0.6 V to 1.5 V in multiple consecutive images, while measure the OP amplitude in Figure 5.22. As expected, the mesa at right always exhibits the strongest signal.

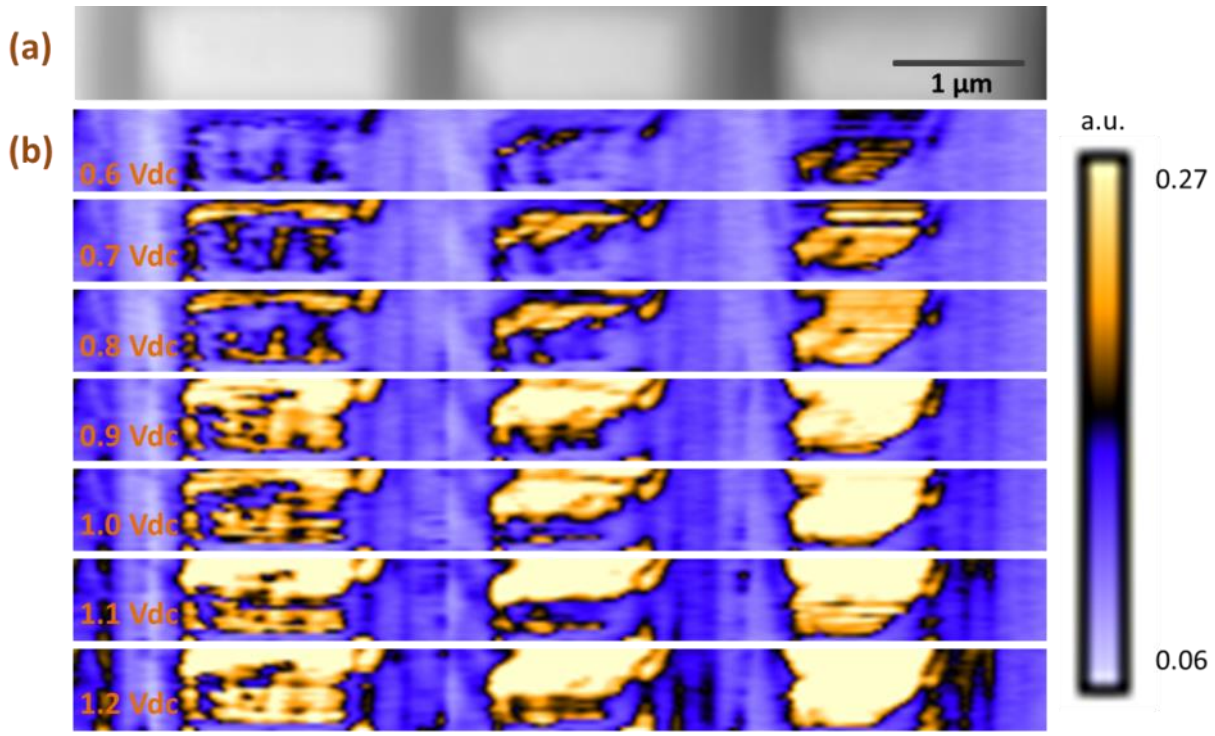

Figure 5.22. Height information (a), consecutive amplitude images from 0.6 V to 1.2 V.

Cross sections of this data, only DC voltages of 0.6 V, 0.8 V, 1 V and 1.2 V for simplicity, yield Figure 5.23 which clearly confirms the expected behavior. Topographic information in grey dashed line is shown in this figure as well to indicate the position of mesas.

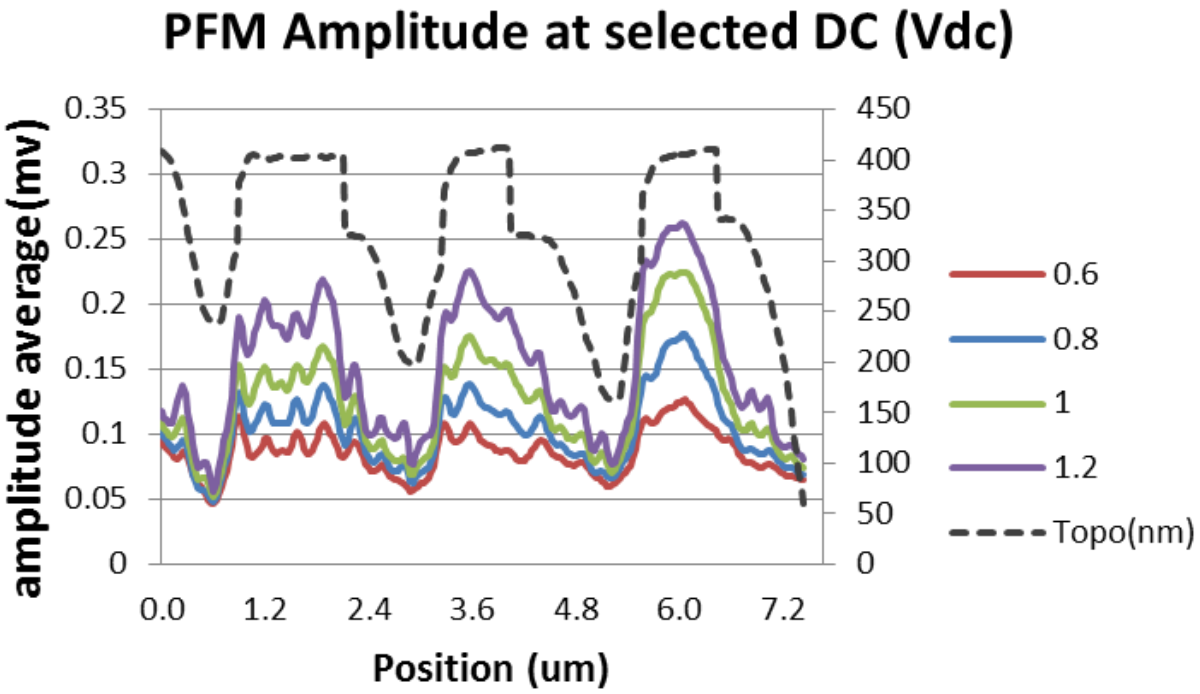

Figure 5.23. Average amplitude with selected DC voltages superimposed with topography.

With the application of MatLab code, the intercept of d33 (0 V) can be extrapolated pixel by pixel in Figure 5.24 (b), again figure (a) shows the topography. By extracting the peak and mean value of d_{33} from the red dashed boxes in the map, a plot of d_{33} at 0 V with error for 3 mesas is depicted in Figure 5.24 (c). d_{33} for the mesa on the left is ~ 100 pm/V for the mean value and ~ 140 pm/V of the peak signal; ~ 150 pm/V and ~190pm/V for the right mesa which is 1.5x enhanced. Thus, we can confirm that more strain relief leads to a stronger piezoelectric response.

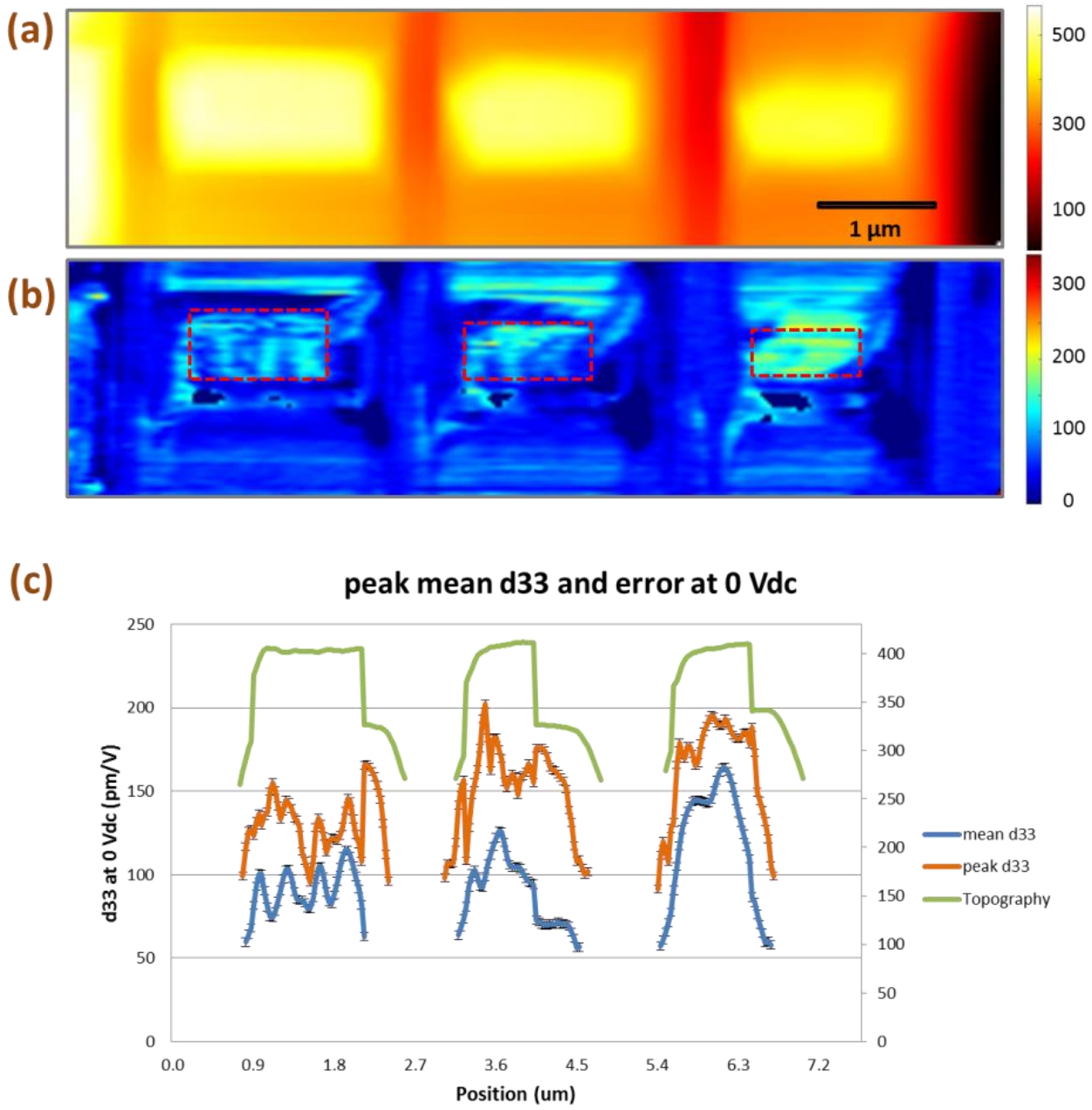

Figure 5.24. Topography (a); calculated map of d_{33} at 0 V (b); and plot of mean and peak d33 (c) only for the mesas (signals at trenches are removed for clarity).

5.6 Summary

This chapter describes the Out-of-Plane enhancement of microfabricated structures of PMN-PT measured by PFM. Piezoelectric coefficient d_{33} has been mapped for 2, 1 and 0.75 µm arm

features respectively pixel by pixel. By plotting the mean and peak d_{33} signal, 2 μm feature shows an enhancement at both edges of the arm with the enhancement range ~600 nm. d_{33} for 1 um arm has been improved across the entire arm and is higher than d_{33} for 2 um arm. 0.75 μm which is the narrowest structure has the most enhanced d_{33} value. Therefore, Out-of-Plane piezoelectric property can be improved by reducing size. XRD data with similar results confirms our PFM data.

As hypothesized, the In-Plane Piezoelectric property has also been enhanced due to geometric strain relief. By implementing nano-sculpting, patterned structures at the nanoscale can thus be fabricated with various strain-relieved conditions, which controls the extent of piezoelectric enhancement as well. Such unique OP and IP piezoelectric property investigations demonstrate the dependence of functional properties on local declamping, with implications for optimizing future piezoelectonic devices such as piezotronics, MEMS and NEMS devices, and other microactuators.

Chapter 6 Future Work

Several additional studies to further this research are proposed based on the results throughout the entire dissertation:

1. We have investigated the switching dynamics of PZT thin films with a-domains after strain relief via nano-sculpting technique. Thus the ferroelectic and ferroelastic switching of $BiFeO_3$ thin films can be studied as the next step due to its multiferroic properties and coupled magnetic switching to optimize future magnetoelectronics devices[72]. By detecting the OP and IP signal, the switching path of nanoscale BFO mesa can be determined and compared with continuous film. By relaxing the mesa, switching steps could be possibly alternated as a result of switching energy change. And since the mesa is isolated from adjacent domains, the switching process would be more stabilized without any back-switching. To obtain these results, PFM can be utilized to monitor the switching dynamics path before and after nano-sculpting for comparison by recording the OP and IP signals. In addition, ferroelectric hysteresis loop can be mapped before and after to compare the coercive voltages.
2. Dislocations might be introduced into the ferroelectric mesa during the milling process. Though AFM is not capable of detecting such damage, High-Resolution TEM can be utilized in the future to study the cross section of the fabricated mesas. The existence and influence of any microcracks, dislocation networks, or other microstructural defects could then be revealed by comparing TEM and AFM based measurements for nano-sculpted regions and adjacent, unmodified, continuous thin films.

3. We can fabricate ferroelectric mesas at small length scales as described in the thesis. However, the sizes and side-wall angles are strongly dependent on the geometry of the sculpting probe. The probe employed in these experiments has a tip radius ~100 nm, and a conical half-angle of ~15°. To achieve mesas at much smaller scales in the future, we can customize the probe shape into a columnar structure instead of a pyramid. The tip radius can be reduced to several nanometers as well. Therefore, mesas with different geometries can be obtained by this technique which would be expected to yield even more significant piezoelectric and ferroelectric enhancements due to the controllable feature aspect ratio. Crucially, such patterning down to a few nanometers is feasible which FIB cannot achieve due to widely demonstrated ion beam damage. Moreover, many functional properties such as ferroelectricity, magnetism, and thermal coefficients can be measured to assess and further refine the property enhancements that result from such micro/nano fabrication.
4. Since we report the piezoelectric coefficient can be controlled by strain relief conditions, another approach is to measure the electrical conductivity of ferroelectric mesa domain walls. Some paper have shown the conductivity of domain walls in BFO[97, 98], it is critical to reveal and understand the charge distribution of the domain wall on the film surface as well as the electrical properties along the edges. For many future ferroic devices, the focus of functionality can be on the domain walls rather than the domains. By controlling the location of domain walls with electric voltage, device conductance can be modified to achieve nanoscale functionalities.

Overall, in this dissertation I have demonstrated the use of AFM to measure and manipulate the piezoelectronic properties and domain dynamics of ferroelectric thin films. Accordingly, we can

engineer ferroelectric mesas with distinct patterns to achieve desired properties. Furthermore, such work can help to address some of the many remaining questions in the ferroeletrics field. These include how reducing sizes affects the functional properties, how this may influence device reliability, etc. The drawbacks of the nano-sculpting technique must be studied as well. To resolve these questions, variations of Atomic Force Microscopy are an ideal approach, especially when combined with other tools and modelling as exemplified by the work here on enhanced piezoelectricity for microstructured films. In the future, ferroeletric and ferroelastic switching needs to be better understood with various strain relief conditions and mesa sizes that we can control. Functional properties relying on domain walls are also essential to understand and leverage, by uniquely tracking their location as demonstrated herein, as well as any resulting electrical responses especially in terms of useful conductivity mechanisms at certain domain walls. These insights into ferroelectric microstructures can lead to improving the performance, as well as new designs, of future electronic devices.

Chapter 7 Conclusions

This dissertation investigates piezoelectric properties and ferroelectric switching dynamics for PZT and PMN-PT thin films with engineered strain and strain relief.

Chapter 1 provides a general introduction about piezoelectric properties and ferroelectric domains, and their detection especially at the nanoscale primarily using Piezo Force Microscopy (PFM). Chapter 2 presented details for how piezo force microscopy (PFM) is specifically used in the NanoMeasurement Labs to map domains, both out of plane and in plane, simultaneously.

Chapter 3 presents investigations of out-of-plane and in-plane ferroelctric domain configurations for relaxed PZT thin films which exhibit patterns of 90° domains. Domain switching dynamics were observed step by step in the continuous film, both using standard PFM methods and even by tracking topography changes.

Chapter 4 extends such studies, but for films with strain relief via geometric microstructuring. This is achieved by nano-sculpting trenches in the continuous film to isolate mesas of PZT. One concern may be that this process will damage the specimen, but ferroelectric properties for nanostructured mesas are confirmed to be equivalent to continuous thin films. In addition, the switching dynamics of ferroelectric mesas with various strain relief were studied.

Furthermore, piezoelectric coefficients have been measured by PFM as well as XRD on patterned PMN-PT thin films with different arm widths in chapter 5. In-plane PFM signal of the arm structures have also been reported. A higher piezo coefficient has been observed on the sidewalls of arm features suggesting that partially strain relieved regions would experience high piezo coefficient. Moreover, the nano-sculpting technique was also applied on the PMN-PT film to fabricate mesas with different strain conditions and d_{33} was also measured by PFM in chapter

5. By controlling the sizes and strain-relief status of the PMN-PT thin films, piezoelectric properties have been investigated related to the extent of film declamping.

Ultimately this work demonstrates that novel tools based on AFM, especially nanosculpting as well as simultaneous OP and IP PFM, are effective tools for investigating the piezoelectric properties of strained ferroelectrics that can ultimately be leveraged to optimize future memory devices.

Chapter 8 References

[1] N. Setter, et al., Ferroelectric thin films: Review of materials, properties, and applications, JOURNAL OF APPLIED PHYSICS, 100 (2006).
[2] A.K. Tagantsev, V.O. Sherman, K.F. Astafiev, J. Venkatesh, N. Setter, Ferroelectric Materials for Microwave Tunable Applications, Journal of Electroceramics, 11 (2003).
[3] L.E. Cross, Ferroelectric materials for electromechanical transducer applications, Materials Chemistry and Physics, 43 (1995).
[4] C.A.-P.d. Araujo, J.D. Cuchiara, L.D. McMillan, M.C. Scott, J.F. Scott, Fatigue-free ferroelectric capacitors with platinum electrodes, Nature, 374 (1995).
[5] W. Knzig, Ferroelectrics and Antiferroelectrics, 1957.
[6] S. Das, J. Appenzeller, FETRAM. An Organic Ferroelectric Material Based Novel Random Access Memory Cell, Nano Letters, 11 (2011).
[7] O. Auciello, J.F. Scott, R. Ramesh, The Physics of Ferroelectric Memories, Physics Today, 51 (1998).
[8] D. Bonduranta, Ferroelectronic ram memory family for critical data storage, Ferroelectrics, 112 (1990).
[9] A.L. Kholkin, S.V. Kalinin, A. Roelofs, A. Gruverman, Review of Ferroelectric Domain Imaging by Piezoresponse Force Microscopy, in, Alexei Gruverman Publications, 2007, pp. 46.
[10] H. Ibach, H. Lüth, Solid-State Physics: An Introduction to Principles of Materials Science Springer, 2003.
[11] W.P. Mason, Piezoelectric Crystals and Their Application to Ultrasonics, D. Van Nostrand Company, 1950.
[12] K. Bhattacharya, G. Ravichandran, Ferroelectric Perovskites For Electromechanical Actuation, Acta Materialia, 51 (2003).
[13] B. Jaffe, Piezoelectric ceramics, Elsevier, 2012.
[14] D. Damjanovic, Ferroelectric, dielectric and piezoelectric properties of ferroelectric thin films and ceramics Reports on Progress in Physics, 61 (1998).
[15] M. Radmacher, R.W. Tillamnn, M. Fritz, H.E. Gaub, From molecules to cells: imaging soft samples with the atomic force microscope, Science, 257 (1992).
[16] M. Rief, F. Oesterhelt, B. Heymann, H.E. Gaub, Single Molecule Force Spectroscopy on Polysaccharides by Atomic Force Microscopy, Science, 275 (1997).
[17] E. Henderson, P.G. Haydon, D.S. Sakaguchi, Actin filament dynamics in living glial cells imaged by atomic force microscopy, Science, 257 (1992).
[18] P.K. Hansma, V.B. Elings, O. Marti, C.E. Bracker, Scanning Tunneling Microscopy and Atomic Force Microscopy: Application to Biology and Technology, Science, 209 (1988).
[19] R.A. Wilson, H.A. Bullen, Introduction to Scanning Probe Microscopy (SPM): Basic Theory Atomic Force Microscopy (AFM), Creative Commons Attribution-Noncommercial-Share Alike, 2 (2006).
[20] Q. Zhong, D. Inniss, K. Kjoller, V.B. Elings, Fractured polymer/silica fiber surface studied by tapping mode atomic force microscopy, Surface Science Letters, 290 (1993).
[21] R.S. McLean, B.B. Sauer, Tapping-Mode AFM Studies Using Phase Detection for Resolution of Nanophases in Segmented Polyurethanes and Other Block Copolymers, Macromolecules, 30 (1997).
[22] S.N. Magonov, V. Elings, M.H. Whangbo, Phase imaging and stiffness in tapping-mode atomic force microscopy, Surface Science Letters, 375 (1997).
[23] S. Jesse, A.P. Baddorf, S.V. Kalinin, Switching spectroscopy piezoresponse force microscopy of ferroelectric materials, Applied Physics letters, 88 (2006).

[24] B.J. Rodriguez, R.J. Nemanich, A.K.A. Gruverman, S.V. Kalinin, K. Terabe, X.Y. Liu, K. Kitamura, Domain growth kinetics in lithium niobate single crystals studied by piezoresponse force microscopy, Applied Physics letters, 86 (2005).
[25] A. Gruverman, S.V. Kalinin, Piezoresponse force microscopy and recent advances in nanoscale studies of ferroelectrics, Journal of Materials Science, 41 (2006).
[26] R. Proksch, S. Kalinin, Piezoresponse force microscopy with asylum research AFMs, PFM App Note, (2008).
[27] C.A. Stutt, Low-Frequency Spectrum of Lock-in Amplifiers, in, Massachusetts Institute of Technology, 1949, pp. 22.
[28] S. Jesse, A.P. Baddorf, S.V. Kalinin, Dynamic behaviour in piezoresponse force microscopy, Nanotechnology, 17 (2006).
[29] N.S. Partner, Piezoelectric Force Microscopy (PFM), in, pp. 6.
[30] G. Binnig, C.F. Quate, C. Gerber, Atomic Force Microscope, PHYSICAL REVIEW LETTERS, 56 (1986).
[31] K. Lefki, G. Dormans, Measurement of piezoelectric coefficients of ferroelectric thin films, Journal of applied physics, 76 (1994).
[32] J.F. Shepard Jr, F. Chu, I. Kanno, S. Trolier-McKinstry, Characterization and aging response of the d31 piezoelectric coefficient of lead zirconate titanate thin films, Journal of applied physics, 85 (1999).
[33] P. Ceramics, Principles and Applications, Pennsylvania: APC International Ltd, (2006).
[34] J. Heron, J. Bosse, Q. He, Y. Gao, M. Trassin, L. Ye, J. Clarkson, C. Wang, J. Liu, S. Salahuddin, Deterministic switching of ferromagnetism at room temperature using an electric field, Nature, 516 (2014) 370-373.
[35] D. Li, D.A. Bonnell, Controlled patterning of ferroelectric domains: fundamental concepts and applications, Annu. Rev. Mater. Res., 38 (2008) 351-368.
[36] W. Zhang, K. Bhattacharya, A computational model of ferroelectric domains. Part I: model formulation and domain switching, Acta Materialia, 53 (2004).
[37] J.Y. Li, R.C. Rogan, E. Üstündag, K. Bhattacharya, Domain switching in polycrystalline ferroelectric ceramics, Nature Materials, 4 (2005).
[38] S. Hashimoto, H. Orihara, Y. Ishibashi, Study on D-E Hysteresis Loop of TGS Based on the Avrami-Type Model, Journal of the Physical Society of Japan, 63 (1994) 1601-1610.
[39] A.N. Kolmogorov, I.G. Petrovskii, N.S. Piskunov, Etude de l'équation de la diffusion avec croissance de la quantité de matiere et son applicationa un probleme biologique, Moscow Univ. Math. Bull, 1 (1937).
[40] T. Steinkop, Finite-element Modelling of Ferroic Domain Switching in Piezoelectric Ceramics, Journal of the European Ceramic Society, 19 (1999).
[41] A.K. Tagantsev, I. Stolichnov, N. Setter, J.S. Cross, M. Tsukada, Non-Kolmogorov-Avrami switching kinetics in ferroelectric thin films, Physical Review B, 66 (2002) 214109.
[42] D.L.a.D.A. Bonnel, Controlled Patterning of Ferroelectric Domains: Fundamental Concepts and Applications, Annual Review of Materials Research, 38 (2008).
[43] D. Damjanovic, Ferroelectric, dielectric and piezoelectric properties of ferroelectric thin films and ceramics, Reports on Progress in Physics, 61 (1998).
[44] R. Moazzami, C. Hu, W.H. Shepherd, Electrical Characteristics of Ferroelectric PZT Thin Films for DRAM Applications, IEEE Transactions on Electron Devices, 39 (1992).
[45] P. Muralt, PZT Thin Films for Microsensors and Actuators: Where Do We Stand?, IEEE Transactions on Ultrasonics, Ferroelectrics, and Frequency Control 47 (2000).
[46] M. Okada, K. Tominaga, T. Araki, S. Katayama, Y. Sakashita, Metalorganic Chemical Vapor Deposition of c-Axis Oriented PZT Thin Films, Japanese Journal of Applied Physics, 29 (1990).
[47] K.D. Budd, S.K. Dey, D.A. Payne, Sol-Gel Processing of PbTiO3, PbZrO3, PZT, and PLZT thin films, in, Inst of Ceramics, Stoke-on-Trent, Engl, 1985, pp. 15.

[48] R. Castellano, L. Feinstein, Ion‐beam deposition of thin films of ferroelectric lead zirconate titanate (PZT), Journal of applied physics, 50 (1979).
[49] N.K. Clive A. Randall, John-Paul Kucera, Wenwu Cao, Thomas R. Shrout, Intrinsic and Extrinsic Size Effects in Fine-Grained Morphotropic-Phase-Boundary Lead Zirconate Titanate Ceramics, Journal of American Ceramic Society, 81 (1998).
[50] S.A. Mabud, The morphotropic phase boundary in PZT solid solutions, J. Appl. Cryst., 13 (1980).
[51] D. Damjanovic, A morphotropic phase boundary system based on polarization rotation and polarization extension, Applied Physics letters, 97 (2010).
[52] D.I. Woodward, J. Knudsen, I.M. Reaney, Review of crystal and domain structures in the PbZrxTi1−xO3 solid solution, Physical Review B, 72 (2005).
[53] A.D. Hilton, C.A. Randall, D.J. Barber, T.R. Shrout, TEM studies of Pb(Mg1/3Nb2/3)O3-PbTiO3 ferroelectric relaxors, Ferroelectrics, 93 (1989).
[54] M. Yoshida, S. Mori, N. Yamamoto, Y. Uesu, J.M. Kiat, Tem observation of polar domains in relaxor ferroelectric Pb(Mg1/3Nb2/3)O3, Ferroelectrics, 217 (1998).
[55] Y.H. Hu, H.M. Chan, Z.X. Wen, M.P. Harmer, Scanning Electron Microscopy and Transmission Electron Microscopy Study of Ferroelectric Domains in Doped BaTiO3, Journal of the American Ceramic Society, 69 (1986).
[56] C.T. Nelson, P. Gao, J.R. Jokisaari, C. Heikes, C. Adamo, A. Melville, S.-H. Baek, C.M. Folkman, B. Winchester, Y. Gu, Y. Liu, K. Zhang, E. Wang, J. Li, L.-Q. Chen, C.-B. Eom, D.G. Schlom, X. Pan, Domain Dynamics During Ferroelectric Switching, Science, 334 (2011) 968-971.
[57] X. Tan, Z. Xu, J. Shang, In situ transmission electron microscopy observations of electric-field-induced domain switching and microcracking in ferroelectric ceramics, Elsevier Science, 314 (2001).
[58] C. Canedy, H. Li, S. Alpay, L. Salamanca-Riba, A. Roytburd, R. Ramesh, Dielectric properties in heteroepitaxial Ba0. 6Sr0. 4TiO3 thin films: Effect of internal stresses and dislocation-type defects, Applied Physics letters, 77 (2000).
[59] G. Akcay, I. Misirlioglu, S. Alpay, Dielectric tunability of (110) oriented barium strontium titanate epitaxial films on (100) orthorhombic substrates, Applied Physics letters, 89 (2006).
[60] Q. Qiu, V. Nagarajan, S. Alpay, Film thickness versus misfit strain phase diagrams for epitaxial PbTiO 3 ultrathin ferroelectric films, Physical Review B, 78 (2008).
[61] R.K. Nalla, J.H. Kinney, R.O. Ritchie, Mechanistic fracture criteria for the failure of human cortical bone, Nature Materials, 2 (2003).
[62] V. Nagarajan, S. Alpay, C. Ganpule, B. Nagaraj, S. Aggarwal, E. Williams, A. Roytburd, R. Ramesh, Role of substrate on the dielectric and piezoelectric behavior of epitaxial lead magnesium niobate-lead titanate relaxor thin films, Applied Physics letters, 77 (2000).
[63] A. Roytburd, S. Alpay, V. Nagarajan, C. Ganpule, S. Aggarwal, E. Williams, R. Ramesh, Measurement of internal stresses via the polarization in epitaxial ferroelectric films, PHYSICAL REVIEW LETTERS, 85 (2000) 190.
[64] P. Heyliger, Traction-free vibration of layered elastic and piezoelectric rectangular parallelepipeds, The Journal of the Acoustical Society of America, 107 (2000).
[65] D.J. Billingsley, W.A. Bonass, N. Crampton, J. Kirkham, N.H. Thomson, Single-molecule studies of DNA transcription using atomic force microscopy, Physical Biology, 9 (2012).
[66] T. Shibataa, K. Unnob, E. Makinoc, Y. Itod, S. Shimada, Characterization of sputtered ZnO thin film as sensor and actuator for diamond AFM probe, Sensors and Actuators, 102 (2002).
[67] Nanosensors, Diamond Coated PointProbe® Plus Silicon-SPM-Probes, in, Nanosensors, 2002, pp. 4.
[68] S. Jesse, B. Mirman, S.V. Kalinin, Resonance enhancement in piezoresponse force microscopy: Mapping electromechanical activity, contact stiffness, and Q factor, Applied Physics letters, 89 (2006).
[69] A. Gruverman, D. Wu, J.F. Scott, Piezoresponse Force Microscopy Studies of Switching Behavior of Ferroelectric Capacitors on a 100-ns Time Scale, PHYSICAL REVIEW LETTERS, 100 (2008).

[70] V.V. Shvartsman, A.L. Kholkin, Domain structure of 0.8Pb„Mg1Õ3Nb2Õ3…O3-0.2PbTiO3 studied by piezoresponse force microscopy, Phys. Rev. B, 69 (2004).
[71] R. Nath, S. Hong, J.A. Klug, A. Imre, M.J. Bedzyk, R.S. Katiyar, O. Auciello, J.F. Scott, R. Ramesh, Effects of cantilever buckling on vector piezoresponse force microscopy imaging of ferroelectric domains in BiFeO3 nanostructures, Applied Physics letters, 96 (2010).
[72] J.T. Heron, J.L. Bosse, Q. He, Y. Gao, M. Trassin, L. Ye, J.D. Clarkson, C. Wang, J. Liu, S. Salahuddin, D.C. Ralph, D.G. Schlom, J. I´n˜iguez, B.D. Huey, R. Ramesh, Deterministic switching of ferromagnetism at room temperature using an electric field, Nature, 516 (2014).
[73] A.I. Khan, X. Marti, C. Serrao, R. Ramesh, S. Salahuddin, Voltage-Controlled Ferroelastic Switching in Pb(Zr0.2Ti0.8)O3 Thin Films, Nano Letters, 15 (2015).
[74] R. Keech, L. Ye, J. Bosse, G. Esteves, J. Guerrier, J.L. Jones, M. Kuroda, B. Huey, S. Trolier-McKinstry, Declamped Piezoelectric Coefficients in Patterned 70/30 Lead Magnesium Niobate - Lead Titanate Thin Films, Advanced Functional Materials, submitted (2016).
[75] A.L. Roitburd, Equilibrium structure of epitaxial layer, physica status solidi, 37 (1976).
[76] V. Nagarajan, A. Roytburd, A. Stanishevsky, S. Prasertchoung, T. Zhao, L. Chen, J. Melngailis, O. Auciello, R. Ramesh, Dynamics of ferroelastic domains in ferroelectric thin films, Nature Materials, 2 (2002).
[77] C.A.B. Ball, J.H.V. Merwe, F.R.N. Nabarro, Dislocations in solids, 123 (1983).
[78] W.J. Merz, Domain Formation and Domain Wall Motions in Ferroelectric BaTiO3 Single Crystals, Phys. Rev, 95 (1954).
[79] B.S. Kwak, A. Erbil, B.J. Wilkens, J.D. Budai, M.F. Chisholm, L.A. Boatner, Strain relaxation by domain formation in epitaxial ferroelectric thin films, PHYSICAL REVIEW LETTERS, 68 (1992).
[80] R. Xu, S. Liu, I. Grinberg, J. Karthik, A.R. Damodaran, A.M. Rappe, L.W. Martin, Ferroelectric polarization reversal via successive ferroelastic transitions, Nature Materials, 14 (2014).
[81] C. Ganpule, V. Nagarajan, B. Hill, A. Roytburd, E. Williams, R. Ramesh, S. Alpay, A. Roelofs, R. Waser, L. Eng, Imaging three-dimensional polarization in epitaxial polydomain ferroelectric thin films, Journal of applied physics, 91 (2002).
[82] S. DUNN, Determination of Cross Sectional Variation ofFerroelectric Properties for Thin Film (Ca. 500 nm) PZT (30/70) via PFM, Integrated Ferroelectrics, 59 (2010).
[83] J.F. Ihlefeld, D.T. Harris, R. Keech, J.L. Jones, J.P. Maria, S. Trolier-McKinstry, Scaling Effects in Perovskite Ferroelectrics: Fundamental Limits and Process-Structure-Property Relations, Journal of American Ceramic Society, 99 (2016).
[84] A. Stanishevsky, S. Aggarwal, A.S. Prakash, J. Melngailis, R. Ramesh, Focused ion-beam patterning of nanoscale ferroelectric capacitors, Journal of Vacuum Science & Technology B, 16 (1998).
[85] A. Schilling, T. Adams, R.M. Bowman, J.M. Gregg, Strategies for gallium removal after focused ion beam patterning of ferroelectric oxide nanostructures, Nanotechnology, 18 (2007).
[86] A. Stanishevsky, B. Nagaraj, J. Melngailis, R. Ramesh, L. Khriachtchev, E. McDaniel, Radiation damage and its recovery in focused ion beam fabricated ferroelectric capacitors, JOURNAL OF APPLIED PHYSICS, 92 (2002).
[87] S.S. R. Keech, M.A. Kuroda, X. Hu Liu, G.J. Martyna, D.M. Newns, and S. Trolier-McKinstry, Lateral scaling of Pb(Mg1/3Nb2/3)TiO3-PbTiO3 thin films for piezoelectric logic applications, J. Appl. Phys., 115 (2014).
[88] H. Morioka, K. Saito, S. Yokoyama, H. Funakubo, Effect of film thickness on ferroelectric domain structure and properties of Pb(Zr 0.35 Ti 0.65)O 3 /SrRuO 3 /SrTiO 3 heterostructures, Journal of Materials Science, 44 (2009).
[89] V. Nagarajan, C.L. Jia, H. Kohlstedt, R. Waser, I.B. Misirlioglu, S.P. Alpay, R. Ramesh, Misfit dislocations in nanoscale ferroelectric heterostructures, Applied Physics letters, 86 (2005).

[90] C.S. Ganpule, A. Stanishevsky, Q. Su, S. Aggarwal, J. Melngailis, E. Williams, Scaling of ferroelectric properties in thin films, Applied Physics letters, 75 (1999).
[91] J.L. Bosse, I. Grishin, O.V. Kolosov, B.D. Huey, Multidimensional SPM applied for nanoscale conductance mapping, Journal of Materials Research, 28 (2013).
[92] V. Nagarajan, A. Roytburd, A. Stanishevsky, S. Prasertchoung, T. Zhao, L. Chen, J. Melngailis, O. Auciello, R. Ramesh, Dynamics of ferroelastic domains in ferroelectric thin films, Nature Materials, 2 (2003).
[93] R. Keech, L. Ye, J.L. Bosse, G. Esteves, J. Guerrier, J.L. Jones, M.A. Kuroda, B.D. Huey, S. Trolier-McKinstry, Declamped Piezoelectric Coefficients in Patterned 70/30 Lead Magnesium Niobate - Lead Titanate Thin Films, Advanced Functional Materials, Submitted (2016).
[94] S.V. Kalinin, D.A. Bonnell, Imaging mechanism of piezoresponse force microscopy of ferroelectric surfaces, Phys. Rev. B, 65 (2002).
[95] B.D. Huey, Fast Quantitative Nanomechanical Mapping, Annu. Rev. Mater. Res., 37 (2007).
[96] S. Bühlmann, B. Dwir, J. Baborowski, P. Muralt, Size effect in mesoscopic epitaxial ferroelectric structures: Increase of piezoelectric response with decreasing feature size, Applied Physics letters, 80 (2002).
[97] J. Seidel, L.W. Martin, Q. He, Q. Zhan, Y. Chu, A. Rother, M.E. Hawkridge, P. Maksymovych, P. Yu, M. Gajek, N. Balke, S.V. Kalinin, S. Gemming, F. Wang, G. Catalan, J.F. Scott, N.A. Spaldin, J. Orenstein, R. Ramesh, Conduction at domain walls in oxide multiferroics, Nature Materials, 8 (2009).
[98] G. Catalan, J. Seidel, R. Ramesh, J.F. Scott, Domain wall nanoelectronics, Reviews of Modern Physics, 84 (2012).